POLITECNICO DI MILANO
School of Industrial and Information Engineering
Master of Science in Mathematical Engineering
Department of Mathematics

Master Thesis in Computational Science and Engineering

Thermal creep effects described by the kinetic theory of gases

Supervisor: Prof.ssa Silvia LORENZANI

M.Sc. Thesis by:
Tommaso MISSONI
Student ID 920682

Academic Year 2019-2020

Abstract

In the last decades, considerable progress has been made in the field of miniaturization: it is now possible to miniaturize all kinds of systems (e.g., mechanical, fluidic, thermal) down to submicrometric sizes. These achievements gave rise to a new kind of technology, known as MEMS (micro-electro-mechanical systems), employed in a wide variety of applications. The challenge has now become that of integrating, into a simple micro-sized system, operations that commonly solicit a whole laboratory. Such microfluidic devices exploit the physical and chemical properties of gases at the microscale, offering several benefits over conventionally sized systems. Since usually the characteristic length of such devices, operating in gaseous environments, is comparable with (or smaller than) the mean free path of the gas molecules, the gas cannot be treated as a continuous medium and the kinetic theory of rarefied gas flows must be applied. In particular, the Boltzmann equation is the fundamental equation for the dynamics of dilute gases. In such flow conditions, other phenomena, not foreseen by the classical fluid dynamics, appear. An example is the thermal creep flow. This physical process can be used to design a Knudsen pump, a particular thermally driven micropump with no moving parts.

The aim of this thesis is to study the thermomolecular pressure difference (TPD) exponent, a physical quantity correlated to the thermal creep and the performance of a Knudsen pump. This analysis will be done in two parts.

In the first part, we consider an analytical expression of the TPD exponent for a single monatomic gas in a planar channel and we exploit this expression to assess, via experimental data, suitable values of the accommodation coefficients of the Cercignani-Lampis model for boundary conditions. From the practical point of view, five noble gases are considered.

In the second part, we address the problem of giving an appropriate definition of the TPD exponent for a binary gaseous mixture, a rather unexplored issue by now, and we consider the case of such mixture in a planar channel, trying to validate the suitability of this definition via comparison with numerical results.

Sommario

Negli ultimi decenni, enormi progressi sono stati fatti nel campo della miniaturizzazione: è ora possibile miniaturizzare ogni tipo di sistema (per esempio, meccanico, fluidodinamico, termico) a scala micrometrica. Ciò ha dato vita a un nuovo tipo di tecnologia, noto come MEMS, impiegato in una grande varietà di applicazioni. L'obiettivo è ora quello di integrare, in un semplice microdispositivo, operazioni che comunemente richiederebbero un intero laboratorio. Tali sistemi sfruttano le proprietà fisiche e chimiche di liquidi e gas alla microscala, offrendo numerosi vantaggi rispetto ai sistemi di dimensioni convenzionali. Poiché solitamente la lunghezza caratteristica di tali dispositivi, operanti in ambienti gassosi, è paragonabile al (o più piccola del) cammino libero medio delle molecole di gas, il gas non può essere trattato come un mezzo continuo e si deve applicare la teoria cinetica dei gas rarefatti. In particolare, l'equazione di Boltzmann è l'equazione fondamentale della dinamica di tali gas. In tali condizioni compaiono altri fenomeni, non previsti dalla classica fluidodinamica. Un esempio è il thermal creep. Questo fenomeno fisico può essere utilizzato per progettare una pompa di Knudsen, un particolare tipo di micropompa termicamente guidata e senza parti mobili.
Lo scopo di questa tesi è quello di studiare il TPD exponent, una quantità fisica correlata al fenomeno del thermal creep e alla performance di una pompa di Knudsen. Questa analisi verrà condotta in due parti.
Nella prima parte, consideriamo un'espressione analitica del TPD exponent per un gas monoatomico tra due piastre parallele, utilizzando tale espressione per determinare, attraverso dati sperimentali, valori appropriati dei coefficienti di accomodamento del modello di condizioni al bordo di Cercignani-Lampis. A questo scopo, consideriamo cinque gas nobili.
Nella seconda parte, affrontiamo il problema di dare una corretta definizione del TPD exponent per una miscela binaria di gas, un problema ancora piuttosto inesplorato, e consideriamo il caso di tale miscela tra due piastre parallele, per provare ad avvalorare la correttezza di tale definizione tramite un confronto con dati numerici.

Contents

List of Figures

List of Tables

List of Abbreviations

TPD	Thermomolecular Pressure Difference
KP	Knudsen Pump
MEMS	Micro-Electro-Mechanical System
NEMS	Nano-Electro-Mechanical System
BE	Boltzmann Equation
LBE	Linearized Boltzmann Equation
HS	Hard Sphere
LJ	Lennard-Jones
BGK	Bhatnagar-Gross-Krook
CL	Cercignani-Lampis
AC	Accommodation Coefficient
TSC	Thermal Slip Coefficient

1. Introduction

1.1. Kinetic theory, MEMS and Microfluidics

In the last decades, considerable progress has been made in the field of miniaturization: it is now effectively possible to miniaturize all kinds of systems (e.g., mechanical, fluidic, electromechanical, thermal) down to submicrometric sizes.
In the 1980s, these achievements gave rise to a new kind of technology, known as **MEMS** (**micro-electro-mechanical systems**). This nomenclature generally refers to devices that have a characteristic length of less than 1 mm but more than 1 µm, that combine electrical and mechanical components and that are fabricated using integrated circuit batch-processing technologies. Later, in the 1990s, this domain became considerably diversified, with MEMS devices being fabricated for chemical, biological, and biomedical applications. Electrostatic, magnetic, electromagnetic, pneumatic and thermal actuators, motors, valves, gears, cantilevers, diaphragms and tweezers less than 100 µm in size have been fabricated. These have been used as sensors for pressure, temperature, mass flow, velocity, sound and chemical composition; as actuators for linear and angular motions; and as simple components for complex systems such as robots, micro-heat-engines and micro-heat-pumps, mass spectrometers, gas chromatographs, optical spectrometers, electron beam optics, and on-demand gas generators.
In this wide variety of applications, encountered in our everyday life, gas flows are very important. For example, gas sensors, chemical reactors, and electron optical systems usually require a vacuum pump to draw in a gas sample or to evacuate an air space. The development of such devices has opened up an entirely new field of research where the behaviour of flows far from equilibrium conditions is very important. In some cases, the equations of mass, momentum and energy equilibrium, combined by the Newton-Fourier-Fick constitutive equations, describe their behaviour very well and have been actually applied successfully for many years. However, this formulation is subject to certain limitations due to the underlying assumption that the gas must be considered as a continuum medium. Even though this is a reasonable assumption for many cases, there are situations where this hypothesis fails. This happens, for example, when the mean free path between intermolecular collisions may become comparable to a characteristic length, due to conditions of low pressure or if the gas is confined in a region of very small dimensions: in such cases the continuum medium assumption collapses. Beyond a certain limit, it is not possible to investigate such phenomena accurately without taking into account the molecular nature of the gas. In this case, we may say that the gas is in a *rarefied state*, for which the departure from the thermodynamic equilibrium leads to a failure of the macroscopic equations. To deal with these cases, several approaches are used depending on the application under study. Concepts derived from statistical mechanics and kinetic theory of gases need to be involved.

Statistical mechanics may be naturally divided into two branches, one dealing

with *equilibrium systems*, the other with *non-equilibrium systems*. Nonequilibrium phenomena are much less understood at the present time, but a notable exception is offered by the case of dilute gases, studied in the framework of the **kinetic theory of gases**. Here a basic equation was established by Ludwig Boltzmann in 1872.
The so-called **Boltzmann equation** appears as a prototype of a reduced description taking into account only partial information about the underlying microscopic state (fully described by the coordinates and momenta of all the molecules), but nevertheless undergoing an autonomous time evolution. This equation, used to describe transport phenomena in the framework of kinetic theory, concerns the distribution function of particles, a 7-dimensional probability density distribution of molecules in the physical space, molecular velocity space and time. The Botzmann equation is quite complex and can be solved analytically only for very specific situations, a fact that often leads to the pursuit of numerical solutions, since the experimental investigation is, usually, very costly. However, the solution of this equation is widely used today and leads to a good approach for a large number of problems with satisfactory results.

As an important example of exploitation of this method, it allowed scholars to study fluid flows operating under unusual and unexplored conditions, peculiar feature of MEMS devices, which naturally led to the need for the creation of a new discipline: **microfluidics**, which can be defined as "the study of flows that are simple or complex, mono- or multiphasic, which are circulating in artificial microsystems"[1]. This engineering development allowed the implementation of a whole new kind of experiments.

1.1.1. About Microfluidics

In the early 1990s, microchannel flow experiments revealed intriguing results for both liquids and gases that sparked excitement and new interest in the study of low Reynolds number flows at microscales. Another influential development at about the same time was the fabrication of the first microchannel with integrated pressure sensors. Indeed, while the experimental results indicated global deviations of microflows from canonical flows, pointwise measurements for gas flows with pressure sensors, and later with temperature sensors, revealed a new flow behavior at microscales not captured by the familiar continuum theory.
In microgeometries the flow is granular for liquids and rarefied for gases, and the walls "move". In addition, other phenomena such as thermal creep, electrokinetics, viscous heating, anomalous diffusion, and even quantum and chemical effects may become significant. Most important, the material of the wall and the quality of its surface play a very important role in the momentum and energy exchange between the flowing fluid and its solid container.
One could argue that at least for gases the situation is similar to low-pressure high-altitude aeronautical flows, which were studied extensively more than 50 years ago. Indeed, there is a similarity in a certain regime of rarefaction. However, most gas microflows correspond to a low Reynolds number and low Mach number, in contrast to their aeronautical counterparts. Moreover, the typical microgeometries are of very large aspect ratio, and this poses more challenges for numerical modeling, but also creates

[1] P. Tabeling. *Introduction to Microfluidics*. Oxford University Press, 2005.

opportunities for obtaining semianalytical results [2].
The main differences between fluid mechanics at microscales and in the macrodomain can be broadly classified into four areas:

- non-continuum effects;
- surface-dominated effects;
- low Reynolds number effects;
- multiscale and multiphysics effects.

For gas microflows, compressibility effects are very important because of relatively large density gradients, although the Mach number is typically low. Depending on the degree of rarefaction, corrections at the boundary or everywhere in the domain need to be incorporated. Increased rarefaction effects may make the constitutive models for the stress tensor and the heat flux vectors in the Navier-Stokes equations invalid. This is the main reason why the Boltzmann equation and the whole construction of the kinetic theory play a fundamental role: they are the main tool for the study of these problems, because they are valid where the continuum model fails.

1.1.2. More about MEMS

Miniaturization and MEMS gave birth to microfluidics in the 1990s and today still constitute a large portion of this relatively new discipline. MEMS are electro-mechanical systems whose total size varies between 1 and 300 µm. Although these numbers are rough limits (there are actually MEMS of submicrometer size and MEMS larger than 300 µm), the majority of MEMS devices fabricated today have typical dimensions of this order, and actually "acting" at a micrometric scale, rather than just "observing" (for which it is sufficient an optical microscope, invented centuries ago), is precisely what MEMS technology allows us to do.
However, the industrial success of MEMS is not solely due to the improvement in sensor response and sensitivity, but also due to the ability to integrate detection, information analysis, and signal processing all on one single chip. Just as with integrated circuits, this chip can, in principle, be easily reproduced by the millions. As an example: the cost, which is so critical in the field of automobile manufacturing, becomes very advantageous as compared to traditional systems, and for this reason all modern automobiles now use MEMS for their airbags. Today, the volume of MEMS activity is estimated to be worth between several billion and several tens of billions of dollars. In the United States, there was on average 2-5 MEMS per person in the 2000s. Today, there are numerous industries involved in MEMS: both new industries, appeared in just the last few years, as well as more traditional ones that use MEMS in a significant way in their sector of activity, or that profit from developing novel ventures by taking advantage of the potential of this young technology (see [1] for more details).

[2] This happens because a large disproportion between the dimensions of a computational domain may cause problems in the numerical computation, but also simplify some analytical procedures (think about a rectangular channel with width much larger than height: hence, the channel can be approximated with a planar channel, with a much simpler analytical treatment).

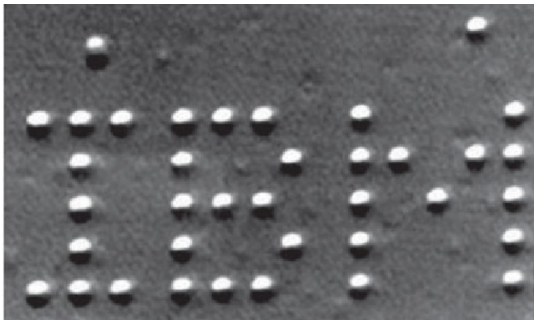

(a) The word 'IBM' spelled with 35 Xenon atoms arranged individually with a STM (from [3]).

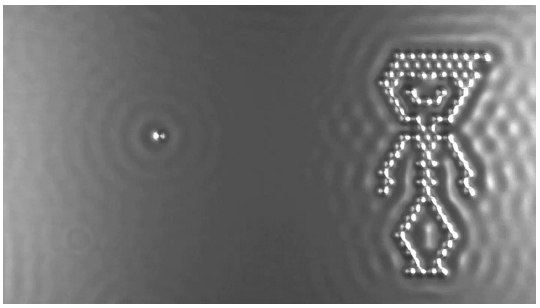

(b) A frame of *A Boy And His Atom: The World's Smallest Movie*.

Figure 1.1.: "Observing" and "acting" at the microscale... yes, they are atoms! (Courtesy of IBM.)

The history of the field of MEMS is an interesting one. The year 1959 is often considered to be the beginning of the history of micro- and nano-technologies. In December of that year a visionary speech was given by Richard P. Feynman during the APS (American Physical Society) meeting at Caltech. This speech was entitled *There is plenty of room at the bottom*, whose beginning went as follows:

> I would like to describe a field, in which little has been done, but in which an enormous amount can be done in principle. This field is not quite the same as the others in that it will not tell us much of fundamental physics (in the sense of, "What are the strange particles?") but it is more like solid-state physics in the sense that it might tell us much of great interest about the strange phenomena that occur in complex situations. Furthermore, a point that is most important is that it would have an enormous number of technical applications. [2]

These suggestions did not remain just a part of a fantasy world. In 1989, at IBM's Almaden lab, Don Eigler and Erhard Schweizer sprayed a nickel substrate with vaporized Xenon, and by bringing the probe tip of their scanning tunnelling microscope (STM) close to the sample, they precisely placed 35 of these atoms to spell the word 'IBM', which was just a few nanometers long at the end ([3]). Later, in 2013, in the same lab and with the same technique, IBM Research released *A Boy And His Atom: The World's Smallest Movie*, a stop-motion animated short film composed by 242 frames of few hundreds of carbon monoxide molecules each, manipulated into place on a copper substrate with a copper needle, each frame measuring 45 by 25 nanometres (the video is freely available at [4] and [5]).
The first MEMS devices were created a decade after Feynman's speech, and the invention of new microsystems has been the center of activities of laboratories involved in MEMS in the 1990s. Today, a sort of maturation in the domain of MEMS prevails, resulting in less time being spent on creating new systems and more time being spent on investigating concrete applications.

It is now clear that the relation which occurs between MEMS and microfluidics is almost symbiotic: MEMS are the only way to study micro-flows from an experimental point of view, and in turn theoretical microfluidics, thanks to these experimental data, can be developed to improve the design and performance of MEMS themselves.

1.1.3. Micropumps

Micromachined pumps have many potential uses: they may be used to create a high pressure (compressors), create a low pressure (vacuum pumps), or transport gases with no substantial change in pressure. Potential applications for these devices include driving gases for gas chromatography, spectroscopy, and μ-plasmas; pneumatic pumping of liquids for spectroscopy; or to maintain vacuum on-chip without requiring hermetic packaging for vacuum encapsulated applications.

From biology and medicine to space exploration and microelectronics cooling, fluid volumes on the order of a milliliter and below figure prominently in an increasing number of engineering systems. The small fluid volumes in these systems are often pumped, controlled or otherwise manipulated during operation. For example, biological samples must be moved through the components of miniature assay systems, and coolant must be forced through micro heat exchangers. Microfluidic transport requirements such as these can sometimes be met by taking advantage of passive mechanisms, most notably surface tension. For other applications, macroscale pumps, pressure/vacuum chambers and valves provide adequate microfluidic transport capabilities. Yet for many microfluidic systems, a self-contained, active pump, the package size of which is comparable to the volume of fluid to be pumped, is necessary or highly desirable. Nonetheless, the pumps available during the late 1990s were greatly oversized for the tiny flows needed for the above mentioned MEMS devices. Moreover, in terms of size, weight, cost, and power consumption, pumps remain the single largest component. Let us consider briefly a few applications to gain insight into design parameters relevant to micropumps.

Dispensing *therapeutic agents* into the body has long been a goal of micropump designers. Among the first micropumps, those developed by Jan Smits in the early 1980s were intended for use in controlled insulin delivery systems for maintaining diabetics' blood sugar levels without frequent needle injections. Micropumps might also be used to dispense engineered macromolecules into tumors or the bloodstream. High volumetric flow rates are not likely to be required of implanted micropumps (the amount of insulin required by a diabetic per day, for example, is less than a milliliter) but precise metering is of great importance. The pressure generation requirements for implantable micropumps are not insignificant, as the back pressure encountered *in vivo* can be as high as 25 kPa. Reliability, power consumption, cost and biocompatibility are critical. To date, deficiencies in these areas have precluded widespread implantantion of micropumps. For example, currently available implanted insulin delivery systems employ static pressure reservoirs metered by solenoid-driven valves and are over 50 cm^3 in size.

A number of researchers have sought to develop micropumps for use in single- or two-phase *cooling of microelectronic devices*. Microelectronics cooling is highly demanding with respect to flow rate. For instance, Tuckerman and Pease's seminal paper on liquid-phase chip cooling contemplated flow rates of several hundred milliliters per minute. Recent studies indicate that two-phase convective cooling of a 100 W microchip will require flowrates of order 10 $ml\,min^{-1}$ or more. The fundamental scaling associated with pressure-driven flow dictates that high pressures (100 kPa or greater) will be required to force such high flow rates through microchannels and/or jet structures found in micro heat sinks. In the laminar regime, an order-of-magnitude decrease in the hydraulic diameter of a channel (the channel cross-sectional area multiplied by four and divided

by its perimeter) increases by two orders of magnitude the pressure difference required to maintain a constant average flow velocity. Cost and power consumption are also important considerations, the latter especially for mobile units. Micropumps might also be built directly into integrated circuits to cool transient hot spots, and so fabrication methods and temporal response characteristics may be particularly important. Insensitivity to gas bubbles is also important as bubbles are present in and detrimental to many microfluidic systems.

Much attention has been focused recently on miniature systems for *chemical and biological analysis*. Miniaturization of chemical assays systems can reduce the quantities of sample and reagents required, often allows assays to be performed more quickly and with less manual intervention and also enables portability. Miniaturization sometimes offers the further advantage of enabling use of inexpensive disposable substrates. Although fluids (typically liquids) must typically be introduced into, and transported within, these micro total analysis systems (μTAS) during operation, micropumps are found in very few current-generation systems. Liquid transport is instead often accomplished through manual pipetting, with external pneumatic sources, or by inducing electro-osmotic flow. The limited use of micropumps in μTAS may be partly due to the lack of available micropumps with the necessary combination of cost and performance. Compatibility with the range of fluid volumes of interest will be necessary if micropumps are to become more widely used in μTAS. Monitoring single cells may require manipulation of fluid volumes on the order of 1 pl. Microchip-based systems used in drug discovery amplify DNA, separate species through capillary electrophoresis, and/or interface with mass spectrometers with sample volumes ranging from hundreds of picoliters to hundreds of microliters. Patient pain considerations have prompted manufacturers of *in vitro* blood glucose monitors for diabetics to minimize sample size requirements; current systems need a sample volume of only one-third of a microliter. Detecting microbes in human body liquids often requires somewhat larger sample volumes; for example, a common immunoassay-based blood test for malaria uses a sample volume of 10 µl. Other parameters important for μTAS include working fluid properties such as pH, viscosity, visco-elasticity and temperature, as well as the presence of particles (e.g., cells or dust) which may disrupt operation of pumps and valves. Secondary effects associated with reliability and corrosion include the impact of mechanically shearing the sample, chemical reactions, adsorption of analytes and wear of moving parts.

Space exploration is another exciting area for micropump technologies. Miniature roughing pumps are needed for use in mass spectrometer systems to be transported on lightweight spacecrafts. Such a pump would likely be required to achieve a vacuum of approximately 0.1 Pa, the level at which high vacuum pumps typically become effective. Miniature roughing pumps have been sought for other applications as well. Micropropulsion is another potential application of micropumps in space. For example, ion-based propulsion systems proposed for future 1-5 kg "microspacecraft" may require delivery of compressed gases at $1\,\mathrm{ml\,min^{-1}}$ flow rates.

Inspired by this wide range of applications, several archival journal papers reporting new micropumps or analyzing micropumps operation have been published since Smits' micropump was first developed in the 1980s.
From now on, let us focus on gas pumps, and specifically **vacuum pumps** (or **compressors**).

Vacuum pumps may be divided into two broad classes: entrapment pumps and gas transfer pumps. Examples of entrapment pumps include adsorption, getter, and cryopumps. Gas transfer pumps may be divided into two further classifications: those using positive displacement to achieve compression, and those using kinetic forces to compress. Common displacement pumps are piston, diaphragm, rotary vane, roots, and gear pumps, all of which have moving parts. Kinetic pumps include those with moving parts such as turbine and drag pumps, and those without moving parts such as diffusion, jet/ejector, and ion pumps, a characteristic the latter group shares with the entrapment pumps. To the category of kinetic pumps with no moving parts belong the **thermal molecular** (or **thermally driven**) **pumps**, such as thermal transpiration and accommodation pumps, which are particularly suited to miniaturization and fabrication by integrated circuit lithographic techniques.
Displacement pumps have potential mechanical reliability concerns (e.g., stiction, wear-and-tear of the moving parts, etc.) as well as problems related to particulate generation, friction power losses, leakage at sliding or rotating shaft feedthrough seals, acoustic noise, and pulsating flows. Conversely, thermally driven micropumps with no moving parts, such as the **Knudsen pump**, have high reliability and uses a low operating voltage. Moreover, the absence of moving parts allows a simple fabrication process.

In thermal molecular pumps, pumping energy is supplied by temperature changes alone. As we shall see in detail, a general feature of such pumps is that the upper pressure limit is reached when the mean free path becomes small relative to the physical dimensions of the pump in the region of the temperature transition. Thus, the upper pressure limits of these pumps have been determined by the microfabrication limits of the day; they have operated at relatively low pressures, with low throughputs, and have not become main line pumps. In recent years, however, MEMS has introduced a whole new level of miniaturization to devices in general, including vacuum devices, and hence has raised the upper pressure limits, and thus the throughputs of thermal molecular pumps to atmospheric levels. The general pumping phenomenon has had various names: Knudsen compressor; thermal transpiration; thermal creep; thermodynamic, thermolecular, thermal molecular, and accommodation pumping. In this work, we shall consider this kind of pumps.

To deepen the study of the basic and guide concepts of statistical mechanics of non-equilibrium, the great book by Cercignani, [6], is highly recommended.
The informations and details reported here about the birth of MEMS and microfluidics have been taken from [1, 7].
For the section on micropumps, we relied on [8, 9, 10, 11].
It has also been useful the reading of the basic but rather complete and effective introduction of [12].

1.2. The problem under study

Now that the interest in microfluidics, MEMS and micropumps has been fully justified, we shall present the main topic of this thesis.

We will deal with the study of the **thermomolecular pressure difference** (or **TPD**) **exponent**, also denoted by γ: it is a physical quantity correlated, from a prac-

tical point of view, to the analysis of the performance of a Knudsen pump. We shall give a description of the functioning of the Knudsen pump as well as the definition of the TPD exponent later on.

We will study the TPD exponent in two different situations:

- first, we will consider a single gas between two infinite parallel plates and in the slip and transition regime;
- then, a binary gaseous mixture will be studied, likewise entrapped in a planar channel but for arbitrary rarefaction regime.

The Boltzmann equation will be exploited. Further mathematical and physical details, such as the kinetic models, the boundary conditions and the intermolecular interaction employed, will be specified in the dedicated chapters.

1.3. Structure and aim of the thesis

The thesis is structured as follows.

In Chapter 2 we provide the theoretical framework in which we will deal with our problem, in order to give a common notation and an overview of the most important concepts and techniques in the field of kinetic theory of gases. Also, the functioning mechanism of the Knudsen pump is presented, along with its connection with the TPD exponent γ.

In Chapter 3 we study in detail the TPD exponent in the case of a single gas. In particular, we present an analytical expression, valid in a particular rarefaction regime, whose numerical behaviour is widely explored, we verify its reliability comparing it with other accurate numerical results, and finally we use it to reproduce some experimental data.

In Chapter 4 we deal with the thermal creep problem for a binary gas mixture with a particular kinetic model, the McCormack model, and we exploit some dataset, already present in literature, concerning numerical results about mass fluxes in order to compute the TPD exponent and study its numerical behaviour.

In Chapter 5 we summarize our work and discuss possible future developments and improvements.

The aim of this work is twofold. From one side, it is guided by the theoretical interest in a better explanation and a deeper understanding of a phenomenon which is still not much studied and investigated, both theoretically and experimentally. From the other side, from a practical point of view, it can be seen as a small step toward an improved modelling of the gas-surface interaction, mandatory in the treatment of rarefied flows, and a refined description of the different rarefaction regimes, in particular about the extendibility of the use of the Navier-Stokes equations into the transition regime.

1.3.1. Original contributions

The original contributions in this work consist in the systematic and detailed numerical analysis of the TPD exponent for the case of a single gas. In this case, experimental data will be considered and exploited for the assessment of the accommodation coefficients,

which describe the gas-surface interaction. For what concerns the case of gas mixture, a suitable definition of the TPD exponent is conjectured, the thermal creep problem is formulated and numerical data from literature are used for the analysis of the behaviour of such TPD exponent in different situations.

2. Background

In this chapter we outline the framework in which we will work in the following chapters, with the aim of introducing a theoretical background, a common notation, and a general view of some of the most important techniques in each area.

2.1. Elements of Kinetic Theory of Gases and the Boltzmann equation

The Boltzmann equation can be derived rigorously from Newton's laws at least for the low-density limit, but it is also used for the dense limit, although there is no totally rigorous theoretical basis for the latter (see [7, 13]). Research efforts focused on obtaining most of the fluid-dynamics limits of the Boltzmann equation including the incompressible limit (see [14, 15, 16, 17]).
In this work, we assume that microscale fluidic and thermal gas transport in the entire rarefaction regime is governed by the Boltzmann equation (BE), which describes the evolution of the velocity distribution function of gas molecules through binary intermolecular collisions.

2.1.1. The Boltzmann equation

Let us consider monoatomic gases, the state of which can be described by a velocity distribution function $f(t, \mathbf{x}, \boldsymbol{\xi})$, where $\mathbf{x}$ denotes the position and $\boldsymbol{\xi}$ denotes the velocity of the molecules. The set of all possible positions $\mathbf{x}$ and velocities $\boldsymbol{\xi}$ is the so-called **phase space**. The distribution function represents the total mass of the molecules contained in $d\mathbf{x}d\boldsymbol{\xi}$, the element of volume of the phase space, at time t. This distribution function obeys the **Boltzmann equation** ([6, 18, 19, 20])

$$\frac{\partial f}{\partial t} + \boldsymbol{\xi} \cdot \frac{\partial f}{\partial \mathbf{x}} + \mathbf{F} \cdot \frac{\partial f}{\partial \boldsymbol{\xi}} = Q(f, f_*) \tag{2.1}$$

with $\mathbf{x} \in \Omega$, $\boldsymbol{\xi} \in \mathbb{R}^3$ and Ω is the space domain where the gas is moving.
$\mathbf{F}$ is an external body force. Since we shall usually consider cases where the external action on the gas is exerted only through solid boundaries (surface forces), we shall not usually consider the term describing body forces (so, if not differently specified, we shall always consider $\mathbf{F} = \mathbf{0}$); it should be kept in mind, however, that such simplification implies neglecting, *inter alia*, gravity.
The term on the right-hand side represents molecule collisions: it is called **collision integral** and it is given by

$$Q(f, f_*) = \frac{1}{m} \int_{\mathbb{R}^3} \int_{S^+} \mathcal{B}(\mathbf{V} \cdot \mathbf{n}, |\mathbf{V}|) \left[f(\mathbf{x}, \boldsymbol{\xi}_*') f(\mathbf{x}, \boldsymbol{\xi}') - f(\mathbf{x}, \boldsymbol{\xi}_*) f(\mathbf{x}, \boldsymbol{\xi}) \right] d\mathbf{n} d\boldsymbol{\xi}_* \tag{2.2}$$

where the quantity $\mathcal{B}(\mathbf{V} \cdot \mathbf{n}, |\mathbf{V}|)$ depends on the intermolecular interaction potential. In the case of a hard-sphere gas, it is $\mathcal{B}(\mathbf{V} \cdot \mathbf{n}, |\mathbf{V}|) = |\mathbf{V} \cdot \mathbf{n}|$.

The quantity defined by Eq. (2.2) represents collisions of two molecules with post-collision velocities $\boldsymbol{\xi}$ and $\boldsymbol{\xi}_*$, and corresponding pre-collision velocities denoted in addition by primes. Here, the integration is taken over the three-dimensional velocity space $\mathbb{R}^3$ and the hemisphere S^+, which includes the particles moving away from each other after the collision. Also, we have the definitions

$$\mathbf{V} = \boldsymbol{\xi} - \boldsymbol{\xi}_* \qquad \boldsymbol{\xi}' = \boldsymbol{\xi} - \mathbf{n}(\mathbf{n}\cdot\mathbf{V}) \qquad \boldsymbol{\xi}'_* = \boldsymbol{\xi}_* + \mathbf{n}(\mathbf{n}\cdot\mathbf{V})\,, \tag{2.3}$$

where $\mathbf{n}$ is the unit vector along $\boldsymbol{\xi} - \boldsymbol{\xi}'$.

2.1.2. Macroscopic quantities

All the **macroscopic quantities**, which are the quantities of main practical interest, are defined in terms of moments of the distribution function:

$$\text{density:} \quad \rho(\mathbf{x},t) = \int f d\boldsymbol{\xi} \tag{2.4}$$

$$\text{bulk velocity:} \quad \rho\mathbf{v}(\mathbf{x},t) = \int \boldsymbol{\xi} f d\boldsymbol{\xi} \tag{2.5}$$

$$\text{temperature:} \quad T(\mathbf{x},t) = \frac{1}{3\rho R}\int c^2 f d\boldsymbol{\xi} \tag{2.6}$$

$$\text{stress:} \quad P_{ij}(\mathbf{x},t) = \int c_i c_j f d\boldsymbol{\xi} \tag{2.7}$$

$$\text{heat flux:} \quad \mathbf{q}(\mathbf{x},t) = \frac{1}{2}\int \mathbf{c} c^2 f d\boldsymbol{\xi} \tag{2.8}$$

where $\mathbf{c} := \boldsymbol{\xi} - \mathbf{v}$ is called *peculiar velocity.*
We define also the

$$\text{number density:} \quad n(\mathbf{x},t) = \frac{\rho(\mathbf{x},t)}{m} \tag{2.9}$$

where m is the molecular mass.

2.1.3. Equilibrium states

The solution of the Boltzmann equation (2.1) for an **equilibrium state** (i.e., $\partial f/\partial t = 0$, $\partial f/\partial x_i = 0$) is given by the following (*absolute*) *Maxwell distribution* or *Maxwellian* with five constant parameters n_0, $\mathbf{v}$ and T_0:

$$f_0 = \frac{n_0\beta_0^3}{\pi^{3/2}}\exp\left(-\beta_0^2|\boldsymbol{\xi}-\mathbf{v}|^2\right) = n_0\left(\frac{m}{2\pi k_B T_0}\right)^{3/2}\exp\left(-\frac{m}{2k_B T_0}|\boldsymbol{\xi}-\mathbf{v}|^2\right) \tag{2.10}$$

with

$$\beta_0^2 = \frac{m}{2k_B T_0}\,, \tag{2.11}$$

and k_B being the Boltzmann constant, n_0 being the equilibrium number density, T_0 being some reference temperature.
The equilibrium distribution with variable parameters n, $\mathbf{v}$ and T is called *local Maxwellian.*

2.1.3.1. Linearization

Since in microchannel flow applications one usually deals with small deviations from the basic equilibrium state, Eqs. (2.1) and (2.2) can be linearized representing the distribution function as

$$f = f_0(1+h) \quad |h| \ll 1 \tag{2.12}$$

with f_0 being the Maxwellian configuration 2.10.
The small perturbation h satisfies the following linearized Boltzmann equation

$$\frac{\partial h}{\partial t} + \boldsymbol{\xi} \cdot \nabla_{\mathbf{x}} h = Lh\,, \tag{2.13}$$

where Lh is the linearized collision operator given by

$$\begin{aligned} Lh = n_0 \left(\frac{m}{2\pi k_B T_0}\right)^{3/2} \int_{\mathbb{R}^3}\int_{B^+} \left[h(\boldsymbol{\xi}') + h(\boldsymbol{\xi}_*') - h(\boldsymbol{\xi}) - h(\boldsymbol{\xi}_*)\right] \times \\ \times \exp\left(-\frac{m}{2k_B T_0}{\xi_*}^2\right) \mathcal{B}(\mathbf{V}\cdot\mathbf{n}, |\mathbf{V}|) d\mathbf{n} d\boldsymbol{\xi}_* \\ = \int_{\mathbb{R}^3}\int_{B^+} \left[h(\boldsymbol{\xi}') + h(\boldsymbol{\xi}_*') - h(\boldsymbol{\xi}) - h(\boldsymbol{\xi}_*)\right] f_{0*} \mathcal{B}(\mathbf{V}\cdot\mathbf{n}, |\mathbf{V}|) d\mathbf{n} d\boldsymbol{\xi}_*\,. \end{aligned} \tag{2.14}$$

2.1.4. Boundary conditions

Accurate modelling of gas-surface interaction is very important for external rarefied gas flows, such as those around shuttles and satellites, as well as for internal rarefied or small-scale flows, such as those in MEMS or in gas shale reservoirs, both characterized by large surface area-to-volume ratios ([7]).
The **boundary conditions** for the BE must be formulated on a probabilistic ground by specifying the relation between the velocity distribution function of the reflected and the incident gas molecules on the solid surface. The wall characteristics can be taken into account via the non-negative *scattering kernel*

$$R(\boldsymbol{\xi}' \to \boldsymbol{\xi}; \mathbf{x}, t) \tag{2.15}$$

representing a probability density that molecules hitting the wall with velocity between $\boldsymbol{\xi}'$ and $\boldsymbol{\xi}' + d\boldsymbol{\xi}'$ at location $\mathbf{x}$ at time instant t will be reflected with velocity between $\boldsymbol{\xi}$ and $\boldsymbol{\xi}+d\boldsymbol{\xi}$. If R is known, then we can obtain the boundary condition for the distribution function as ([21, 6, 13, 22])

$$f(\mathbf{x}, \boldsymbol{\xi}, t)|\xi_n| = \int_{\xi_n'<0} |\xi_n'| R(\boldsymbol{\xi}' \to \boldsymbol{\xi}; \mathbf{x}, t) f(\mathbf{x}, \boldsymbol{\xi}', t) d\boldsymbol{\xi}' \quad (\mathbf{x} \in \partial\Omega\,,\, \xi_n > 0) \tag{2.16}$$

where $\xi_n = \boldsymbol{\xi}\cdot\mathbf{n}$ is the velocity normal to the surface. If the wall restitutes all the gas molecules (i.e., it is nonporous and nonadsorbing), then

$$\int_{\xi_n'>0} R(\boldsymbol{\xi}' \to \boldsymbol{\xi}; \mathbf{x}, t) = 1\,. \tag{2.17}$$

Moreover, the scattering kernel satisfies the *reciprocity condition* ([6, 19])

$$|\boldsymbol{\xi}'\cdot\mathbf{n}| f_0(\boldsymbol{\xi}') R(\boldsymbol{\xi}' \to \boldsymbol{\xi}) = |\boldsymbol{\xi}\cdot\mathbf{n}| f_0(\boldsymbol{\xi}) R(-\boldsymbol{\xi} \to -\boldsymbol{\xi}') \quad (\boldsymbol{\xi}\cdot\mathbf{n} > 0,\, \boldsymbol{\xi}'\cdot\mathbf{n} < 0) \tag{2.18}$$

also known as *preservation of equilibrium.*

2.1.4.1. Maxwell boundary conditions

In [23], Maxwell proposed to treat the surface as something intermediate between a perfectly reflecting and a perfectly absorbing surface. In particular, he supposed that a portion of every surface element absorbs all the incident molecules, and afterwards allows them to re-evaporate with the velocities corresponding to those in a still gas at the temperature of the solid wall, while the remaining portion perfectly reflects all the molecules incident upon it ([21]).
If we call α the fraction of evaporated molecules (and so $0 \leq \alpha \leq 1$), Maxwell's assumption is translated mathematically in the **Maxwell model** or **diffuse-specular model** (see, e.g., [24, 25])

$$R_M(\boldsymbol{\xi}' \to \boldsymbol{\xi}) = \alpha|\xi_n| f_0(\boldsymbol{\xi}) + (1-\alpha)\delta(\boldsymbol{\xi}' - \boldsymbol{\xi} + 2\mathbf{n}\xi_n) \quad (\xi_n > 0,\, \xi_n' < 0) \tag{2.19}$$

where T_0 is the temperature of the wall and f_0

$$f_0 = n_0 \left(\frac{m}{2\pi R T_0}\right)^{3/2} \exp\left(-\frac{\xi^2}{2RT_0}\right) \tag{2.20}$$

is called *wall Maxwellian*.
For $\alpha = 1$ we obtain a *purely diffuse scattering*, which physically means that we have *perfect accommodation*, in the sense that the molecules "forget their past" and re-emerge after the wall collision with a Maxwellian distribution function. On the other hand, for $\alpha = 0$ we have that the wall *specularly reflects* the molecule.
Maxwell's boundary conditions are frequently used for their simplicity and reasonable accurateness, but are by no means the only possible ones, and not very satisfactory in general.

2.1.4.2. Cercignani-Lampis boundary conditions

The **Cercignani-Lampis model**, introduced for the first time in [26], makes use of two **accommodation coefficients**: the tangential accommodation coefficient α_t ($0 \leq \alpha_t \leq 2$), and the normal accommodation coefficient α_n ($0 \leq \alpha_n \leq 1$). It has the form (see, e.g., [24, 25, 27, 28])

$$R_{CL}(\boldsymbol{\xi}' \to \boldsymbol{\xi}) = \frac{2\xi_n}{\pi \alpha_t \alpha_n (2-\alpha_t)} I_0\left(\frac{2\sqrt{1-\alpha_n}}{\alpha_n}\xi_n \xi_n'\right) \times \\ \times \exp\left(-\frac{[\boldsymbol{\xi}_t - (1-\alpha_t)\boldsymbol{\xi}_t']^2}{\alpha_t(2-\alpha_t)}\right) \exp\left(-\frac{\left[{\xi_n}^2 + (1-\alpha_n){\xi_n'}^2\right]}{\alpha_n}\right) \tag{2.21}$$

where I_0 is the modified Bessel function of first kind and zeroth order.
The CL model recovers, as limiting cases, the *specular reflection* ($\alpha_t = 0$, $\alpha_n = 0$) and the *diffuse re-emission* ($\alpha_t = 1$, $\alpha_n = 1$). Moreover, it includes the *back scattering* ($\boldsymbol{\xi} = -\boldsymbol{\xi}'$) when $\alpha_t = 2$, $\alpha_n = 0$.

2.1.5. Model equations

One of the main difficulties in dealing with the Boltzmann equation is the complicated structure of the collision integral, Eq. (2.2). Therefore, alternative, simpler expressions

have been proposed for the collision term: they are known as **collision** (or **kinetic**) **models**, and any Boltzmann-like equation where the Boltzmann collision integral is replaced by a collision model is called a **model equation**.
The idea behind this replacement is that a large amount of detail of the two-body interaction (which is contained in the collision term) is not likely to influence significantly the values of many experimentally measured quantities: therefore, when one is not interested in too much fine details, it is possible to obtain reasonable results by replacing the collision integral by the collision model $J(f)$, that retains only the qualitative and average properties of the collision term $Q(f, f)$.

2.1.5.1. BGK model for monatomic gases

The most widely known collision model is the **Bhatnagar-Gross-Krook model** (**BGK**), proposed for the first time in 1954 in [29, 30]. It reads as follows:

$$J(f) = \nu[\Phi(\boldsymbol{\xi}) - f(\boldsymbol{\xi})] \tag{2.22}$$

where the *collision frequency* ν is independent of $\boldsymbol{\xi}$ (but depends on ρ and T), and Φ is the local Maxwellian which has at any space point and time instant the same density, velocity and temperature of the gas given by the distribution function f.
The idea behind this model is to express in the simplest way the tendency of the gas to a Maxwellian distribution (i.e., to an equilibrium state): we assume that the average effect of collisions is to change the distribution function f by an amount proportional to the departure from a Maxwellian Φ ([6]).
The main disadvantage of the BGK model is that it yields a wrong Prandtl number ($Pr^{BGK} = 1$ instead of the correct value 2/3). As a consequence, it can be proved that (see e.g. [31]) no choice of the parameter ν is compatible with both viscosity and thermal conductivity, and hence the BGK model is inadequate in the case of heat transfer ([7]).

This model can be generalized to the case of gaseous mixtures (see Section 2.2.2).

2.2. Gaseous mixtures theory

The kinetic description of a mixture of gases with different particle masses (and possibly with different internal energies) is not a trivial generalization of the classical Boltzmann theory for a single gas since the collision operators have to take into account exchanges of momentum and energy among the different species (and also mass exchanges, in the case of reacting mixtures) ([32]).

2.2.1. General description

In kinetic theory, the evolution of a mixture of N elastically scattering gases, labelled with letter i, is usually described by a set of N integro-differential Boltzmann-type equations for the species distribution functions $f_s(t, \mathbf{x}, \boldsymbol{\xi})$:

$$\frac{\partial f_s}{\partial t} + \boldsymbol{\xi} \cdot \nabla_{\mathbf{x}} f_s = \sum_{r=1}^{N} Q^{sr}(f_s, f_r) \quad s = 1, \ldots, N \tag{2.23}$$

where the collision operator Q^{sr} is given by

$$Q^{sr}(f_s, f_r) = \int_{\mathbb{R}^3} \int_{S^+} \left[f_s(\boldsymbol{\xi}') f_r(\boldsymbol{\xi}'_*) - f_s(\boldsymbol{\xi}) f_r(\boldsymbol{\xi}_*) \right] \mathcal{B}_{sr}(\mathbf{V} \cdot \mathbf{n}, |\mathbf{V}|) d\mathbf{n} d\boldsymbol{\xi}_* \,. \tag{2.24}$$

Here, $\boldsymbol{\xi}$ is the molecular velocity, $\mathcal{B}_{sr}$ is computed from the interaction law between the s-th and r-th species, $\mathbf{V} = \boldsymbol{\xi} - \boldsymbol{\xi}_*$ is the relative velocity of the molecule of the s-th species with respect to a molecule of the r-th species, $\mathbf{n}$ is the unit vector along $\boldsymbol{\xi} - \boldsymbol{\xi}'$, and S^+ is the semisphere defined by $\mathbf{n} \cdot \mathbf{V} \geq 0$. The post-collisional velocities $\boldsymbol{\xi}'$ and $\boldsymbol{\xi}'_*$ are given by

$$\boldsymbol{\xi}' = \boldsymbol{\xi} - 2\frac{\mu^{sr}}{m_s}\mathbf{n}\left[(\boldsymbol{\xi} - \boldsymbol{\xi}_*) \cdot \mathbf{n}\right]$$
$$\boldsymbol{\xi}'_* = \boldsymbol{\xi}_* + 2\frac{\mu^{sr}}{m_r}\mathbf{n}\left[(\boldsymbol{\xi} - \boldsymbol{\xi}_*) \cdot \mathbf{n}\right]$$

where m_s is the mass of the s-th species and $\mu^{sr} = \dfrac{m_s m_r}{m_s + m_r}$ is the reduced mass.

2.2.1.1. Linearization

Repeating the arguments of Section 2.1.3.1, Eqs. (2.23) and (2.24) can be linearized representing the distribution functions of the species as

$$f_s = f_{s,0}(1 + h_s) \quad |h_s| \ll 1 \tag{2.25}$$

with $f_{s,0}$ being the Maxwellian configuration

$$f_{s,0} = n_{s,0}\left(\frac{m_s}{2\pi k_B T_0}\right)^{3/2} \exp\left(-\frac{m_s}{2k_B T_0}\xi^2\right) \tag{2.26}$$

where $n_{s,0}$ the equilibrium number density of the s-th species and T_0 a reference temperature.
The small perturbation h_s satisfies the following Boltzmann equation

$$\frac{\partial h_s}{\partial t} + \boldsymbol{\xi} \cdot \nabla_{\mathbf{x}} h_s = \sum_{r=1}^{N} L^{sr} h_s \quad s = 1, \ldots, N \tag{2.27}$$

where $L^{sr}h_s$ is the linearized collision operator given by

$$\begin{aligned} L^{sr}h_s = n_{r,0}\left(\frac{m_r}{2\pi k_B T_0}\right)^{3/2} \int_{\mathbb{R}^3}\int_{B^+} \left[h_s(\boldsymbol{\xi}') + h_r(\boldsymbol{\xi}'_*) - h_s(\boldsymbol{\xi}) - h_r(\boldsymbol{\xi}_*)\right] \times \\ \times \exp\left(-\frac{m_r}{2k_B T_0}{\xi_*}^2\right) \mathcal{B}_{sr}(\mathbf{V} \cdot \mathbf{n}, |\mathbf{V}|) d\mathbf{n} d\boldsymbol{\xi}_* \\ = \int_{\mathbb{R}^3}\int_{B^+} \left[h_s(\boldsymbol{\xi}') + h_r(\boldsymbol{\xi}'_*) - h_s(\boldsymbol{\xi}) - h_r(\boldsymbol{\xi}_*)\right] f_{r,0} \mathcal{B}_{sr}(\mathbf{V} \cdot \mathbf{n}, |\mathbf{V}|) d\mathbf{n} d\boldsymbol{\xi}_* \,. \end{aligned} \tag{2.28}$$

2.2.2. Kinetic modeling of gas mixtures

We report here the generalization of Section 2.1.5 to the case of gaseous mixtures, and another model, also suitable for mixtures.

2.2.2.1. BGK-type model

In [33], a BGK relaxation model for mixtures was proposed, which satisfies the following properties:

- the correct Boltzmann collision invariants and Maxwellian equilibria are properly recovered;
- the H-theorem is fulfilled;
- the indifferentiability principle holds (when the N gases coincide, the classical BGK model for a single gas is correctly reproduced).

For a mixture of two gases, this BGK model reads as

$$\frac{\partial f_s}{\partial t} + \boldsymbol{\xi} \cdot \nabla_{\mathbf{x}} f_s = \nu_s(\mathcal{M}_s - f_s) \quad s = 1, \dots, N \tag{2.29}$$

where ν_s are suitable collision frequencies (independent from the molecular velocity $\boldsymbol{\xi}$, but possibly dependent on the macroscopic fields) and $\mathcal{M}_s$ are the Maxwellian attractors

$$\mathcal{M}_s = n_s \left(\frac{m_s}{2\pi k_B T_s} \right)^{3/2} \exp\left(-\frac{m_s}{2k_B T_s} |\boldsymbol{\xi} - \mathbf{v}_s|^2 \right) . \tag{2.30}$$

Auxiliary parameters $\mathbf{v}_s$ and T_s are determined in terms of the moments of the distribution functions f_s (that is, the number density n_s, the mass velocity $\mathbf{v}^{(s)}$ and the temperature $T^{(s)}$), by imposing that the exchange rates for species momenta and energies given by the BGK operator reproduce the exact corresponding rates calculated by the Boltzmann collision operators Eq. (2.24) (see [33, 32]).

2.2.2.2. McCormack model

In 1973, McCormack ([34]) presented a simple method of constructing explicit linearized kinetic models, up to a certain order.
For the k-th order model, the method, called *equivalence of moments method*, consists of writing the collision term Eq. (2.28) in the form

$$L^{sr} h_s \approx \hat{L}^{sr}_{(k)} h_s = -\gamma^{sr} h_s(t, \mathbf{x}, \boldsymbol{\xi}) + \sum_{j \leq k} A_j(t, \mathbf{x}) \psi_j(\boldsymbol{\xi}) , \tag{2.31}$$

where γ^{sr} is a constant collision frequency, h_s is the perturbation of the distribution function f_s from the Maxwellian $f_{s,0}$, $f_s = f_{s,0}(1 + h_s)$, and ψ_j is a suitably chosen complete orthonormal set of functions, while the expansion coefficients A_j, $j \leq k$ can be evaluated by equating certain physically significant moments of the model

$$(\Delta\phi)_{M,sr} = \int \phi(\boldsymbol{\xi}) f_{s,0} \hat{L}^{sr}_{(k)} h_s d\boldsymbol{\xi} \tag{2.32}$$

to the corresponding moments of the full linearized collision operator (2.28), calculated with the k-th order approximation to the distribution function.
It automatically gives the correct behaviour in the continuum limit of the k-th order moment of the distribution function: if in Eq. (2.32) k is large enough to include the heat flux moment ($k = 3$ using a particular complete orthonormal set, see [34]), then the correct hydrodynamic behaviour of the model is automatically ensured.
For a third-order model, which is the lowest order that gives a correct hydrodynamic description, the collision term moments corresponding to the species density ($\phi = 1$), drift velocity ($\phi = \xi_i$), energy ($\phi = \frac{1}{2}\xi^2$), stress ($\phi = \xi_i \xi_j - \frac{1}{3}\xi^2 \delta_{ij}$) and heat flux

($\phi = \frac{1}{2}\xi_i\left(\xi^2 - \frac{5}{2}\right)$) have been computed ([35, 36]) by using a third order, thirteen-moment approximation to the distribution function.
The resulting explicit McCormack collision term for a binary mixture reads ([32, 37])

$$\begin{aligned} {Lh^{(1)}}_{MC} = \gamma_1 \Bigg\{ & \rho^{(1)} + 2\left(1 - \eta_{1,2}^{(1)}\right)\mathbf{c}\cdot\mathbf{v}^{(1)} - 2\eta_{1,2}^{(2)}\mathbf{c}\cdot\mathbf{q}^{(1)} + \left[1 - \frac{2\eta_{1,2}^{(1)}M_{12}}{1+M_{12}}\right]\left(|\mathbf{c}|^2 - \frac{3}{2}\right)\tau^{(1)} \\ & + 2\left(1 + \eta_{1,1}^{(4)} - \eta_{1,1}^{(3)} - \eta_{1,2}^{(3)}\right)c_i c_j P_{ij}^{(1)} + \frac{8}{5}\left(1 + \eta_{1,1}^{(6)} - \eta_{1,1}^{(5)} - \eta_{1,2}^{(5)}\right)\left(|\mathbf{c}|^2 - \frac{5}{2}\right)\mathbf{c}\cdot\mathbf{q}^{(1)} \\ & - \eta_{1,2}^{(2)}\left(|\mathbf{c}|^2 - \frac{5}{2}\right)\mathbf{c}\cdot\mathbf{v}^{(1)} + 2\eta_{1,2}^{(1)}\mathbf{c}\cdot\mathbf{v}^{(2)} + 2M_{12}\eta_{1,2}^{(2)}\mathbf{c}\cdot\mathbf{q}^{(2)} + \eta_{1,2}^{(2)}\left(|\mathbf{c}|^2 - \frac{5}{2}\right)\mathbf{c}\cdot\mathbf{v}^{(2)} \\ & + \frac{2\eta_{1,2}^{(1)}M_{12}}{1+M_{12}}\left(|\mathbf{c}|^2 - \frac{3}{2}\right)\tau^{(2)} + \frac{2\eta_{1,2}^{(4)}}{M_{12}}c_i c_j P_{ij}^{(2)} + \frac{8\eta_{1,2}^{(6)}}{5\sqrt{M_{12}}}\left(|\mathbf{c}|^2 - \frac{5}{2}\right)\mathbf{c}\cdot\mathbf{q}^{(2)} - h_1 \Bigg\} \end{aligned} \tag{2.33}$$

$$\begin{aligned} {Lh^{(2)}}_{MC} = \gamma_2 \Bigg\{ & \rho^{(2)} + \frac{2}{M_{12}}\left(1 - \eta_{2,1}^{(1)}\right)\mathbf{c}\cdot\mathbf{v}^{(2)} - \frac{2\eta_{2,1}^{(2)}}{M_{12}}\mathbf{c}\cdot\mathbf{q}^{(2)} + \left[1 - \frac{2\eta_{2,1}^{(1)}}{1+M_{12}}\right]\left(\frac{|\mathbf{c}|^2}{M_{12}} - \frac{3}{2}\right)\tau^{(2)} \\ & + \frac{2}{{M_{12}}^2}\left(1 + \eta_{2,2}^{(4)} - \eta_{2,2}^{(3)} - \eta_{2,1}^{(3)}\right)c_i c_j P_{ij}^{(2)} + \frac{8}{5M_{12}}\left(1 + \eta_{2,2}^{(6)} - \eta_{2,2}^{(5)} - \eta_{2,1}^{(5)}\right)\left(\frac{|\mathbf{c}|^2}{M_{12}} - \frac{5}{2}\right)\mathbf{c}\cdot\mathbf{q}^{(2)} \\ & - \frac{\eta_{2,1}^{(2)}}{M_{12}}\left(\frac{|\mathbf{c}|^2}{M_{12}} - \frac{5}{2}\right)\mathbf{c}\cdot\mathbf{v}^{(2)} + \frac{2\eta_{2,1}^{(1)}}{M_{12}}\mathbf{c}\cdot\mathbf{v}^{(1)} + \frac{2\eta_{2,1}^{(2)}}{{M_{12}}^2}\mathbf{c}\cdot\mathbf{q}^{(1)} + \frac{\eta_{2,1}^{(2)}}{M_{12}}\left(\frac{|\mathbf{c}|^2}{M_{12}} - \frac{5}{2}\right)\mathbf{c}\cdot\mathbf{v}^{(1)} \\ & + \frac{2\eta_{2,1}^{(1)}}{1+M_{12}}\left(\frac{|\mathbf{c}|^2}{M_{12}} - \frac{3}{2}\right)\tau^{(1)} + \frac{2\eta_{2,1}^{(4)}}{M_{12}}c_i c_j P_{ij}^{(1)} + \frac{8\eta_{2,1}^{(6)}}{5\sqrt{M_{12}}}\left(\frac{|\mathbf{c}|^2}{M_{12}} - \frac{5}{2}\right)\mathbf{c}\cdot\mathbf{q}^{(1)} - h_2 \Bigg\} \end{aligned} \tag{2.34}$$

where it should be noted that, in combining the self- and cross-collision terms in Eq. (2.27), the γ coefficients appear only in the combinations $\gamma_1 = \gamma^{11} + \gamma^{12}$ and $\gamma_2 = \gamma^{21} + \gamma^{22}$.
In Eqs. (2.33) and (2.34) the following normalizations have been introduced:

$$\mathbf{c} = \frac{\boldsymbol{\xi}}{\sqrt{2\frac{k_B}{m_1}T_0}} \quad \hat{f}_{1,0} = \frac{f_{1,0}}{n_{1,0}} = \frac{e^{-|\mathbf{c}|^2}}{\pi^{3/2}} \quad \hat{f}_{2,0} = \frac{f_{2,0}}{n_{2,0}} = \frac{e^{-\frac{|\mathbf{c}|^2}{M_{12}}}}{(\pi M_{12})^{3/2}} \tag{2.35}$$

where $M_{12} = m_1/m_2$ is the mass ratio. The other symbols appearing in Eqs. (2.33) and (2.34) are defined in the following:

$$\eta_{s,r}^{(k)} = \frac{\nu_{s,r}^{(k)}}{\gamma_s} \qquad s, r = 1, 2 \quad k = 1, \ldots, 6\,, \tag{2.36}$$

where the collision frequencies are expressed as

$$\gamma_1 = \left(\psi_1\psi_2\nu_{1,2}^{(4)}\nu_{2,1}^{(4)}\right)\left(\psi_2 + \nu_{1,2}^{(4)}\right)^{-1}\,, \tag{2.37}$$

$$\gamma_2 = \left(\psi_1\psi_2\nu_{1,2}^{(4)}\nu_{2,1}^{(4)}\right)\left(\psi_1 + \nu_{2,1}^{(4)}\right)^{-1}\,, \tag{2.38}$$

with

$$\psi_1 = \nu_{1,1}^{(3)} + \nu_{1,2}^{(3)} - \nu_{1,1}^{(4)} \quad \psi_2 = \nu_{2,3}^{(3)} + \nu_{2,1}^{(3)} - \nu_{2,2}^{(4)} \tag{2.39}$$

and

$$\nu_{s,r}^{(1)} = \frac{16}{3}\frac{\mu^{sr}}{m_s} n_r \Omega_{s,r}^{11} \quad \nu_{s,r}^{(2)} = \frac{64}{15}\left(\frac{\mu^{sr}}{m_s}\right)^2 n_r \left(\Omega_{s,r}^{12} - \frac{5}{2}\Omega_{s,r}^{11}\right) \tag{2.40}$$

$$\nu_{s,r}^{(3)} = \frac{16}{5}\left(\frac{\mu^{sr}}{m_s}\right)^2 \frac{m_s}{m_r} n_r \left(\frac{10}{3}\Omega_{s,r}^{11} + \frac{m_r}{m_s}\Omega_{s,r}^{22}\right) \tag{2.41}$$

$$\nu_{s,r}^{(4)} = \frac{64}{15}\left(\frac{\mu^{sr}}{m_s}\right)^2 \frac{m_s}{m_r} n_r \left(\frac{10}{3}\Omega_{s,r}^{11} - \Omega_{s,r}^{22}\right) \tag{2.42}$$

$$\nu_{s,r}^{(5)} = \frac{64}{15}\left(\frac{\mu^{sr}}{m_s}\right)^3 \frac{m_s}{m_r} n_r \Gamma_{s,r}^{(5)} \quad \nu_{s,r}^{(6)} = \frac{64}{15}\left(\frac{\mu^{sr}}{m_s}\right)^3 \left(\frac{m_s}{m_r}\right)^{3/2} n_r \Gamma_{s,r}^{6}\,, \tag{2.43}$$

with

$$\Gamma_{s,r}^{(5)} = \Omega_{s,r}^{22} + \left(\frac{15m_s}{4m_r} + \frac{25m_r}{8m_s}\right)\Omega_{s,r}^{11} - \left(\frac{m_r}{2m_s}\right)\left(5\Omega_{s,r}^{12} - \Omega_{s,r}^{13}\right) \tag{2.44}$$

$$\Gamma_{s,r}^{(6)} = -\Omega_{s,r}^{22} + \frac{55}{8}\Omega_{s,r}^{11} - \frac{5}{2}\Omega_{s,r}^{12} + \frac{1}{2}\Omega_{s,r}^{13}\,. \tag{2.45}$$

$\Omega_{s,r}^{ij}$ are the Chapman-Cowling integrals ([38]), which contain the dependence on the intermolecular interaction potential (see Appendix A for some explicit expression of these quantities for important particular cases).
Furthermore, the dimensionless macroscopic perturbed density $\rho^{(s)}$, velocity $\mathbf{v}^{(s)}$, temperature $T^{(s)}$, stress tensor $P_{ij}^{(s)}$, and heat flux $\mathbf{q}^{(s)}$, appearing in the McCormack model, are defined as follows:

$$\rho^{(1)} = \frac{1}{\pi^{3/2}}\int_{\mathbb{R}^3} h_1 e^{-|\mathbf{c}|^2} d\mathbf{c} \quad \rho^{(2)} = \frac{1}{(\pi M_{12})^{3/2}}\int_{\mathbb{R}^3} h_2 e^{-\frac{|\mathbf{c}|^2}{M_{12}}} d\mathbf{c} \tag{2.46}$$

$$\mathbf{v}^{(1)} = \frac{1}{\pi^{3/2}}\int_{\mathbb{R}^3} \mathbf{c} h_1 e^{-|\mathbf{c}|^2} d\mathbf{c} \quad \mathbf{v}^{(2)} = \frac{1}{(\pi M_{12})^{3/2}}\int_{\mathbb{R}^3} \mathbf{c} h_2 e^{-\frac{|\mathbf{c}|^2}{M_{12}}} d\mathbf{c} \tag{2.47}$$

$$\tau^{(1)} = \frac{1}{\pi^{3/2}}\int_{\mathbb{R}^3} \left(\frac{2}{3}|\mathbf{c}|^2 - 1\right) h_1 e^{-|\mathbf{c}|^2} d\mathbf{c} \quad \tau^{(2)} = \frac{1}{(\pi M_{12})^{3/2}}\int_{\mathbb{R}^3} \left(\frac{2}{3M_{12}}|\mathbf{c}|^2 - 1\right) h_2 e^{-\frac{|\mathbf{c}|^2}{M_{12}}} d\mathbf{c} \tag{2.48}$$

$$P_{ij}^{(1)} = \frac{1}{\pi^{3/2}}\int_{\mathbb{R}^3} \left(c_i c_j - \frac{1}{3}|\mathbf{c}|^2\delta_{ij}\right) h_1 e^{-|\mathbf{c}|^2} d\mathbf{c} \quad P_{ij}^{(2)} = \frac{1}{(\pi M_{12})^{3/2}}\int_{\mathbb{R}^3} \left(c_i c_j - \frac{1}{3}|\mathbf{c}|^2\delta_{ij}\right) h_2 e^{-\frac{|\mathbf{c}|^2}{M_{12}}} d\mathbf{c} \tag{2.49}$$

$$\mathbf{q}^{(1)} = \frac{1}{\pi^{3/2}}\int_{\mathbb{R}^3} \frac{1}{2}\mathbf{c}\left(|\mathbf{c}|^2 - \frac{5}{2}\right) h_1 e^{-|\mathbf{c}|^2} d\mathbf{c} \quad \mathbf{q}^{(2)} = \frac{1}{(\pi M_{12})^{3/2}}\int_{\mathbb{R}^3} \frac{1}{2}\mathbf{c}\left(\frac{|\mathbf{c}|^2}{M_{12}} - \frac{5}{2}\right) h_2 e^{-\frac{|\mathbf{c}|^2}{M_{12}}} d\mathbf{c} \tag{2.50}$$

2.3. The Knudsen pump and the TPD exponent

With the fast progress in micro/nanoscale devices and components, it is desired to obtain fundamental understanding of the transport phenomena in these devices. Additionally, a deep understanding of the hydrodynamics and thermal physics of rarefied gas flows is crucial in design, fabrication and operation of MEMS/NEMS. For this reason, the flow analysis should be performed using accurate approaches based on the solution

of the Boltzmann equation ([39]). In particular, thermally driven mass flows, which are peculiar to rarefied gases (or gases in the kinetic regime), have potential applicability as non-mechanical controllers of mass and energy flow rates in micro/nano-channels ([40]). As thermally driven flows, mention should be made of the thermal creep flow, or thermal transpiration, which is a flow along the non-uniformly heated wall in the direction of the gradient of the temperature. It is a classical phenomenon in rarefied flows and has been investigated by many scientists. A notable application of this flow is the Knudsen pump or compressor and its variants, which therefore, unlike most conventional pumps, do not require moving parts or supplementary pumping fluids ([41]).

The phenomenon of thermal transpiration was originally investigated experimentally by Reynolds in 1880, based on earlier experimental observations from 1831 to 1863 by Graham. It is used to describe what occurs in transitional rarefied flows, primarily along walls with a superimposed wall surface temperature gradient. Substantially diffuse and thermally accommodated reflections are required at the surface for thermal creep to be significant. As we shall see in more detail, thermal creep flow is from the cold end of a tube toward the hot end. For free molecular flow, thermal creep flow will fill the entire tube, while in the case of transitional flow, the thermal creep occurs closer to the tube's walls ([41]). As a consequence of the cold to hot flow, a pressure difference between the hot and cold ends can be established and a pressure return flow will occur, partially or completely balancing the thermal creep flow. Thus, thermal creep can produce both a net gas flow and a pressure difference, which are the requirements for a pump.

Micro/mesoscale gas pumps are essential for the realization of completely miniaturized devices such as gas sensors, fuel cells, and lab-on-a-chip systems. Numerous microscale gas pumps have been proposed and studied. Some microscale pumps have been developed as simple scaled-down versions of conventional macroscale pumps. Nonetheless, in other cases unconventional pumping techniques have been investigated for unique application to microscale pumping needs, since only a few types of vacuum pump scale well to small dimensions. Moreover, most vacuum pumps also have complicated machinery that does not scale well to microfabrication by planar techniques. Thermal molecular pumps can serve this purpose: they are well-suited for miniaturization because efficiency improves with surface-to-volume ratio, and they have no valves that must seal.
Among the different kinds of thermal molecular pumps, the Knudsen pump, or Knudsen compressor, a solid-state micro/mesoscale gas pump with no moving parts, provides the highest compression ratio and its performance is independent of the material surface conditions. Invented almost a century ago, the Knudsen pump was long regarded as a relatively inefficient option for achieving high vacuum, despite its attractive feature of no moving parts. In theory, the Knudsen pump has many potential advantages, such as high reliability and the ability to efficiently pump light gases, such as hydrogen and helium, which many types of pumps do not pump well. A barrier to acceptance has been that sub-micron feature sizes are required for the pump to operate at atmospheric pressure. Nonetheless, the evolution of micromachining technology has rekindled interest in this kind of pump.

2.3.1. The Knudsen number

Rarefied gas flows are mainly found in small-scale flow fields and/or low-pressure environments. The characteristic number that determines the degree of rarefaction and the area in which continuum model equations are valid is the **Knudsen number** (Kn), which is defined by the relationship

$$Kn = \frac{\lambda}{L} \tag{2.51}$$

where λ is the mean free path of the particles and L is a characteristic dimension of the problem (e.g., the distance between two parallel plates, o the radius of a pipe).
The mean free path cannot be measured directly and may be calculated on the basis of measured macroscopic quantities in accordance to the relationship ([42])

$$\lambda = \frac{\sqrt{\pi}\mu}{2p} v_0 \,, \tag{2.52}$$

where p is the local pressure, μ the dynamic viscosity at local temperature T, and

$$v_0 = \sqrt{\frac{2k_B T}{m}} = \sqrt{2RT} \tag{2.53}$$

is the most probable velocity (valid for the hard-sphere model). Thus, for some given gas, the Knudsen number is a function of the pressure and temperature: $Kn = Kn(p, T)$.
Also, the **gas rarefaction parameter** δ is frequently used, which is linked to the Knudsen number as follows ([42]):

$$\delta = \frac{\sqrt{\pi}}{2} \frac{1}{Kn} \,. \tag{2.54}$$

The value of Kn (or, equivalently, δ) characterizes the flow of gas: in particular, the local value of the Knudsen number in a certain flow determines the **degree of rarefaction** of the flow itself, and hence the validity of the continuum model. In general: in the limit of a zero Knudsen number, the mean free path is zero, i.e., for $p \neq 0$ the viscosity is zero and then the Navier-Stokes equations reduce to the inviscid Euler equations; as Kn increases, rarefaction effects become more important and, eventually, the Navier-Stokes equations break down.
The different Knudsen number regimes can be summarized as follows (see, e.g., [43]):

- $Kn < 0.001$ ($\delta > 1000$): hydrodynamic regime. The mean free path is so small that the flow is dominated by collisions between gas molecules, the gas can be considered as a continuous medium and the Navier-Stokes equations are applicable, coupled with no-slip boundary conditions;

- $0.001 < Kn < 0.1$ ($1000 > \delta > 10$): slip regime. Non-equilibrium phenomena start manifesting in the boundary regions of the domain. In particular, velocity slip and temperature jump are observed on the walls: Navier-Stokes equations are applicable, but with suitable slip boundary conditions;

- $0.1 < Kn < 10$ ($10 > \delta > 0.1$): transition regime. A kinetic description of the gas is necessary, since intermolecular collisions are reduced: the Boltzmann equation is valid here;

- $Kn > 10$ ($\delta < 0.1$): free-molecular regime. The mean free path is so large that the collisions of molecules with the boundary walls occur much more frequently than the collisions between molecules: under this condition we may discount the intermolecular collisions and consider that every molecule undergoes ballistic motion and moves independently of each other, remaining unaffected by other molecules.

This division of the regimes of flow, although only qualitative and not strictly rigorous, is very useful because it suggests the most effective methods to be used for calculation of the gas flows.

In the hydrodynamic regime, classical hydrodynamics prevails, with well-known effects such as stresses caused by velocity gradients, as expressed in the Navier-Stokes law, and heat flux caused by temperature gradients, as expressed in Fourier's law. When, however, the Knudsen number becomes larger, so-called *rarefaction effects* influence the flow.
Moreover, also the interaction between gas and solid boundaries depends on the degree of rarefaction. In classical hydrodynamics, one commonly assumes no-slip and no-jump boundary conditions, where the gas at the wall assumes velocity and temperature of the wall. Rarefaction leads to non-equilibrium phenomena and deviations from this behaviour, so that the gas experiences velocity slip and temperature jump at the wall: the gas and the wall surface do not have the same velocity and temperature, secondary flows are induced by temperature gradients (or concentration gradients for mixtures), and so on.
These phenomena cannot be captured by the classical hydrodynamic equations and can be examined via the kinetic theory of gases, in which the problem is correctly described by the Boltzmann equation.

2.3.1.1. Slip regime and boundary conditions

In the slip regime non-equilibrium phenomena begin to influence the global gas flow. Anyway, they are not predominant yet, and the continuum description can still be exploited, as long as some corrections are introduced: in particular, the Navier-Sokes equations are still usable, if coupled with **slip boundary conditions**.
For pressure-driven flows, assuming a first-order boundary condition at a flat wall, in the isothermal case, the slip velocity reads as

$$v_s^P = A_P \lambda \left(\frac{\partial v}{\partial x} \right)_w , \tag{2.55}$$

where A_P is called **viscous slip coefficient**, x is the coordinate normal to the wall and λ is the mean free path.
Likewise, for thermal-driven flows one can write the following first-order slip boundary condition on a flat wall:

$$v_s^T = A_T \frac{\mu}{\rho T} \left(\frac{\partial T}{\partial z} \right)_w , \tag{2.56}$$

where A_T is called **thermal slip coefficient**, z is the longitudinal coordinate, μ is the gas viscosity and ρ is the density. In both cases, the subscript $_w$ means that the gradients are evaluated at the wall.
It is generally accepted that the classical hydrodynamical equations can supply realistic

results well beyond the slip region, provided that higher-order boundary conditions are employed (see [27, 28]); explicitly:

$$v_s^P = A_1^P \lambda \left(\frac{\partial v}{\partial x}\right)_w - A_2^P \lambda^2 \left(\frac{\partial^2 v}{\partial x^2}\right)_w \tag{2.57}$$

and

$$v_s^T = A_1^T \frac{\mu}{\rho T} \left(\frac{\partial T}{\partial z}\right)_w + A_2^T \frac{\mu^2}{\rho^2 T} \left(\frac{\partial^2 T}{\partial z^2}\right)_w , \tag{2.58}$$

where A_1^P and A_2^P are the first- and second-order viscous slip coefficients, A_1^T and A_2^T are the first- and second-order thermal slip coefficients, respectively.
We may refer to the domain of validity of this second-order slip model as *"extended" slip regime*.

2.3.2. The thermal creep

In the framework of classical fluid dynamics, there is no time-independent flow induced by virtue of only the temperture field without external forces such as gravity and pressure ([43]). Nonetheless, in rarefied gases, the temperature field plays an important role in inducing time-independent flows. Among the various types of thermally induced flows, nowadays, the theories and applications of the thermal creep effect seem to be the richest.

Thermal creep flow (also known as **thermal transpiration flow**) is the macroscopic movement of a rarefied gas induced by a temperature gradient.
It is a particularly interesting boundary effect, where a velocity slip is induced by a temperature gradient in the wall, i.e., the gas is forced into motion at the boundary by a non-uniform temperature distribution in the boundary itself. This simple condition induces a tangential creep velocity in the interior gas close to the walls such that the gas flows in the direction of the temperature gradient, i.e., from cold to hot (as in Fig. 2.1).

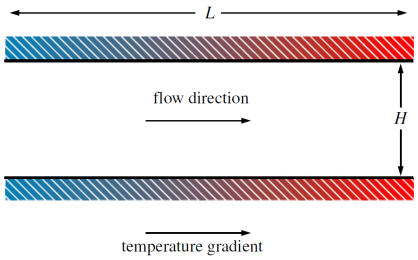

Figure 2.1.: Flow setting in thermal transpiration flow ([44]).

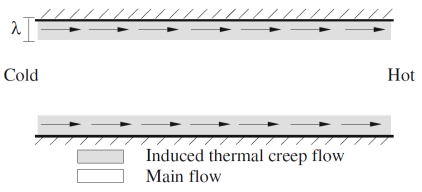

Figure 2.2.: Thermal creep flow is induced primarily near the walls ([39]).

This thermally induced velocity initiates within a thin boundary layer, and the thickness of this creep layer is proportional to the Knudsen number ([39, 44]), as represented in Fig. 2.2. Therefore, thermal creep effect can occur in a perceptible way only in sufficiently rarefied flows. In this case and, for example, in sufficiently long channels, the velocity gradient within the creep layer might fill the whole channel width, as the result of shear stress diffusion. (It may be worth noting that some authors use the nomenclature "thermal transpiration flow", instead of "thermal creep",

only for the situation in which the thermal creep layer fills the entire channel. Anyway, as in most of the literature, we will use the two terms with no distinction.)
Thermal creep problem is investigated by several authors using kinetic models of the Boltzmann equation. The flow between two parallel plates, where a constant unidimensional temperature gradient is applied to the plates, is a common flow configuration which is used in kinetic approaches.

This phenomenon was first reported in 1879 by Reynolds as an experimental result, and called "thermal transpiration flow" ([45]). In an investigation with a porous plate separating two gas regions, maintained at different temperatures T_c and T_h, he showed that at very low densities the equilibrium pressures on the two sides are related by the law

$$\frac{p_h}{p_c} = \sqrt{\frac{T_h}{T_c}}\,. \tag{2.59}$$

Almost at the same time, Maxwell ([23]) investigated the problem from a theoretical point of view, studying the stresses in an unequally heated stationary mass of gas, in order to provide a physical explanation for this problem. At an unequally heated boundary of the gas, Maxwell showed that a special effect was to be expected in the form of a steady creep of the gas over the surface from colder to hotter regions.

Later experimental observations by Knudsen (in 1909-1910) proved the existence of a pumping effect in thermal creep flows using experimental observations ([46, 47]). Knudsen's research led to the supposition that Eq. (2.59) was valid only at a zero-flow final equilibrium state, which followed a transitional stage of gas displacement.

Figure 2.3.: Gas at rest with a temperature gradient ([43]).

To explain the physical mechanism of thermal creep flow ([19, 43, 48, 49]), we consider the static gas on a wall with a temperature gradient (Fig. 2.3). Take a small area dS of the wall, and consider the momentum transferred to dS when gas molecules impinge on it. The molecules impinging on dS come from various directions directly (or without molecular collisions) over a distance of the order of the mean free path, keeping the property of their origins. Since the molecules coming from the hotter region have a larger average speed than the molecules coming from the colder region, the momentum transferred to dS (or wall) by the molecules impinging on it has a tangential component in the direction opposite to the temperature gradient on the wall. More precisely, in a static gas, the number of molecules in the colder region is larger than that in the hotter region (the molecular density in the hotter region is smaller), but the molecules from these two regions impinging on dS per unit time are the same. Moreover, the molecules from the hotter region have a larger average speed. Thus, the momentum transferred to dS by the molecules impinging on it has a tangential component in the direction opposite to the temperature gradient. Note that, for the diffuse reflection, the contribution of the molecules leaving the wall to the tangential component of the momentum transfer is highly small (almost zero). (Generally, except in the specular reflection, the velocity distribution function of the molecules leaving the wall, characterized by the wall condition, is qualitatively different from that of the impinging molecules, formed

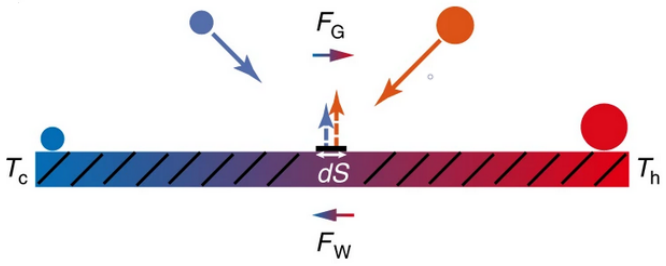

Figure 2.4.: Scheme of the physical mechanism of thermal creep phenomenon ([43]).

by collisions of surrounding gas molecules. Thus the two contributions are generally different.) Summarizing, a net force (F_W in Fig. 2.4) towards the colder region is produced by the molecules on the wall. Therefore, the gas is subjected to a reaction force acting in the direction of the temperature gradient (F_G in Fig. 2.4) according to Newton's third law, and a gas flow results in this direction. Finally, in a gas in motion, a momentum in the direction of motion is transferred to the wall or dS. Thus, a time-independent flow is established when the two contributions of momentum transfer balance.
Obviously from the above explanation, the boundary (or, more precisely, the qualitative difference of the velocity distribution functions of the molecules impinging on the boundary and those leaving there) plays an essential role in inducing the thermal creep flow. For example, if the gas molecules impinge on a VDM (velocity dependent Maxwell) wall boundary, inverted thermal creep flow will be produced with a flow direction opposite to that of thermal creep flow (see [43]). Note that the inverted thermal creep is only observed theoretically ([50]), has not yet been verified in experiments.

Thermal creep will obviously have an effect upon the motion of gases in tubes, and in some cases this may be of practical importance. If the tube is unequally heated, there may be a *resulting flow of gas* along it, even in the absence of a pressure gradient; or, if the circumstances are such as to prevent such a flow (e.g., the system is closed), then a *steady pressure gradient* may be set up with the gas at rest. Measurements of gaseous pressure by means of external gauges at a different temperature may require correction for pressure differences arising in this way in the connecting tubes ([48]).

2.3.2.1. Cross effects and Onsager relations

It has been noted that the consideration of rarefied slip flow in the boundary conditions can introduce large deviations of transport in conditions of thermal and pressure gradients when compared to a classical no-slip treatment. In addition to the direct thermal and mass fluxes caused by thermal and pressure gradients, mass and heat transport cross terms given by the **mechanocaloric effect** and **thermal transpiration** are present. These cross effect terms are defined by the mass flux transport due to a temperature gradient (thermal transpiration) and heat flux due to a pressure gradient (mechanocaloric effect). In the continuum limit, where the mean free path of the gas is much less than the characteristic dimension, these cross effects disappear. In the transition region and free molecular region, where the mean free path of the gas becomes on the same order of the characteristic dimension or greater, these effects become significant.

The cross phenomena of thermal transpiration and mechanocaloric effect constitute an interesting and simple problem for the illustration of Onsager's ideas ([51]). Physically, we consider the flow and heat transfer in a gas in two vessels that are connected by a capillary. In vessel 1, the gas is maintained at a pressure p and a temperature T, while in vessel 2 the respective values of these parameters are $p+\Delta p$ and $T+\Delta T$. Now, if J_M and J_Q are, respectively, the mass flux (mass/time) and the heat flux (energy/time) through the capillary, then, by the principles of non-equilibrium thermodynamics ([52]):

$$J_M = \gamma_{MM} x_M + \gamma_{MQ} x_Q \tag{2.60}$$

$$J_Q = \gamma_{QM} x_M + \gamma_{QQ} x_Q \tag{2.61}$$

where the phenomenological **kinetic coefficients** γ form a positive matrix, and have the Onsager reciprocity relation $\gamma_{MQ} = \gamma_{QM}$. The driving terms x are given by (ρ indicates the density)

$$x_M = -\frac{1}{\rho T}\Delta p \tag{2.62}$$

$$x_Q = -\frac{1}{T^2}\Delta T \tag{2.63}$$

Thus, the thermodynamic results clearly indicate that, in general, there exists a mass flux due to a temperature gradient and a heat flux due to a pressure gradient. It is also well-known that in the continuum limit $\gamma_{MQ}, \gamma_{QM} = 0$ and that the cross effects become important only in the transition region and the free molecular limit.

We assume now parallel plates, BGK model, diffuse reflection boundary conditions. The various phenomenological coefficients can be more conveniently expressed in the following non-dimensional forms:

$$\mathcal{J}_{MM} = 2\left(\frac{m}{2k_B T_0}\right)^{1/2} \frac{p_0}{T_0 {\rho_0}^2 \tilde{\delta}^2}\gamma_{MM} \tag{2.64}$$

$$\mathcal{J}_{MQ} = 2\left(\frac{m}{2k_B T_0}\right)^{1/2} \frac{1}{T_0 \rho_0 \tilde{\delta}^2}\gamma_{MQ} \tag{2.65}$$

$$\mathcal{J}_{QQ} = 2\left(\frac{m}{2k_B T_0}\right)^{1/2} \frac{1}{p_0 T_0 \tilde{\delta}^2}\gamma_{QQ} \tag{2.66}$$

where subscript 0 indicates some mean value of the corresponding parameter and $\tilde{\delta} = \delta/\lambda$. Then, it is observed that ([53]):

- $\mathcal{J}_{MM}$ clearly exhibits a minimum at $\delta \approx 1$ (the so-called Knudsen minimum, see [54]);
- $\mathcal{J}_{MQ}$ diminishes monotonically with increasing δ and vanishes as $\delta \to \infty$, i.e., in the continuum limit both the thermal transpiration and the mechanocaloric effect vanish;
- for $\delta \to 0$ it is shown that $\mathcal{J}_{MQ} = \frac{1}{2}\mathcal{J}_{MM}$ which, under the condition $J_M = 0$, gives the well-known result $(p_1/p_2) = (T_1/T_2)^{1/2}$ (Eq. (2.59)).

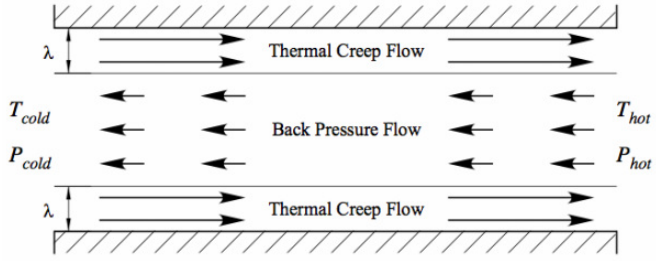

Figure 2.6.: Scheme of the steady state of the thermal creep flow: the flow near the wall is maintained by the temperature gradient at the boundary, the bulk flow is due to the pressure gradient generated during the transient phase and maintained at the steady state.

2.3.2.2. The thermomolecular pressure difference

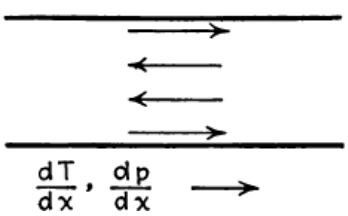

Figure 2.5.: Temperature gradient on the wall and consequent pressure gradient ([48]).

Let us consider two vessels containing the same gas at different temperatures T_1, T_2 and connected by a capillary. To maintain the temperature difference between the vessels, the gas begins to move from the cold vessel to the hot one even when there is no pressure drop ([55]). If the system is closed, a pressure drop, called **thermomolecular pressure difference** (**TPD**), is established between the vessels (Fig. 2.5). The pressure drop causes a gas flow which is opposite to the thermal creep (**TPD effect**) so that the whole mass flow through the capillary vanishes in the stationary state (**TPD state**). Fig. 2.6 depicts the situation. Practically, we have that the gas is creeping steadily along the walls of the tube and is at the same time flowing back through the central part; the TPD is necessary in order to maintain the return flow and is the maximum pressure drop that the imposed temperature gradient can maintain at the steady state.

The TPD effect is very important in engineering practice, because in many studies it is necessary to calculate the pressure p_1 in a chamber at a given temperature T_1 from a measured pressure p_2 in another chamber at a given temperature T_2: if the chambers are joined by a capillary and the relation of p_1 with p_2, T_1, and T_2 is known, one easily obtains p_1. The scientific importance of the effect is also great because it is sensitive to many properties of the gas: viscosity, thermal conductivity, gas-surface interaction, etc. So it can be used to verify a validity of kinetic models describing both gas-gas and gas-surface interactions. TPD measurements can be used to calculate several thermal properties of polyatomic gases as well.
Thus, due to the great practical and scientific importance, the thermal transpiration phenomena continue to attract the attention of theoretical and experimental researchers as well.

The relation between p_1, p_2, T_1, and T_2 in a general form can be written as ([42, 55, 56, 57, 58])

$$\frac{p_1}{p_2} = \left(\frac{T_1}{T_2}\right)^{\gamma}, \tag{2.67}$$

where the coefficient γ, called **TPD exponent**, depends on many factors, such as geometry of the capillary, type of the gas, nature of the gas-surface interaction. But the

coefficient γ also significantly depends on Kn (and thus also on p and T).

In order to derive a particular expression for γ, let us consider the flow of a rarefied monatomic gas through a cross section of a long capillary caused by longitudinal pressure and temperature gradients. We assume that these gradients are so small that the reduced mass flow rate G can be split into two independent parts as ([55, 59])

$$G = -G_P \kappa + G_T \tau \tag{2.68}$$

with

$$\kappa = \frac{L}{p}\frac{\partial p}{\partial z} \qquad \tau = \frac{L}{T}\frac{\partial T}{\partial z} \tag{2.69}$$

where z is the longitudinal coordinate. The coefficients G_P and G_T are determined only by the local Knudsen number $Kn = Kn(p, T)$ and do not depend on the gradients. If the pressure and temperature drops are small we may consider that these coefficients do not vary along the capillary.
To find the coefficient γ we assume to be in the TPD state, so we put $G = 0$ in Eq. (2.68): integrating it with respect to z, it is easily obtained that

$$\gamma = \frac{G_T}{G_P}\,. \tag{2.70}$$

As already said, γ depends strongly on the rarefaction parameter. In particular: as δ is increased, γ is decreased, since as the atmosphere becomes more dense the thermal creep flow is decreased and therefore larger temperature drops are needed to maintain the no-net flow condition; and viceversa, as δ decreases, γ increases, since in highly rarefied atmospheres the effect of the thermal creep flow is significant and larger pressure drops are needed to counterbalance this flow. Therefore, γ *should be monotonically decreasing as* δ *increases*. We can state precisely the two limiting cases ([53]):

- in the continuum limit we have $\gamma \to 0$ (the cross effects vanish);
- in the free molecular limit we have $\gamma \to 1/2$ (as in Eq. (2.59)) .

It should be noted that, even for cases where the mass flow rate is zero, if Kn is finite then $\gamma < 1/2$ ([9]).

2.3.3. The Knudsen pump

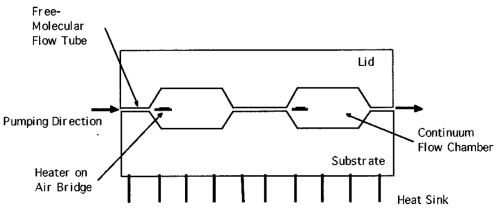

Figure 2.7.: Cross-sectional schematic of a MEMS fabricated thermal transpiration pump ([9]).

In recent years, the advent of MEMS made way for new perspectives on thermal transpiration. The interest in temperature induced flows has grown in connection with micromachine engineering, since a pumping system making use of this kind of flow has no moving parts and no mixing process or working fluids. The possibility of using the pumping effect of thermal transpiration to create a microcompressor without moving parts led to various experimental works by several researchers,

in which the attention is mainly focused on the pressure increase due to the application of a temperature gradient along the channel.

The **Knudsen pump** (**KP**) is a kind of vacuum pump that, working by the principle of thermal transpiration, can form thermally induced flows in rarefied gas environments. It has the advantages of having no moving parts (and hence high reliability), simple structure, easy construction and extension, a wide range of energy sources and low energy consumption. With the development of MEMS and NEMS, extensive studies have been conducted on KPs, and their applications have widened.
Potential applications for the Knudsen pump with respect to sensors include chemical preconcentration, gas chromatography and spectroscopy. Other microfluidic applications include moving gases on chips and providing power for microactuators. The pump is also conducive to passive applications such as power scavenging since it has no moving parts and is powered by a thermal gradient. A particularly interesting application is forced convection cooling: the heat of the surface provides the energy to power the pump while the pump cools this surface.

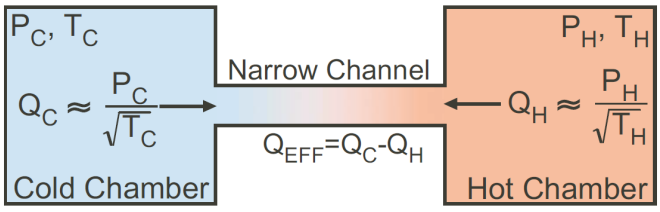

Figure 2.8.: If two chambers are connected by a channel that restricts flow to the free-molecular regime, the ratio of pressures at equilibrium is nominally equal to the ratio of the square root of their absolute temperatures ([60]).

A basic configuration of a KP consists of two chambers, maintained at different temperatures, connected by a narrow channel that restricts gas flow to the free-molecular regime (Fig. 2.8). Due to the temperature gradient along the channel walls, the gas starts flowing from the colder region to the hotter one until equilibrium is reached: at this point, a pressure increase is established from the colder region to the hotter one.

2.3.3.1. Cascading of KPs

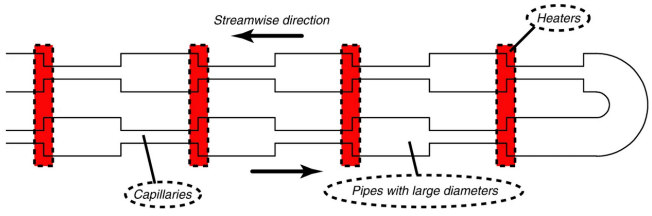

Figure 2.9.: Model of an early thermal creep flow KP ([46, 43]).

As demonstrated by Knudsen, a straightforward generalization of the basic "single-stage" KP is a periodic structure consisting of alternately arranged narrow and wide pipes (tubes and volumes). The result is a KP able to generate large changes in pressure by utilizing a cascade of multiple stages. Referring to Fig. 2.9, each stage is composed of two parts:

- a *capillary*, between the cold inlet chamber and the heated chamber, is where the

pressure change occurs: here a temperature increase, produced by a heater, results in a pressure increase due to the thermal transpiration, which is the dominant mass flow phenomenon;

- a *connector section* (e.g., a larger tube), dominated by pressure flow, in which the pressure is approximately constant, used to transport the gas to the next stage.

In order to have a working pump, from a purely theoretical point of view, the behaviour of the temperature in the connector sections is not so important.
However, some observations have to be made, in order to improve the behaviour and efficiency of this design:

- it is fundamental to maintain a flow as rarefied as possible in the capillaries (to guarantee an effective thermal creep);

- it is desirable not to deal with (too high temperatures or) too high temperature differences (which are not efficiently maintained).

The second point is easily satisfied by imposing a temperature decrease along the connector, usually to return the gas to its original temperature prior to entering the next stage. For example, it can be done with a periodic temperature with the same period as the structure, such as a sawtooth distribution increasing in the narrow segments and decreasing in the wide segments (see Fig. 2.10). This is done to facilitate the cascade of stages that comprise a KP: as it enters the cold-side end of the next stage's capillary, the working gas is at a manageable temperature, assuring that a maximum temperature difference is available to drive the thermal creep flow. The result is the achievement of a required pressure increase for a specified upflow, without a net change in the temperature of the working gas.

If a negative temperature gradient along the wall of the hot-side connector section is imposed, it does not cause a significant decrease of the stage exit pressure, but only if the flow regime is sufficiently far from the free-molecular regime. If this is not true, a "reverse" thermal creep flow may occur, i.e., in the opposite direction as the primary thermal creep. However, since the dimensions of the connector section are larger than those of the narrow channel, the flow regime in the connector section is less rarefied than in the membrane channels: as a result, the reverse thermal creep flow in the connector section is of reduced relative effectiveness compared to the creep in the narrow channel.

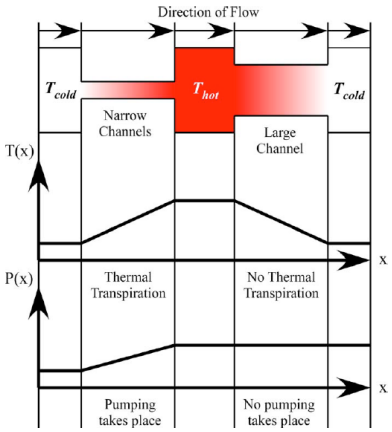

Figure 2.10.: Schematic of the KP with a periodic temperature distribution ([61]).

By this means, a significant pressure rise can be accomplished, since for N stages the total pressure ratio goes as

$$\frac{p_h}{p_c} = \sqrt{\left(\frac{T_h}{T_c}\right)^N}. \tag{2.71}$$

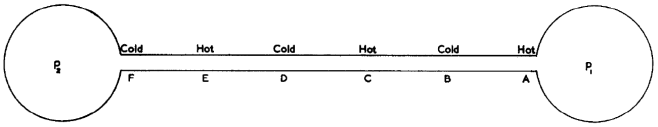

Figure 2.11.: Thermal transpiration in a tube with alternating hot and cold surfaces: the result is a "useless cascade" ([62]).

Note that simply imposing a periodic temperature distribution on a tube with constant cross section, as shown in Fig. 2.11 (where flow is from left to right), would be useless since, though pressure drops would be established from right to left in sections AB, CD and EF, the effect would be reversed in sections BC and DE. The result would be a one-stage device with the pressure ratio set by the temperature ratio between A and F.

Another interesting improvement is about the throughput. One may reasonably argue that, with this setup, the throughput of this pump is too low, because of the bottleneck given by the narrow channel. In order that the throughput of the pump is not too small, the capillaries should be as large in cross-sectional area as possible. Nonetheless, this fact clashes with the requirement that molecular flow be established in them. Baum overcame this by making the tube annular in cross section; thus its area was large while its width was small ([62]). The cross section of such a pump would look like in Fig. 2.12. In place of a single capillary, we have a membrane consisting of a parallel array of small gas flow channels: this maintains in the capillary section practically the same cross-section area (and so throughput) as in the connector section and a relatively large mean free path.

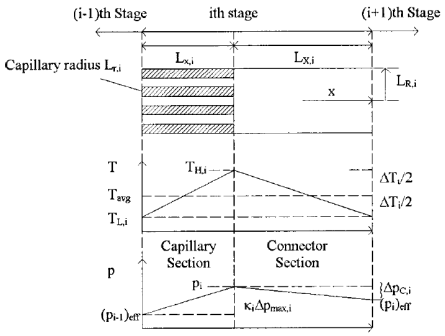

Figure 2.12.: Illustrative i-th stage of a cascaded KP ([63, 64, 41]).

Two further remarks:

- the basic single-stage KP can be easily arrayed, rather than cascaded: this would improve the throughput, instead of the pressure ratio;
- as correctly shown in Fig. 2.12, there is actually a drop of pressure in the connector stage, which is obviously needed to drive the viscous flow: anyway, it is negligible with respect to the pressure increase obtained in the capillary.

2.3.3.2. Working pressure

Another general feature of such pumps is that they have specific and rigorous requirements about the value of pressure with which they work. In particular, these pumps generally have an upper and a lower pressure limit, which have to be respected in order to have an efficient device, or even to guarantee a proper functioning. This is due to the fact that the channels in a KP must operate in the proper flow regime: ideally, the

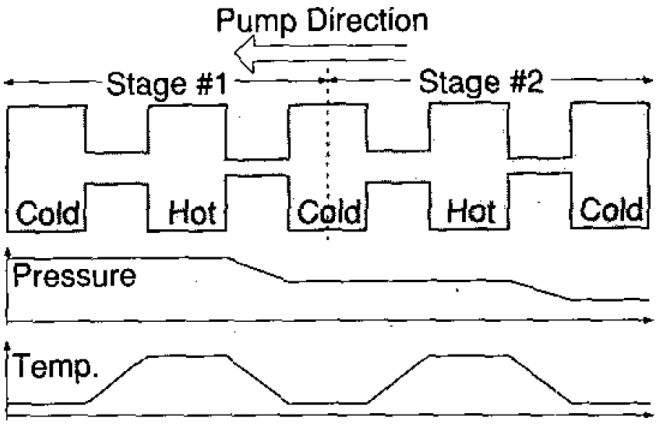

Figure 2.13.: A two-stage Knudsen pump which alternates hot and cold chambers with a periodic temperature distribution ([65]). Note that the channels connecting the chambers have different hydraulic radii: one is the capillary, and one is part of the connector.

narrow channels should have a hydraulic diameter less than 1/10 of the mean free path of the gas (free-molecular flow regime, $Kn > 10$) and the wide channels should have a hydraulic diameter greater than 20 times the mean free path of the gas (viscous flow regime, $Kn < 0.05$). While these conditions can be closely matched in laboratory compressors, it is expected in practice that both the capillary and connector sections of the compressor frequently will operate in the transitional flow regime ($0.05 < Kn < 10$), with a possible loss of compression.
These observations imply that:

- upper pressure limit, reached when the backing pressure (that is, the starting pressure) is such that the gas mean free path is less than the width of the capillary, is determined by the hydraulic diameter of the narrow channels: the smaller the narrow channels are, the higher the operating pressure can be;

- lower pressure limit, reached when the backing pressure is such that the ultimate pressure of the pump is below the limiting pressure, (i.e., when molecular flow begins to occur in the intermediate volumes), is determined by the hydraulic diameter of the wide channels: the larger the wide channels are, the lower the attainable pressure is.

For example (see [65]), the maximum height of the narrow channels is 6 nm if operation in the free molecular flow regime is to be achieved because the mean free path of air is approximately 60 nm at STP (standard temperature and pressure). This small dimension makes it more convenient to design a Knudsen pump that operates in the transition flow regime at its input stage for atmospheric operation.

This is the reason why the upper pressure limits of these pumps have been determined by the microfabrication limits of the day: they have operated at relatively low pressures, with low throughputs, and have not become main line pumps for a long time. In recent years, MEMS have introduced a whole new level of miniaturization to devices in general, including vacuum devices, and hence have raised the upper pressure limits, and thus the throughputs of thermal molecular pumps to atmospheric levels.

2.3.3.3. Other examples of Knudsen pumps

The flow of a gas in a grooved channel (Fig. 2.14a), due to an imposed temperature gradient in the longitudinal direction, has also been investigated ([66]). This flow has common characteristics with the classical Poiseuille flow and is found in thermal creep problems, but the presence of rectangular grooves that are placed periodically in one of the two stationary walls, results in a two dimensional flow pattern.
The feasibility of making a Knudsen pump by using a two-dimensional channel with a "snaky" shape has also been investigated ([67]). The channel is composed of alternately arranged straight and semicircular segments, with a periodic temperature distribution (Fig. 2.14b).

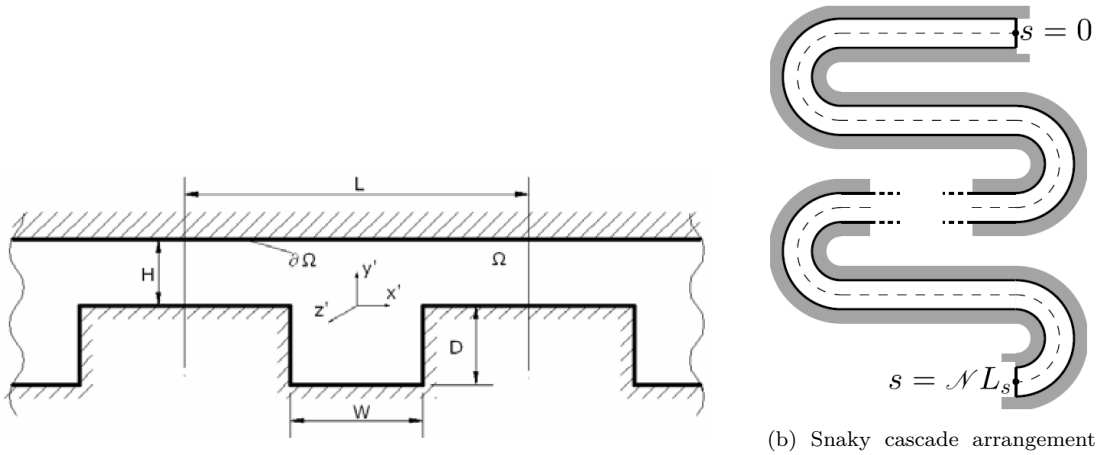

(a) Grooved configuration for the KP ([66]).

(b) Snaky cascade arrangement for the KP ([67]).

Figure 2.14.: Some more involved KP designs.

A slight variation of the implementation in Fig. 2.10 is given in [68] (see Fig. 2.15). The length of the hot chamber is set to zero, so the setup is the following. The pump consists of two reservoirs filled with a gas, which are sequentially connected by a narrow and a wide channels with equal length. At the reservoirs walls the constant temperature T_1 is kept. Along the walls of the narrow channel the temperature increases from T_1 to T_2 at the joint of the channels, and then decreases again to T_1 along the wall of the wide channel. The stationary state therefore corresponds to the two chambers at the same temperature but at different pressure.

2.4. Subjects

In the following, we shall deal with two main subjects.

The first subject is the study of the behaviour of the TPD exponent for a single gas. Specifically, we shall consider the case of a monatomic gas trapped between two infinite parallel plates. The collision model is the true linearized collision operator for hard-sphere molecules, and the boundary conditions are modelled with the Cercignani-Lampis model. We shall consider explicitly only the hydrodynamic and the slip regime, since analytical solutions in this limits are available, and we are interested in checking their reliability and maybe in extending their validity into the transition regime. We will

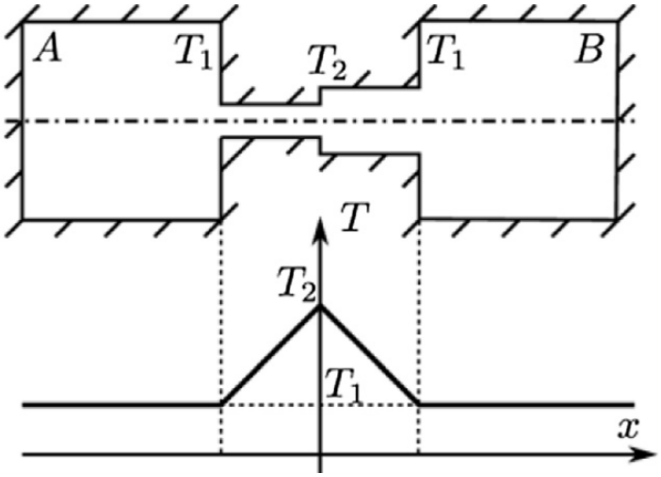

Figure 2.15.: Scheme of the Knudsen pump ([68]).

do this by comparing the results from the analytical expression with accurate numerical data, but also with some experimental data, that hopefully will be reproduced by our formulas.

The second subject is the study of the behaviour of the TPD exponent for a binary gaseous mixture. In particular, we will consider the case of a mixture of monatomic gases trapped between two infinite parallel plates. The collision model will be the McCormack model, and Maxwell boundary conditions are adopted. We will consider the whole regime of rarefaction, since we will rely on numerical computations, which hence hold in any regime of rarefaction.

3. TPD exponent for a single gas

In this chapter we analyse the first main topic of this thesis:
we deal with the computation of the TPD exponent for a single gas flowing between two infinite parallel plates. The Boltzmann equation based on the true linearized collision operator for hard-sphere molecules and the Cercignani-Lampis boundary conditions is used.

We shall study in detail the behaviour of our "reference" analytical expression of the TPD exponent with respect to the rarefaction parameter and the accommodation coefficients. The TPD exponent is here computed from its definition Eq. (2.70) via the formulas in [27, 28] (obtained with a variational method). Then we shall check its validity with a comparison with numerical and experimental data from the literature. From the analytical reference expression we shall also try to compute some simplified formulas, via a series expansion.
In both papers [27, 28], the purpose of the authors was to compute the coefficients for second-order slip boundary conditions to be associated with the LBE describing the problem at hand ([27] is dedicated to the study of the viscous slip coefficients, while in [28] the thermal coefficients are investigated). Therefore, to this aim, analytical expressions for the Poiseuille and thermal creep mass flow rates were obtained, which however do not hold in arbitrary regimes of rarefaction. The TPD exponent is hence simply computed, from Eq. (2.70), as the ratio between these quantities: the result is an analytical expression for γ, but valid only for certain rarefaction regimes.

3.1. Statement of the problem

Let us consider two infinite parallel plates separated by a distance d and a single species of monatomic gas flowing between them due to longitudinal gradients of pressure and temperature. In the (x, z) plane, the z axis coincides with the direction of the fluid motion, while the two walls are fixed at $x = \pm d/2$. If the pressure and temperature gradients are taken to be small, it can be assumed that the velocity distribution of the flow is nearly the same as that occurring in an equilibrium state. This means that the Boltzmann equation can be linearized about a Maxwellian f_0 by putting

$$f(x, z, \mathbf{c}) = f_0 \left[1 + kz + \left(c^2 - \frac{5}{2} \right) \tau z + h(x, \mathbf{c}) \right] , \tag{3.1}$$

where f is the distribution function for the molecular velocity $\mathbf{c}$ expressed in units of $\sqrt{2RT}$ (with R being the specific gas constant and T being the equilibrium temperature) and h is the small perturbation on the basic equilibrium state. The above-mentioned Maxwellian is given by

$$f_0(\mathbf{c}) = \frac{\rho_0}{\pi^{3/2}} \exp\left(-c^2\right) , \tag{3.2}$$

where ρ_0 is the equilibrium gas density and

$$k = \frac{1}{p}\frac{\partial p}{\partial z} \qquad \tau = \frac{1}{T}\frac{\partial T}{\partial z} \quad , \tag{3.3}$$

with p and T being the local gas pressure and temperature, respectively.
The steady LBE satisfied by the perturbation h is

$$c_x \frac{\partial h}{\partial x} + k c_z + \left(c^2 - \frac{5}{2}\right)\tau c_z = Lh\,, \tag{3.4}$$

where Lh is the linearized collision operator defined in Eq. (2.14).
In general, it is difficult to manage the Boltzmann operator L as such, and simplified kinetic models of the exact collision integral are widely used in practice for both analytical computations and numerical simulations (e.g., BGK, S-model, etc.). Anyway, in this chapter the Poiseuille and thermal-creep flows are analysed on the basis of the exact linearized collision operator for hard-sphere molecules in order to obtain a better approximation of real-gas behaviours.
The boundary conditions for Eq. (3.4) can be written as

$$h^+(-(d/2)\operatorname{sgn} c_x, \mathbf{c}) = \int_{c_x'<0} R_{CL}(-\mathbf{c} \to -\mathbf{c}')h^-(-(d/2)\operatorname{sgn} c_x, \mathbf{c}')d\mathbf{c}' \tag{3.5}$$

where $h^\pm$ are the restrictions of the function h, defined on the boundary, to positive (negative) values of c_x (that is, h^+ and h^- concern the re-emitted and the impinging molecules on the boundaries, respectively) and R_{CL} is the Cercignani-Lampis scattering kernel, given by Eq. (2.21).
The pressure and temperature gradients cause a gas flow and heat transfer in the z-direction. The bulk velocity $v_z(x)$ and the heat flux $q_z(x)$ are defined as

$$v_z(x) = \pi^{-3/2}\int_{-\infty}^{+\infty}\int_{-\infty}^{+\infty}\int_{-\infty}^{+\infty} e^{-c^2} c_z h(x, \mathbf{c})d\mathbf{c}\,, \tag{3.6}$$

$$q_z(x) = \pi^{-3/2}\int_{-\infty}^{+\infty}\int_{-\infty}^{+\infty}\int_{-\infty}^{+\infty} e^{-c^2} c_z \left(c^2 - \frac{5}{2}\right) h(x, \mathbf{c})d\mathbf{c}\,. \tag{3.7}$$

Hence, the mass $\dot{M}$ and heat flow rate $\dot{Q}$ (per unit time through unit thickness) are given by

$$\dot{M} = \rho\int_{-d/2}^{d/2} v_z(x)dx\,, \tag{3.8}$$

$$\dot{Q} = \int_{-d/2}^{d/2} q_z(x)dx\,, \tag{3.9}$$

which, within the framework of a linearized analysis, can be expressed by the sum of the Poiseuille and thermal creep contributions as

$$\dot{M} = d^2 p\,[-G_P k + G_T \tau] \tag{3.10}$$

$$\dot{Q} = \frac{d^2}{2} p\,[Q_P k - Q_T \tau] \tag{3.11}$$

where G_P, G_T, Q_P, and Q_T are dimensionless coefficients (defined to be always positive) that represent the Poiseuille coefficient, the thermal creep coefficient, the mechanocaloric coefficient and the reduced heat flux, respectively.
In [53, 69, 70], it was proven that the cross coefficients G_T and Q_P obey the Onsager relation

$$G_T = Q_P\,. \tag{3.12}$$

3.2. Reference value of the TPD exponent

To apply the variational formulation, a suitable functional J is introduced, which attains its minimum when the test function solves Eq. (3.4); the stationary value of J has a direct connection with the quantities of physical interest for the problem at hand. Since the purpose of the authors was to provide an analytical expression for the slip coefficients, it has been sufficient to consider asymptotic results (near-continuum) for mass flow rates. Therefore, J was evaluated on a simplified test function, with some adjustable constants to be varied in order to obtain the best value of the functional. The results of all the computations are ([27])

$$G_P = \frac{\delta}{\sigma_0^P} + \sigma_1^P + \frac{\sigma_2^P}{\delta} + \dots \tag{3.13}$$

and ([28])

$$G_T = \frac{\sigma_1^T}{\delta} + \frac{\sigma_2^T}{\delta^2} + \dots , \tag{3.14}$$

both valid, *a priori*, only for $\delta \gg 1$.
From a comparison between Eqs. (3.13) and (3.14) and the pressure- and thermal-driven mass flow rates obtained by using the Navier-Stokes equations with second-order slip boundary conditions, it can be found that the σ coefficients are related to the slip coefficients defined in Section 2.3.1.1 through the formulas

$$A_1^P = \frac{\sigma_0^P \sigma_1^P}{3\sqrt{\pi}} \tag{3.15}$$

$$A_2^P = \frac{\sigma_0^P \sigma_2^P}{3\pi} \tag{3.16}$$

and

$$A_1^T = \sigma_1^T \tag{3.17}$$

$$A_2^T = \sigma_2^T \tag{3.18}$$

From a comparison with results obtained by a direct numerical solution of the LBE, it has been assessed that the validity of Eqs. (3.13) and (3.14) extends up to $\delta \simeq 3$, hence beyond the classical slip regime.

Therefore, from Eq. (2.70), the resulting expression for γ is

$$\gamma = \frac{\dfrac{\sigma_1^T}{\delta} + \dfrac{\sigma_2^T}{\delta^2}}{\dfrac{\delta}{\sigma_0^P} + \sigma_1^P + \dfrac{\sigma_2^P}{\delta}} . \tag{3.19}$$

In this section, we analyse what we shall call the "reference value" of the TPD exponent γ, that is, we study the analytical behaviour of Eq. (3.19) without any substantial simplification:

$$\gamma = \frac{\sigma_1^T \delta + \sigma_2^T}{\dfrac{1}{\sigma_0^P}\delta^3 + \sigma_1^P \delta^2 + \sigma_2^P \delta} = \frac{\sigma_1^T \delta + \sigma_2^T}{\delta\left(\dfrac{1}{\sigma_0^P}\delta^2 + \sigma_1^P \delta + \sigma_2^P\right)} = \frac{\sigma_1^T + \dfrac{\sigma_2^T}{\delta}}{\dfrac{1}{\sigma_0^P}\delta^2 + \sigma_1^P \delta + \sigma_2^P} .$$

The coefficients are (see [27, 28]):

$$\sigma_1^T = \left[64\hat{J}_4\left(\frac{2\hat{J}_1}{\pi^{3/2}}+1\right)\right]^{-1}\left[16\left(5\hat{J}_1-10\hat{J}_3+2\hat{J}_4\right)+10\pi^{3/2}\left(\alpha_t+\alpha_n-\alpha_t\alpha_n+4\right)\right] \tag{3.20}$$

$$\sigma_2^T = \left[2\sqrt{\pi}A_T\right]^{-1}\left[\frac{B_T C_T}{A_T}-E_T\right] \tag{3.21}$$

$$A_T = \frac{32\hat{J}_4}{3\sqrt{\pi}}\left[\frac{2\hat{J}_1}{\pi^{3/2}}+1\right]\alpha_t \tag{3.22}$$

$$B_T = -\frac{128}{\pi}\hat{J}_4\alpha_t(1-\alpha_t)\left[F_0\alpha_n+F_1(1-\alpha_n)\right]-8\hat{J}_4\left[\frac{4}{\pi}+\alpha_t\right]\alpha_t \tag{3.23}$$

$$+\frac{16}{3}\sqrt{\pi}\left[\frac{2\hat{J}_1}{\pi^{3/2}}+1\right]\left[\alpha_n+7\alpha_t+2{\alpha_t}^3-6{\alpha_t}^2-\alpha_t\alpha_n\right]\alpha_t \tag{3.24}$$

$$C_T = -\frac{16}{3}\left[5\hat{J}_1-10\hat{J}_3+2\hat{J}_4\right]\alpha_t-\frac{10}{3}\pi^{3/2}\left[\alpha_t+\alpha_n-\alpha_t\alpha_n+4\right]\alpha_t \tag{3.25}$$

$$E_T = -32\sqrt{\pi}\left[5\hat{J}_3-\hat{J}_4\right]\alpha_t+160\pi\alpha_t(1-\alpha_t)\left[F_0\alpha_n+F_1(1-\alpha_n)\right]$$
$$+10\pi^2\alpha_t\left[2\alpha_t+\alpha_n-\alpha_t\alpha_n\right]-\frac{32}{3}\pi\alpha_t\left[\alpha_t-2\alpha_n-3{\alpha_t}^2+{\alpha_t}^3+2\alpha_t\alpha_n-\frac{15}{4}\right] \tag{3.26}$$

$$\sigma_0^P = \left(4\sqrt{\pi}\right)^{-1}\left[\frac{96}{\pi}\hat{J}_1+48\sqrt{\pi}\right]\simeq 5.8883 \tag{3.27}$$

$$\sigma_1^P = \left(4\sqrt{\pi}A_P\alpha_t\right)^{-1}\left[D_P-\frac{16}{9}\pi C_P\alpha_t\right] \tag{3.28}$$

$$\sigma_2^P = \left(4\sqrt{\pi}A_P\alpha_t\right)^{-1}\left[E_P+\frac{16}{9}\pi{C_P}^2\alpha_t-\frac{16}{9}\pi B_P\alpha_t-C_P D_P\right] \tag{3.29}$$

$$A_P = \frac{32}{3\pi}\hat{J}_1+\frac{16}{3}\sqrt{\pi}\simeq 4.6385 \tag{3.30}$$

$$B_P = {A_P}^{-1}\left[\frac{128}{\pi}\hat{J}_2-16\sqrt{\pi}\alpha_t-16\sqrt{\pi}\alpha_n+16\sqrt{\pi}\alpha_t\alpha_n\right] \tag{3.31}$$

$$C_P = {A_P}^{-1}\left[-16-4\pi\alpha_t-64F_0\alpha_n(1-\alpha_t)-64F_1(1-\alpha_t)(1-\alpha_n)\right] \tag{3.32}$$

$$D_P = \frac{128}{3}\hat{J}_1-\frac{32}{3}\pi^{3/2}\alpha_t+\frac{64}{3}\pi^{3/2} \tag{3.33}$$

$$E_P = -64\pi+\frac{64}{3}\pi\alpha_t-256\pi F_0\alpha_n(1-\alpha_t)-256\pi F_1(1-\alpha_t)(1-\alpha_n) \tag{3.34}$$

with the numerical parameters

$$\hat{J}_1 = -1.4180 \qquad \hat{J}_2 = 1.8909 \tag{3.35}$$

$$\hat{J}_3 = 0.9449 \qquad \hat{J}_4 = 4.7252 \tag{3.36}$$

$$F_0 = 0.196079 \qquad F_1 = 0.247679 \tag{3.37}$$

We are interested in studying the dependence of γ on the rarefaction parameter δ and on the accommodation coefficients α_t and α_n.

3.2.1. Preliminary considerations

For what concerns the behaviour with respect to δ, we have that:

1. $\delta = \dfrac{-\sigma_1^P \pm \sqrt{{\sigma_1^P}^2 - 4\sigma_2^P/\sigma_0^P}}{2/\sigma_0^P} \quad \Rightarrow \quad \gamma \to \infty$;
2. $\delta \to 0 \quad \Rightarrow \quad \gamma \to \infty$;
3. $\delta = -\sigma_2^T/\sigma_1^T \quad \Rightarrow \quad \gamma = 0$;
4. $\delta \to \infty \quad \Rightarrow \quad \gamma \to 0$ and $\propto 1/\delta^2$.

Since the expressions of all the coefficients reported above are obtained in the case $\delta \gg 1$, we can neglect case 1 (in which, via numerical check, we have $\delta < 0$, which does not make physical sense) and 2 ($\delta \to 0$). Moreover, as observed in Section 2.3.2.2, γ should be monotonically decreasing as δ increases, therefore the minimum δ for which the model is correct will be for sure strictly bigger than the one reported in case 3. Finally, the trend described in case 4, that is, the vanishing and the particular asymptotic behaviour of the TPD exponent as the rarefaction parameter is in viscous flow regime, is exactly what we expected, according to Section 2.3.2.2 and [56].

For what concerns the accommodation coefficients, we observe that the above coefficients contain denominators proportional to α_t: precisely, we find divergent denominators in σ_2^T, σ_1^P and σ_2^P when $\alpha_t = 0$. Therefore, we look for some simplifications.
We rewrite the coefficients in order to highlight their dependence on the accommodation parameters:

$$A_T = \frac{32\hat{J}_4}{3\sqrt{\pi}}\left[\frac{2\hat{J}_1}{\pi^{3/2}} + 1\right]\alpha_t = A'_T\alpha_t \quad A'_T = \frac{32\hat{J}_4}{3\sqrt{\pi}}\left[\frac{2\hat{J}_1}{\pi^{3/2}} + 1\right] \simeq 13.9535 \tag{3.38}$$

$$\begin{aligned} B_T = &\left[-\frac{32}{\pi}\hat{J}_4(4F_1 - 1)\right]\alpha_t + \left[\frac{128}{\pi}\hat{J}_4F_1 - 8\hat{J}_4 + \frac{112}{3}\sqrt{\pi}\left(\frac{2\hat{J}_1}{\pi^{3/2}} + 1\right)\right]{\alpha_t}^2 \\ &+ \left[-\frac{128}{\pi}\hat{J}_4(F_0 - F_1) + \frac{16}{3}\sqrt{\pi}\left(\frac{2\hat{J}_1}{\pi^{3/2}} + 1\right)\right]\alpha_t\alpha_n \\ &+ \left[\frac{128}{\pi}\hat{J}_4(F_0 - F_1) - \frac{16}{3}\sqrt{\pi}\left(\frac{2\hat{J}_1}{\pi^{3/2}} + 1\right)\right]{\alpha_t}^2\alpha_n \\ &+ \left[-32\sqrt{\pi}\left(\frac{2\hat{J}_1}{\pi^{3/2}} + 1\right)\right]{\alpha_t}^3 + \left[\frac{32}{3}\sqrt{\pi}\left(\frac{2\hat{J}_1}{\pi^{3/2}} + 1\right)\right]{\alpha_t}^4 \\ = &\, B'_T\alpha_t \end{aligned} \tag{3.39}$$

$$\begin{aligned} B'_T = &\left[-\frac{32}{\pi}\hat{J}_4(4F_1 - 1)\right] + \left[\frac{128}{\pi}\hat{J}_4F_1 - 8\hat{J}_4 + \frac{112}{3}\sqrt{\pi}\left(\frac{2\hat{J}_1}{\pi^{3/2}} + 1\right)\right]\alpha_t \\ &+ \left[-\frac{128}{\pi}\hat{J}_4(F_0 - F_1) + \frac{16}{3}\sqrt{\pi}\left(\frac{2\hat{J}_1}{\pi^{3/2}} + 1\right)\right]\alpha_n \end{aligned} \tag{3.40}$$

$$+\left[\frac{128}{\pi}\hat{J}_4(F_0-F_1)-\frac{16}{3}\sqrt{\pi}\left(\frac{2\hat{J}_1}{\pi^{3/2}}+1\right)\right]\alpha_t\alpha_n$$
$$+\left[-32\sqrt{\pi}\left(\frac{2\hat{J}_1}{\pi^{3/2}}+1\right)\right]{\alpha_t}^2+\left[\frac{32}{3}\sqrt{\pi}\left(\frac{2\hat{J}_1}{\pi^{3/2}}+1\right)\right]{\alpha_t}^3$$

$$\begin{aligned}C_T&=\left[-\frac{16}{3}\left(5\hat{J}_1-10\hat{J}_3+2\hat{J}_4\right)-\frac{40}{3}\pi^{3/2}\right]\alpha_t\\&\quad+\left[-\frac{10}{3}\pi^{3/2}\right]{\alpha_t}^2+\left[-\frac{10}{3}\pi^{3/2}\right]\alpha_t\alpha_n+\left[\frac{10}{3}\pi^{3/2}\right]{\alpha_t}^2\alpha_n\\&=C'_T\alpha_t\end{aligned}\tag{3.41}$$

$$\begin{aligned}C'_T&=\left[-\frac{16}{3}\left(5\hat{J}_1-10\hat{J}_3+2\hat{J}_4\right)-\frac{40}{3}\pi^{3/2}\right]\\&\quad+\left[-\frac{10}{3}\pi^{3/2}\right]\alpha_t+\left[-\frac{10}{3}\pi^{3/2}\right]\alpha_n+\left[\frac{10}{3}\pi^{3/2}\right]\alpha_t\alpha_n\end{aligned}\tag{3.42}$$

$$\begin{aligned}E_T&=\left[-32\sqrt{\pi}(5\hat{J}_3-\hat{J}_4)+40\pi(4F_1+1)\right]\alpha_t+\left[160\pi(F_0-F_1)+\frac{64}{3}\pi\right]\alpha_t\alpha_n\\&\quad+\left[-160\pi(F_0-F_1)-10\pi^2-\frac{64}{3}\pi\right]{\alpha_t}^2\alpha_n\\&\quad+\left[-160\pi F_1+20\pi^2-\frac{32}{3}\pi\right]{\alpha_t}^2+[32\pi]\,{\alpha_t}^3+\left[-\frac{32}{3}\pi\right]{\alpha_t}^4\\&=E'_T\alpha_t\end{aligned}\tag{3.43}$$

$$\begin{aligned}E'_T&=\left[-32\sqrt{\pi}(5\hat{J}_3-\hat{J}_4)+40\pi(4F_1+1)\right]+\left[160\pi(F_0-F_1)+\frac{64}{3}\pi\right]\alpha_n\\&\quad+\left[-160\pi(F_0-F_1)-10\pi^2-\frac{64}{3}\pi\right]\alpha_t\alpha_n\\&\quad+\left[-160\pi F_1+20\pi^2-\frac{32}{3}\pi\right]\alpha_t+[32\pi]\,{\alpha_t}^2+\left[-\frac{32}{3}\pi\right]{\alpha_t}^3\end{aligned}\tag{3.44}$$

$$A_P=\frac{16}{3}\left(\frac{2}{\pi}\hat{J}_1+\sqrt{\pi}\right)\quad B_P=\frac{16}{A_P}\left[\frac{8}{\pi}\hat{J}_2-\sqrt{\pi}\alpha_t-\sqrt{\pi}\alpha_n+\sqrt{\pi}\alpha_t\alpha_n\right]\tag{3.45}$$

$$C_P=-16\frac{1+4F_1}{A_P}+\left[4\frac{16F_1-\pi}{A_P}\right]\alpha_t+\left[\frac{64(F_1-F_0)}{A_P}\right]\alpha_n+\left[-\frac{64(F_1-F_0)}{A_P}\right]\alpha_t\alpha_n\tag{3.46}$$

$$D_P=\frac{64}{3}\left(2\hat{J}_1+\pi^{3/2}\right)+\left[-\frac{32}{3}\pi^{3/2}\right]\alpha_t\tag{3.47}$$

$$E_P=[-64\pi-256\pi F_1]+\left[\frac{64}{3}\pi+256\pi F_1\right]\alpha_t+[256\pi(F_1-F_0)]\,\alpha_n+[256\pi(F_0-F_1)]\,\alpha_t\alpha_n\tag{3.48}$$

Therefore:

$$\sigma_2^T=\frac{1}{2\sqrt{\pi}}\left[\frac{B_TC_T}{{A_T}^2}-\frac{E_T}{A_T}\right]=\frac{1}{2\sqrt{\pi}}\left[\frac{B'_TC'_T{\alpha_t}^2}{{A'_T}^2{\alpha_t}^2}-\frac{E'_T\alpha_t}{A'_T\alpha_t}\right]=\frac{1}{2\sqrt{\pi}}\left[\frac{B'_TC'_T}{{A'_T}^2}-\frac{E'_T}{A'_T}\right],\tag{3.49}$$

hence, σ_2^T is non-singular for every choice of the accommodation coefficients;

$$\begin{aligned} D_P - \frac{16}{9}\pi C_P \alpha_t &= \frac{64}{3}\left(2\hat{J}_1 + \pi^{3/2}\right) + \left[-\frac{32}{3}\pi^{3/2}\right]\alpha_t - \frac{16}{9}\pi\left\{-16\frac{1+4F_1}{A_P} + \left[4\frac{16F_1-\pi}{A_P}\right]\alpha_t \right. \\ &\quad \left. + \left[\frac{64(F_1-F_0)}{A_P}\right]\alpha_n + \left[-\frac{64(F_1-F_0)}{A_P}\right]\alpha_t\alpha_n\right\}\alpha_t \\ &= \left[\frac{64}{3}\left(2\hat{J}_1 + \pi^{3/2}\right)\right] + \left[-\frac{32}{3}\pi^{3/2} + \frac{256}{9}\pi\frac{1+4F_1}{A_P}\right]\alpha_t \\ &\quad + \left[-\frac{64}{9}\pi\frac{16F_1-\pi}{A_P}\right]{\alpha_t}^2 + \left[-\frac{1024}{9}\pi\frac{F_1-F_0}{A_P}\right]\alpha_t\alpha_n + \left[\frac{1024}{9}\pi\frac{F_1-F_0}{A_P}\right]{\alpha_t}^2\alpha_n \\ &\Rightarrow \quad D_P - \frac{16}{9}\pi C_P\alpha_t \neq 0 \text{ if } \alpha_t = 0\,, \end{aligned}$$

therefore σ_1^P is singular for $\alpha_t = 0$;

finally, after some elementary manipulations:

$$\begin{aligned} E_P + \frac{16}{9}\pi {C_P}^2\alpha_t - \frac{16}{9}\pi B_P\alpha_t - C_P D_P &= E_P - \left(D_P - \frac{16}{9}\pi C_P\alpha_t\right)C_P - \frac{16}{9}\pi B_P\alpha_t \\ &= {\sigma_2^P}'\alpha_t \end{aligned} \tag{3.50}$$

with

$$\begin{aligned} {\sigma_2^P}' &= \left[\frac{64}{3}\pi + 16\pi^2 - 32\pi^{5/2}\frac{1+4F_1}{2\hat{J}_1+\pi^{3/2}} + 16\pi^3\left(\frac{1+4F_1}{2\hat{J}_1+\pi^{3/2}}\right)^2 - \frac{128}{3}\pi\hat{J}_2\frac{1}{2\hat{J}_1+\pi^{3/2}}\right] \\ &\quad + \left[8\pi^{5/2}\frac{16F_1-\pi}{2\hat{J}_1+\pi^{3/2}} - 8\pi^3\frac{(1+4F_1)(16F_1-\pi)}{2\hat{J}_1+\pi^{3/2}}\right]\alpha_t + \left[\pi^3\left(\frac{16F_1-\pi}{2\hat{J}_1+\pi^{3/2}}\right)^2\right]{\alpha_t}^2 \\ &\quad + \left[128\pi^{5/2}\frac{F_1-F_0}{2\hat{J}_1+\pi^{3/2}} - 128\pi^3\frac{(F_1-F_0)(1+4F_1)}{(2\hat{J}_1+\pi^{3/2})^2} + \frac{16}{3}\frac{\pi^{5/2}}{2\hat{J}_1+\pi^{3/2}}\right]\alpha_n \\ &\quad + \left[128\pi^{5/2}\frac{F_1-F_0}{2\hat{J}_1+\pi^{3/2}} + 128\pi^3\frac{(1+4F_1)(F_1-F_0)}{(2\hat{J}_1+\pi^{3/2})^2} + 32\pi^3\frac{(16F_1-\pi)(F_1-F_0)}{(2\hat{J}_1+\pi^{3/2})^2}\right. \\ &\quad \left. - \frac{16}{3}\pi^{5/2}\frac{1}{2\hat{J}_1+\pi^{3/2}}\right]\alpha_t\alpha_n \\ &\quad + \left[-32\pi^3\frac{(16F_1-\pi)(F_1-F_0)}{(2\hat{J}_1+\pi^{3/2})^2}\right]{\alpha_t}^2\alpha_n + \left[256\pi^3\left(\frac{F_1-F_0}{2\hat{J}_1+\pi^{3/2}}\right)^2\right]{\alpha_n}^2 \\ &\quad + \left[-256\pi^3\left(\frac{F_1-F_0}{2\hat{J}_1+\pi^{3/2}}\right)^2\right]\alpha_t{\alpha_n}^2 + \left[256\pi^3\left(\frac{F_1-F_0}{2\hat{J}_1+\pi^{3/2}}\right)^2\right]{\alpha_t}^2{\alpha_n}^2\,. \end{aligned} \tag{3.51}$$

In the numerator of σ_2^P, the coefficients of the terms constant with respect to α_t are identically zero, so α_t at the denominator simplifies and therefore σ_2^P is non-singular

for every choice of the accommodation coefficients.
To sum up: the only divergent coefficient for some choice of the accommodation coefficients is σ_1^P, and precisely $\gamma \to 0$ for $\alpha_t \to 0$.

The final expressions for the σ coefficients are:

$$\sigma_1^T = \left[64\hat{J}_4\left(\frac{2\hat{J}_1}{\pi^{3/2}}+1\right)\right]^{-1}\left[16\left(5\hat{J}_1-10\hat{J}_3+2\hat{J}_4\right)+10\pi^{3/2}\left(\alpha_t+\alpha_n-\alpha_t\alpha_n+4\right)\right] \tag{3.52}$$

$$\sigma_2^T = \frac{1}{2\sqrt{\pi}}\left[\frac{B_T'C_T'}{{A_T'}^2}-\frac{E_T'}{A_T'}\right] \tag{3.53}$$

$$\sigma_0^P = \left(4\sqrt{\pi}\right)^{-1}\left[\frac{96}{\pi}\hat{J}_1+48\sqrt{\pi}\right] \tag{3.54}$$

$$\sigma_1^P = \left(4\sqrt{\pi}A_P\alpha_t\right)^{-1}\left[D_P-\frac{16}{9}\pi C_P\alpha_t\right] \tag{3.55}$$

$$\sigma_2^P = \frac{\sigma_2^{P\prime}}{4\sqrt{\pi}A_P} \tag{3.56}$$

3.2.2. Analytical behaviour of the reference expression

3.2.2.1. γ for fixed δ and varying α_t and α_n

Here, we consider γ as a two-dimensional function of the accommodation coefficients only, considering δ as a parameter, and we study the 3-D plot of $\gamma = \gamma(\alpha_t, \alpha_n)$ as δ varies.
In general, we observe the foreseen trend $\gamma \to 0$ as $\delta \to +\infty$, but this behaviour is uniform (that is, true for every choice of α_t and α_n) only for δ large enough: for $\delta < 5$ there is a region ($\alpha_t \simeq 2$, $\alpha_n \simeq 0$, and the bigger the δ, the smaller the region) where γ locally increases as δ increases (Fig. 3.1), while for $\delta > 5$ we have that, for every α_t, α_n fixed, γ is monotonically decreasing as δ increases (Fig. 3.2). This could be an indication that this model of the boundary conditions in the TPD effect may be not suitable if the gas is too rarefied and a large α_t and a small α_n are needed.
Moreover, we observe that for $\delta < 3$ there is a region ($\alpha_t \simeq 2$, $\alpha_n \simeq 0$) where $\gamma < 0$ (Fig. 3.3), but we already knew, and we find a confirm here, that in this regime of (high) rarefaction the previous expressions of the mass flow rates are not valid, especially for these particular values of the accommodation coefficients.
Finally, we observe, here only in a qualitative sense and more quantitatively in the following, that for $\delta \geq 5$ γ is visibly more sensible on the choice of α_t rather than of α_n.

3.2.2.2. γ for fixed α_t and α_n and varying δ

Here, we consider γ as a function of the rarefaction parameter only, and we study the graph of $\gamma = \gamma(\delta)$ as α_t and α_n vary.
The qualitative trend is the same for every choice of the parameters: γ has a maximum for relatively small δ, and goes to 0 as $\delta \to \infty$.
Moreover, for fixed α_n, as α_t increases (see Fig. 3.4):

- the maximum is reached for bigger δ;

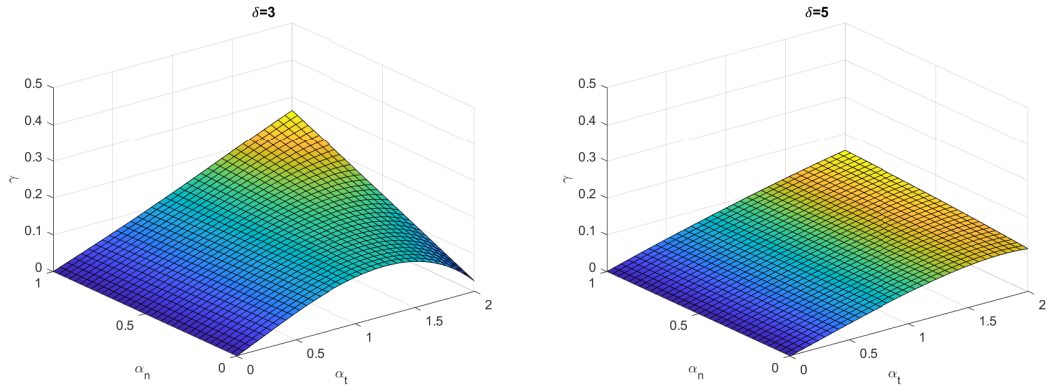

(a) $\delta = 3$. (b) $\delta = 5$.

Figure 3.1.: $\gamma = \gamma(\alpha_t, \alpha_n)$ for different fixed δ: as δ increases, γ is locally increasing for $\alpha_t \simeq 2$ $\alpha_n \simeq 0$.

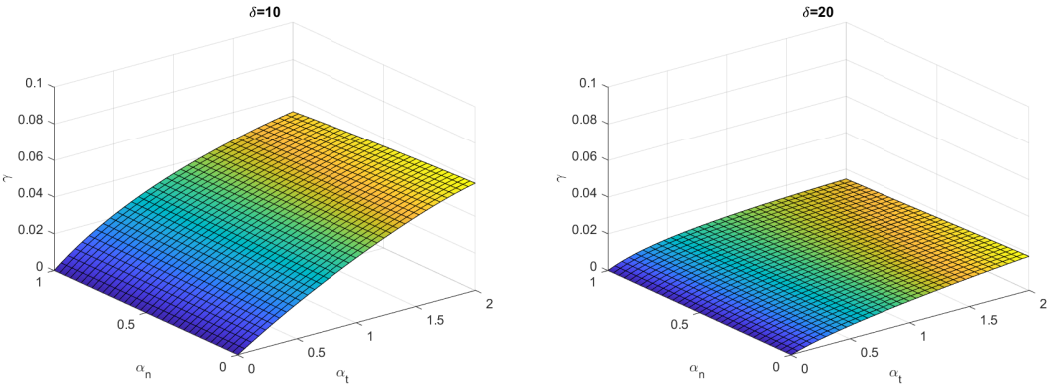

(a) $\delta = 10$. (b) $\delta = 20$.

Figure 3.2.: $\gamma = \gamma(\alpha_t, \alpha_n)$ for different fixed δ: if δ is large enough, γ is uniformly decreasing as δ increases.

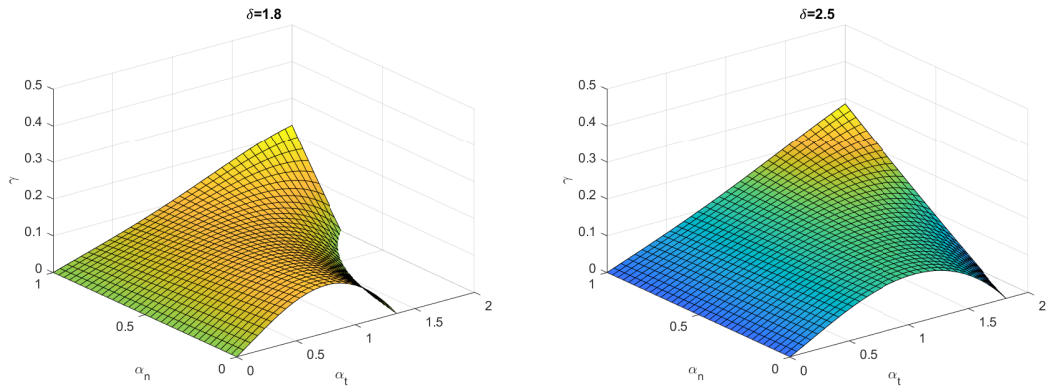

(a) $\delta = 1.8$. (b) $\delta = 2.5$.

Figure 3.3.: $\gamma = \gamma(\alpha_t, \alpha_n)$ for different fixed δ: if δ is too small, γ is locally negative.

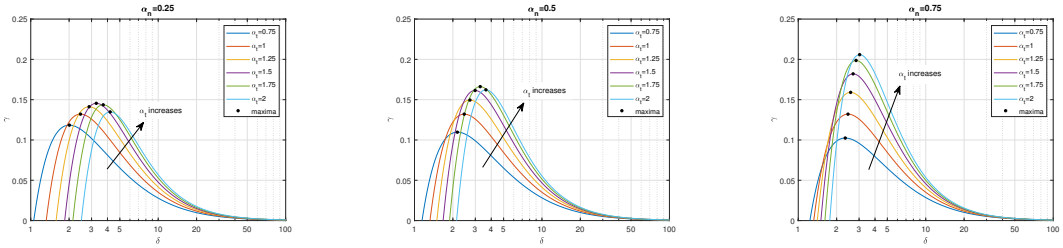

(a) $\alpha_n = 0.25$. (b) $\alpha_n = 0.5$. (c) $\alpha_n = 0.75$.

Figure 3.4.: $\gamma = \gamma(\delta)$ for α_n fixed and different increasing α_t: the point of maximum moves towards bigger δ, and the maximum first increases and then decreases.

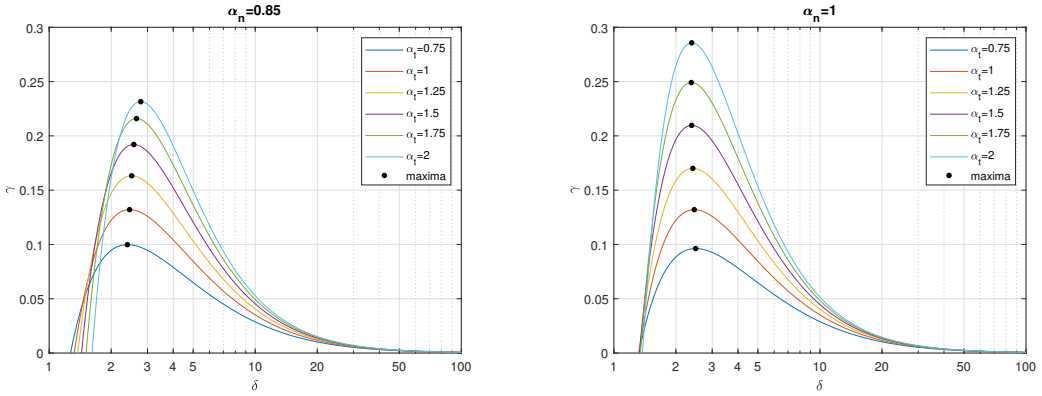

(a) $\alpha_n = 0.85$. (b) $\alpha_n = 1$.

Figure 3.5.: $\gamma = \gamma(\delta)$ for large α_n fixed and different increasing α_t: the maxima tend to align on a vertical line.

- the value of the maximum increases (and after a certain α_t also decreases if $\alpha_n < 0.7$);
- as α_n gets closer to 1, the maxima tend to lie on a vertical line (Fig. 3.5).

Viceversa, for fixed α_t, as α_n increases (see Fig. 3.6):

- the maximum is reached for bigger δ if $\alpha_t < 1$, and for smaller δ if $\alpha_t > 1$;
- the value of the maximum decreases if $\alpha_t < 1$, and increases if $\alpha_t > 1$;
- for $\alpha_t = 1$, γ is exactly the same for every α_n.

Even just looking at the graphs, we can make some qualitative observations:

- with fixed α_n, γ varies sensibly as α_t varies, especially for about $\delta < 10$;
- viceversa, for α_t fixed, the dependence of γ on α_n is rather weak, especially for $\delta > 4 \div 5$.

These remarks qualitatively agree with what was observed at the end of the previous section. The consequence is that, in order to describe correctly the phenomenon, we expect that it is more important to tune precisely α_t rather than α_n, especially near the transition regime.

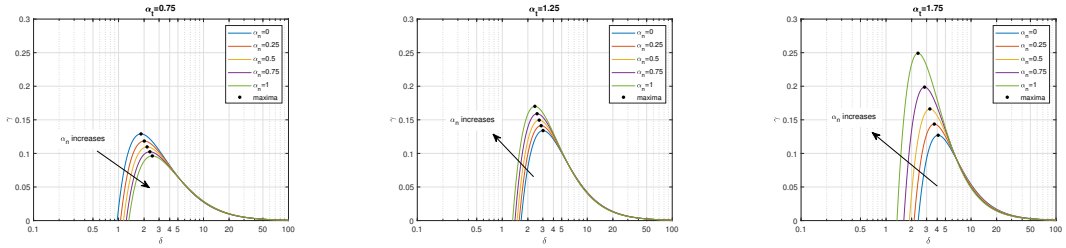

(a) $\alpha_t = 0.75$. (b) $\alpha_t = 1.25$. (c) $\alpha_t = 1.75$.

Figure 3.6.: $\gamma = \gamma(\delta)$ for α_t fixed and different increasing α_n: the point of maximum moves towards bigger or smaller δ and the maximum decreases or increases depending on the value of α_t.

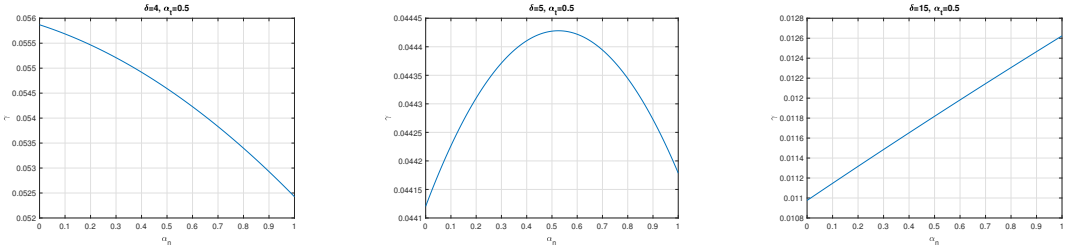

(a) $\delta = 4$, $\alpha_t = 0.5$. (b) $\delta = 5$, $\alpha_t = 0.5$. (c) $\delta = 15$, $\alpha_t = 0.5$.

Figure 3.7.: $\gamma = \gamma(\alpha_n)$ for δ and $\alpha_t < 1$ fixed.

Moreover, the fact that γ must be strictly decreasing with respect to δ forces a lower bound for the domain of validity of the model with respect to the rarefaction regime: the rarefaction parameter must be greater than the point of maximum of the curve. In particular, even if it was assessed, through numerical simulations, that Eqs. (3.13) and (3.14) hold up to $\delta \simeq 3$, this model is actually unable to describe correctly the TPD phenomenon if we are dealing with large α_t and small α_n (see Figs. 3.4 and 3.6) and $\delta < 5$, in agreement with previous observations.

3.2.2.3. γ for fixed δ and α_t and varying α_n

Here, we consider γ as a function of α_n, considering δ and α_t as parameters, and we study the graph of $\gamma = \gamma(\alpha_n)$ as δ and α_t vary.

$\alpha_t < 1$ (Fig. 3.7): γ is strictly decreasing for δ small, has a maximum for δ intermediate, strictly increasing for bigger δ, is almost linear for δ big enough.

$\alpha_t = 1$: for every δ, γ has a constant value as α_n varies, as already observed. This is a strong indication that, if $\alpha_t = 1$, then the TPD effect is not influenced by the part of the mathematical model (and maybe of the physical problem) described by α_n.

$\alpha_t > 1$ (Fig. 3.8): γ is strictly increasing for δ small, has a maximum for δ intermediate, strictly decreasing for bigger δ, is almost linear for δ big enough.

It may be interesting to study the *percent variation* of $\gamma = \gamma(\alpha_n)$ through the domain of α_n for fixed δ and α_t, defined as

$$\Delta_{\%} = \frac{\max\limits_{\alpha_n} \gamma - \min\limits_{\alpha_n} \gamma}{\min\limits_{\alpha_n} \gamma} \,. \tag{3.57}$$

For different values of δ and α_t, $\Delta_{\%}$ takes in general different values, so we can actually

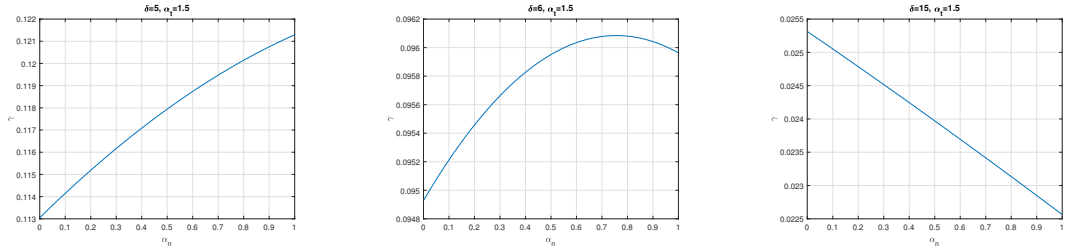

(a) $\delta = 5$, $\alpha_t = 1.5$. (b) $\delta = 6$, $\alpha_t = 1.5$. (c) $\delta = 15$, $\alpha_t = 1.5$.

Figure 3.8.: $\gamma = \gamma(\alpha_n)$ for δ and $\alpha_t > 1$ fixed.

write $\Delta_{\%} = \Delta_{\%}(\delta, \alpha_t)$. Let us have a look at the dependence of this quantity on δ for different values of α_t.

Treating α_t as a parameter and δ as the only independent variable (but always with $\delta > 3$), we can see (Fig. 3.9) that the behaviour of $\Delta_{\%}$ is qualitative similar for every α_t: it rapidly decreases for small δ, has a deep minimum for a certain intermediate δ, and tends to a constant value as δ increases.
For what concerns the quantitative values, we can see that the closer α_t is to 1 the smaller is the percent variation of γ (i.e., the lesser γ changes by changing α_n), that is, the weaker is the dependence of γ on α_n. As a limit case, for $\alpha_t = 1$, $\Delta_{\%}$ is identically zero, no matter what δ is. For example, for $0.8 < \alpha_t < 1.2$ the percent variation of γ as α_n goes from 0 to 1 is less than 10%, and for $0.6 < \alpha_t < 1.4$ is less than 15% for practically every δ. We actually have a pretty large variation of γ for $\alpha_t = 1.4$ in the interval $3 < \delta < 4$, and it becomes even worse with bigger α_t. This seems to indicate a very sensible γ with respect to α_n in this interval of δ, but indeed we already know that this region of rarefaction regimes is a "grey area" of the model if α_t is big: as a consequence, it is unlikely that this strong dependence of γ on α_n is realistic.

These merely numerical considerations have practical consequences: for example, for $\alpha_t \simeq 1$, and indifferently on the rarefaction regime, it may be difficult, but probably also useless, to tune experimentally α_n with high precision, since the percent variation of γ might be similar to the relative sensitivity of the instruments. The same considerations may be done even for α_t not too close to 1, but coupled with a particular rarefaction regime, well described by the point of minimum of $\Delta_{\%}$ for that specific α_t. Another consideration is related to $\Delta_{\%}$ at large δ: the fact that it tends to a constant value at large δ means that after a certain point the sensitivity of γ with respect to α_n is not influenced by the regime of rarefaction any more. Therefore, the importance of tuning α_n accurately in order to have a correct model is always the same, for every δ large enough. Actually, concerning this last remark, it is worth noting that the intensity of the phenomenon of thermal creep, measurable for example by the TPD exponent itself, fades as δ increases: once a certain regime of (low) rarefaction is reached, it may be literally impossible, regardless the sensitivity of γ on α_n, even to detect the phenomenon, and all this work loses its point.

3.2.2.4. γ for fixed δ and α_n and varying α_t

Here, we consider γ as a function of α_t, considering δ and α_n as parameters, and we study the graph of $\gamma = \gamma(\alpha_t)$ as δ and α_n vary.

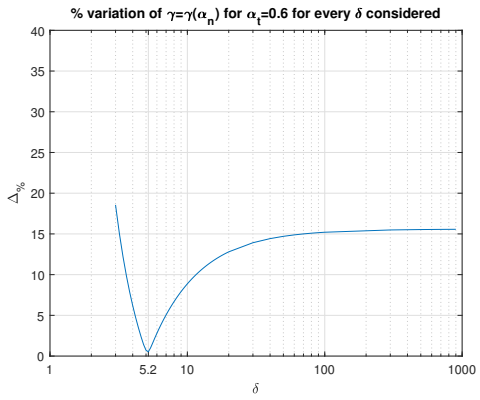

(a) $\alpha_t = 0.6$.

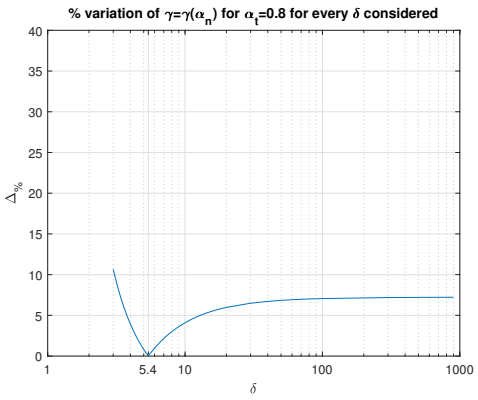

(b) $\alpha_t = 0.8$.

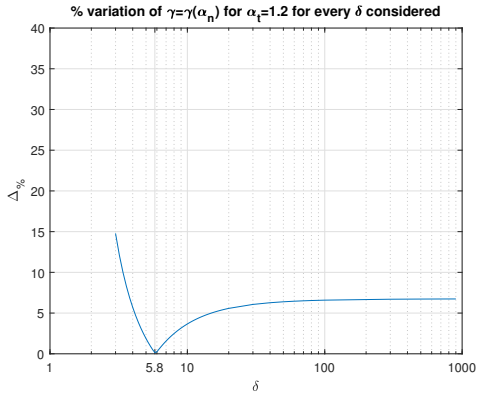

(c) $\alpha_t = 1.2$.

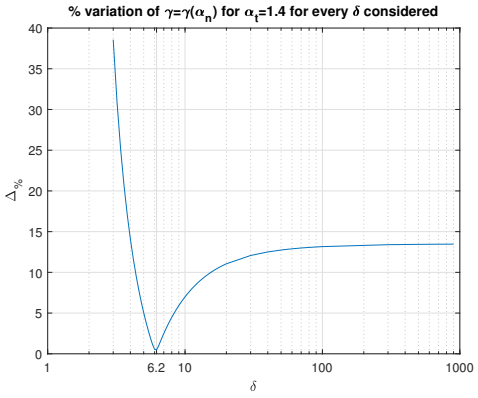

(d) $\alpha_t = 1.4$.

Figure 3.9.: $\Delta_{\%}$ for different α_t in the entire range of δ.

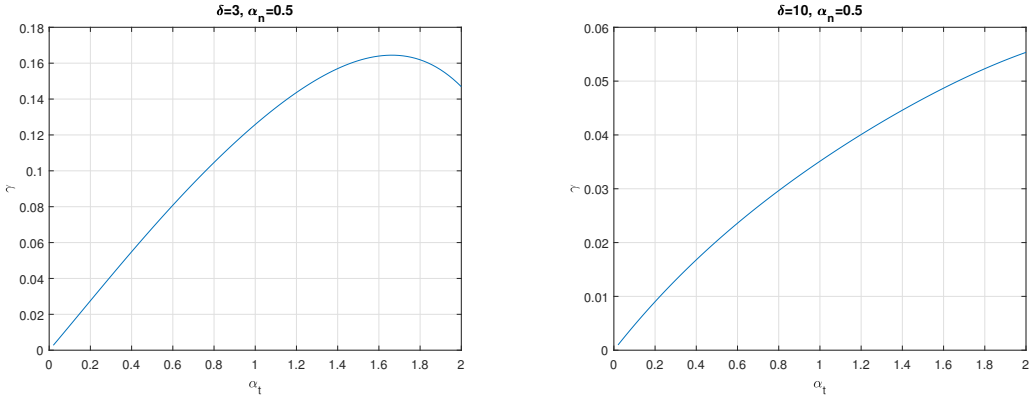

(a) $\delta = 3$, $\alpha_n = 0.5$. (b) $\delta = 10$, $\alpha_n = 0.5$.

Figure 3.10.: $\gamma = \gamma(\alpha_t)$ for δ small and intermediate and $\alpha_n < 0.75$ fixed.

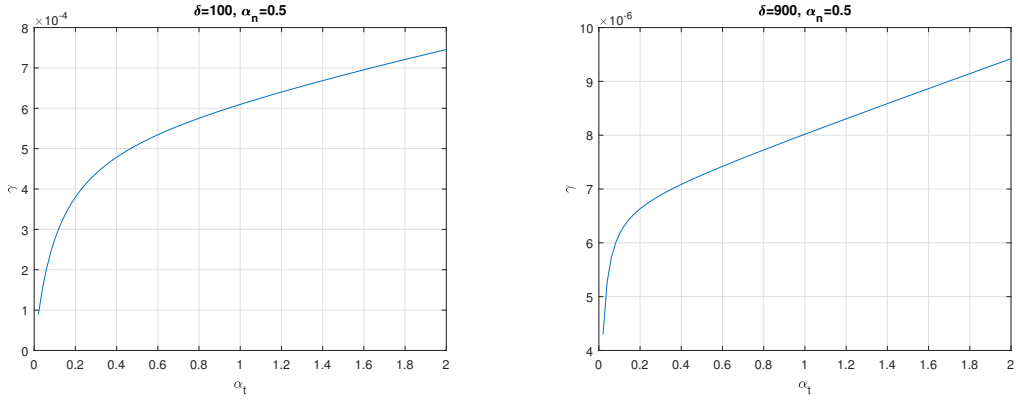

(a) $\delta = 100$, $\alpha_n = 0.5$. (b) $\delta = 900$, $\alpha_n = 0.5$.

Figure 3.11.: $\gamma = \gamma(\alpha_t)$ for δ big and $\alpha_n < 0.75$ fixed.

$\alpha_n < 0.75$: γ has a maximum for small δ (> 3) and becomes strictly increasing for bigger δ (Fig. 3.10); from $\delta > 100$ (and more and more evidently as δ increases) it starts to show a sort of boundary layer for small α_t, where it grows faster than for bigger values of α_t; out of this boundary layer, it is almost linear (Fig. 3.11).

$\alpha_n \geq 0.75$: γ is strictly increasing for every $\delta > 3$ (Fig. 3.12); from $\delta > 100$ (and more and more evidently as δ increases) it starts to show again the boundary layer (Fig. 3.13); out of it, γ is almost linear, and almost constant for $\alpha_n = 1$.

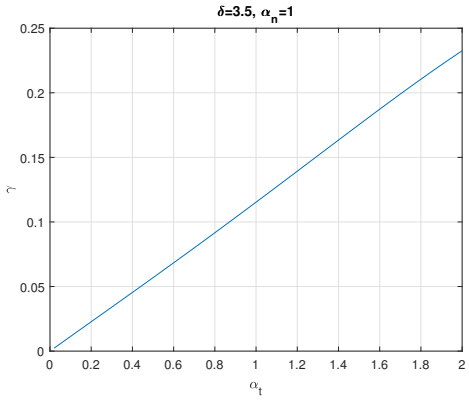

(a) $\delta = 3.5$, $\alpha_n = 1$.

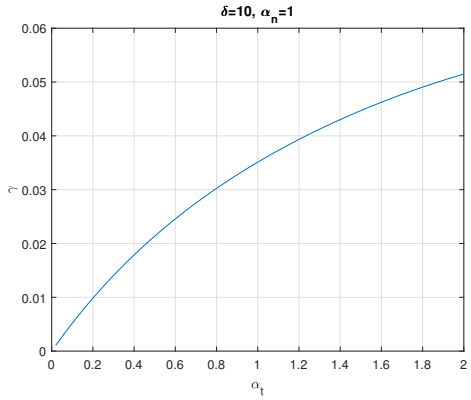

(b) $\delta = 10$, $\alpha_n = 1$.

Figure 3.12.: $\gamma = \gamma(\alpha_t)$ for δ small and intermediate and $\alpha_n = 1$.

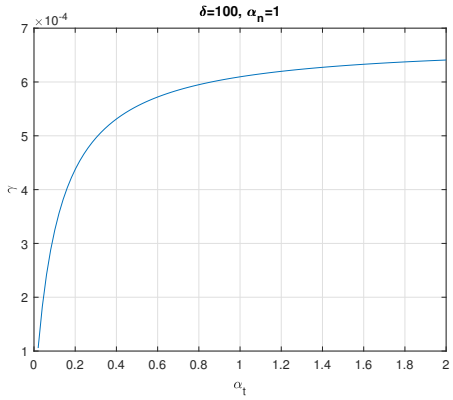

(a) $\delta = 100$, $\alpha_n = 1$.

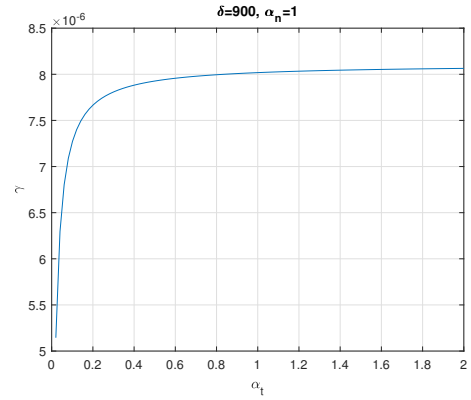

(b) $\delta = 900$, $\alpha_n = 1$.

Figure 3.13.: $\gamma = \gamma(\alpha_t)$ for δ big and $\alpha_n = 1$.

3.3. Series expansion

In this section, we approximate the TPD exponent γ with the series expansion of Eq. (3.19) truncated at order n in $1/\delta$: precisely, we rewrite γ as

$$\gamma = \frac{\frac{\sigma_1^T}{\delta} + \frac{\sigma_2^T}{\delta^2}}{\frac{\delta}{\sigma_0^P}\left(1 + \frac{\sigma_0^P\sigma_1^P}{\delta} + \frac{\sigma_0^P\sigma_2^P}{\delta^2}\right)} = \frac{\frac{\sigma_0^P}{\delta}\left(\frac{\sigma_1^T}{\delta} + \frac{\sigma_2^T}{\delta^2}\right)}{1 + \frac{\sigma_0^P\sigma_1^P}{\delta} + \frac{\sigma_0^P\sigma_2^P}{\delta^2}} = \frac{\frac{\sigma_0^P}{\delta^2}\left(\sigma_1^T + \frac{\sigma_2^T}{\delta}\right)}{1 + \left(\frac{\sigma_0^P\sigma_1^P}{\delta} + \frac{\sigma_0^P\sigma_2^P}{\delta^2}\right)} \tag{3.58}$$

and develop the denominator in the form $\frac{1}{1+x} = 1 - x + x^2 - x^3 + ...$ for $x \ll 1$.

3.3.1. Order 2

$$\left(1 + \frac{\sigma_0^P\sigma_1^P}{\delta} + \frac{\sigma_0^P\sigma_2^P}{\delta^2}\right)^{-1} = 1 - \dots$$

Hence:

$$\gamma_{(2)} = \frac{\sigma_0^P\sigma_1^T}{\delta^2}\,, \tag{3.59}$$

which resembles what is reported in [71]. The subscript $_{(2)}$ denotes the order of truncation.
We recall the expressions of the parameters:

$$\sigma_0^P = (4\sqrt{\pi})^{-1}\left[\frac{96}{\pi}\hat{J}_1 + 48\sqrt{\pi}\right] \simeq 5.8883$$

$$\sigma_1^T = \left[64\hat{J}_4\left(\frac{2\hat{J}_1}{\pi^{3/2}} + 1\right)\right]^{-1}\left[16\left(5\hat{J}_1 - 10\hat{J}_3 + 2\hat{J}_4\right) + 10\pi^{3/2}\left(\alpha_t + \alpha_n - \alpha_t\alpha_n + 4\right)\right]$$

We are interested in studying the dependence of γ on δ and on the accommodation coefficients α_t and α_n.

3.3.1.1. $\gamma_{(2)}$ for fixed δ and varying α_t and α_n

$\gamma_{(2)}$ is always positive, for every (α_t, α_n) and for every δ (Fig. 3.14). Moreover, we observe clearly the trend $\gamma_{(2)} \to 0$ as $\delta \to \infty$, which is now uniform in the whole domain.
A comparison with the reference γ for the same δ shows that even for a pretty big δ ($\delta = 20$, Fig. 3.15) there is a visible discrepancy: the minimum relative difference (which happens for $\alpha_t = 2$) is still 15%, and even quite far from the boundary layer in $\alpha_t = 0$ (precisely, in $\alpha_t = 1$) the difference is 40%.
Only for $\delta = 100$ (Fig. 3.16) we reach a 10% discrepancy also for α_t closer to the boundary layer ($\alpha_t = 0.8$).
Finally, $\gamma_{(2)}$ always overestimate the actual reference value of γ, for every (α_t, α_n) and for every δ.

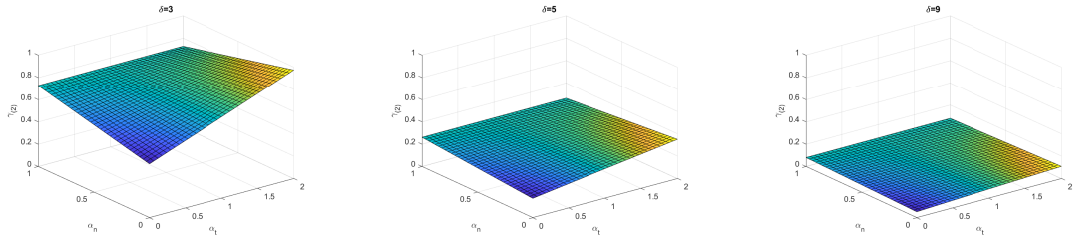

(a) $\delta = 3$. (b) $\delta = 5$. (c) $\delta = 9$.

Figure 3.14.: $\gamma_{(2)} = \gamma_{(2)}(\alpha_t, \alpha_n)$ for different fixed δ.

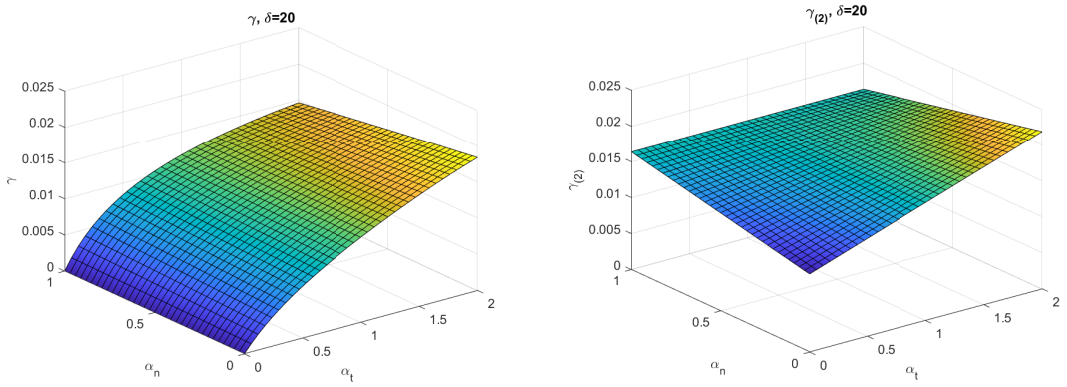

(a) $\gamma = \gamma(\alpha_t, \alpha_n)$, $\delta = 20$. (b) $\gamma_{(2)} = \gamma_{(2)}(\alpha_t, \alpha_n)$, $\delta = 20$.

Figure 3.15.: Comparison between γ and $\gamma_{(2)}$ for quite large δ.

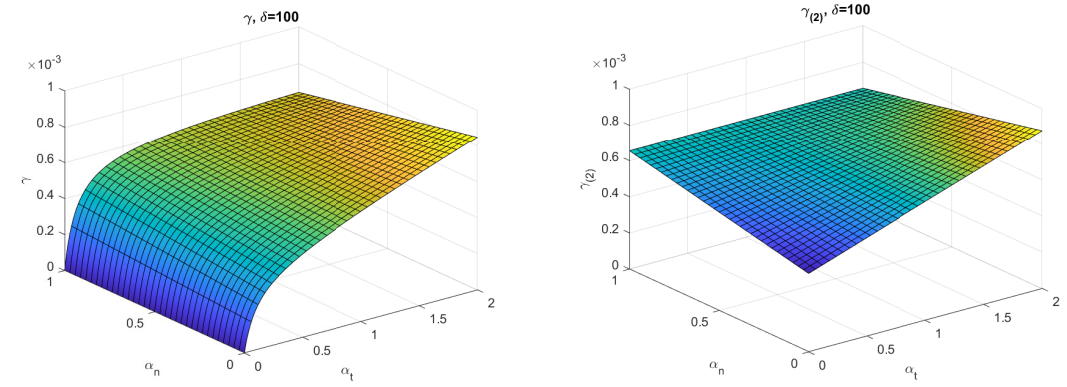

(a) $\gamma = \gamma(\alpha_t, \alpha_n)$, $\delta = 100$. (b) $\gamma_{(2)} = \gamma_{(2)}(\alpha_t, \alpha_n)$, $\delta = 100$.

Figure 3.16.: Comparison between γ and $\gamma_{(2)}$ for large δ.

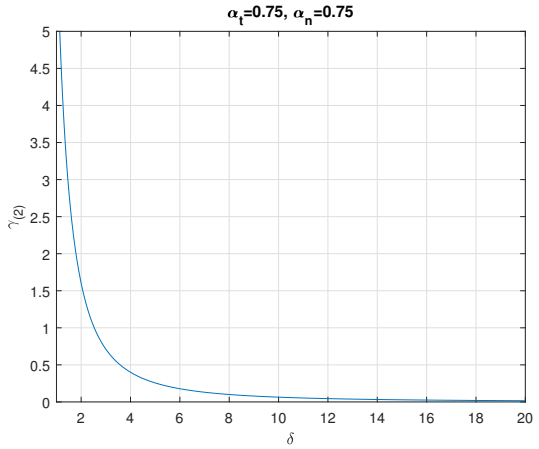

Figure 3.17.: $\gamma_{(2)} = \gamma_{(2)}(\delta)$ for α_t and α_n fixed: the qualitative behaviour is the same for every choice of the accommodation coefficients.

3.3.1.2. $\gamma_{(2)}$ for fixed α_t and α_n and varying δ

For what concerns the behaviour with respect to δ, we have that $\gamma_{(2)} \propto 1/\delta^2$, therefore:

1. $\delta \to 0 \quad \Rightarrow \quad \gamma_{(2)} \to \infty$;
2. $\delta \to \infty \quad \Rightarrow \quad \gamma_{(2)} \to 0$
3. $\gamma_{(2)}$ is strictly decreasing for every δ.

As we already know very well by then, case 1 is well out of the domain of validity even for the original model (as well as physically wrong). Moreover, case 3 is physically consistent in principle, so we cannot use the lack of monotonicity to assess a lower bound for δ (as we did in Section 3.2.2.2). Finally, for what concerns case 2, we have that $\gamma_{(2)}$ tends to zero as $\delta \to \infty$ with the correct asymptotic trend. The overall qualitative behaviour is the same for every choice of the parameters α_t and α_n (see Fig. 3.17).

We can perform the same kind of analysis as in Section 3.2.2.2, that is, we consider how $\gamma_{(2)}$ changes using different values of an accommodation coefficient, keeping the other one fixed. For example, we fix α_t and we let α_n span the whole interval $[0, 1]$. Looking at Fig. 3.18, we can see that the behaviour is somewhat specular with respect to $\alpha_t = 1$: as α_t increases, but always remaining less than 1, the bundle of curves, parametrized by α_n, shrinks, until $\alpha_t = 1$, for which the bundle is actually formed by just one curve (we trivially observe that if $\alpha_t = 1$ then, due to a simplification in σ_1^T, $\gamma_{(2)}$ is independent of α_n); as soon as $\alpha_t > 1$ the bundle starts to spread again. Moreover, as α_n increases, the curve "moves" in opposite directions depending on whether α_t is bigger or smaller than 1. Now we note that $\gamma_{(2)}$ is symmetric with respect to the exchange $\alpha_t \leftrightarrow \alpha_n$: if we write α_n in place of α_t and viceversa, $\gamma_{(2)}$ is unchanged. Therefore, thanks to this trivial observation, the analysis for the opposite case, in which we fix α_n and we let α_t vary, is straightforwardly recovered from what we just said. The only difference is that α_t goes from 0 to 2, while α_n only from 0 to 1: the simple consequence is that the bundle will be wider.

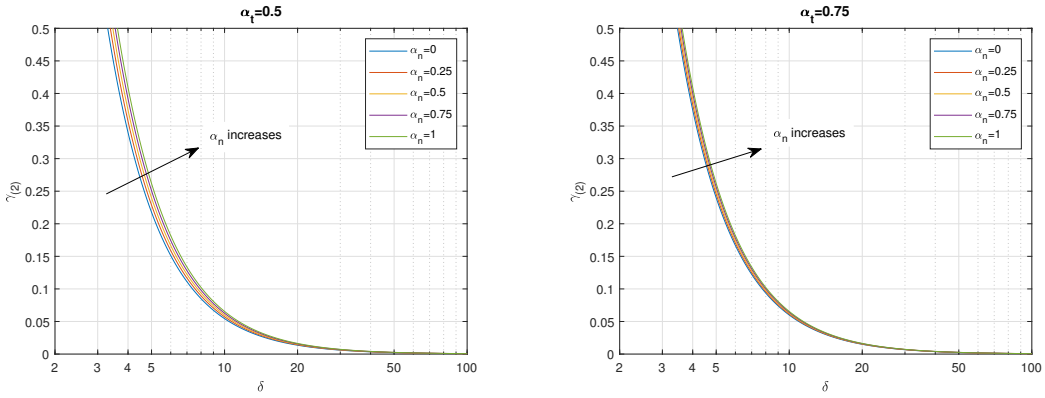

(a) $\alpha_t = 0.5$.

(b) $\alpha_t = 0.75$.

(c) $\alpha_t = 1.25$.

(d) $\alpha_t = 1.5$.

Figure 3.18.: $\gamma_{(2)} = \gamma_{(2)}(\delta)$ for α_t fixed and different α_n.

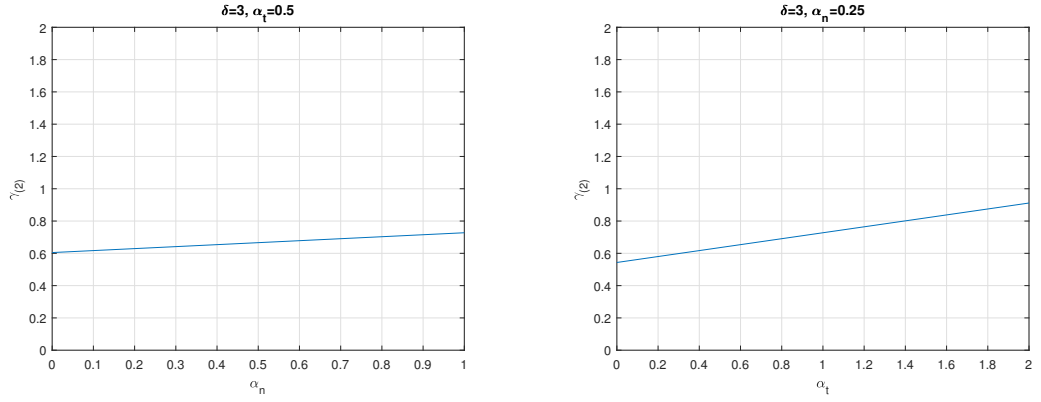

(a) $\delta = 3$, $\alpha_t = 0.5$.

(b) $\delta = 3$, $\alpha_n = 0.25$.

Figure 3.19.: $\gamma_{(2)}$ for the fixed accommodation coefficient strictly smaller than 1.

3.3.1.3. $\gamma_{(2)}$ for fixed δ and fixed one of the two accommodation coefficients, letting the other vary

Thanks to the previous observation, we can talk about *varying* and *fixed* accommodation coefficient (AC), without specifying which is α_n and which is α_t. Hence, let us fix one of the AC and vary the other, thinking of $\gamma_{(2)}$ as a function of δ and of the varying AC only. It is easily seen that $\gamma_{(2)}$ is:

- linear with respect to the varying AC;
- strictly increasing (decreasing) if the fixed AC is chosen strictly smaller (bigger) than 1 (Figs. 3.19 and 3.20);
- constant if the fixed AC is chosen equal to 1.

The first two points (linearity and monotonicity) coincide with the results of Section 3.2.2 for the case of δ large (cfr Figs. 3.7, 3.8, 3.11 and 3.13). For what concern the third point (constantness): for δ fixed, the reference γ was actually constant with respect to α_n if $\alpha_t = 1$, but not with respect to α_t if $\alpha_n = 1$. Anyway, the last statement tends to become true for (very) large δ (see Fig. 3.13). Moreover, for any choice of the fixed AC, the percent variation of $\gamma_{(2)}$ as the free AC varies is always the same (up to all the digits after the decimal point that MATLAB® allows) for every δ, and this percent variation gets smaller as the fixed AC gets closer to 1. We have already discussed (Section 3.2.2.3) what a constant and a small percent variation mean from a practical point of view. The difference is that here $\Delta_{\%}$ is constant through all the regimes of rarefaction, while in the previous model it was approximately constant only for large δ.

The conclusion is that the result of the approximated model are qualitatively recovered through the reference one by letting δ increase, as one should actually expect. Nonetheless, the quantitative agreement is good only for δ very big, almost in the hydrodynamic regime: therefore, it is likely that the approximated model is not suitable if the aim is to model the boundary conditions of a pressure- and temperature-driven flow, or to discriminate with high accuracy the actual domain of validity of a description which couples Navier-Stokes equations and higher-order slip boundary conditions.

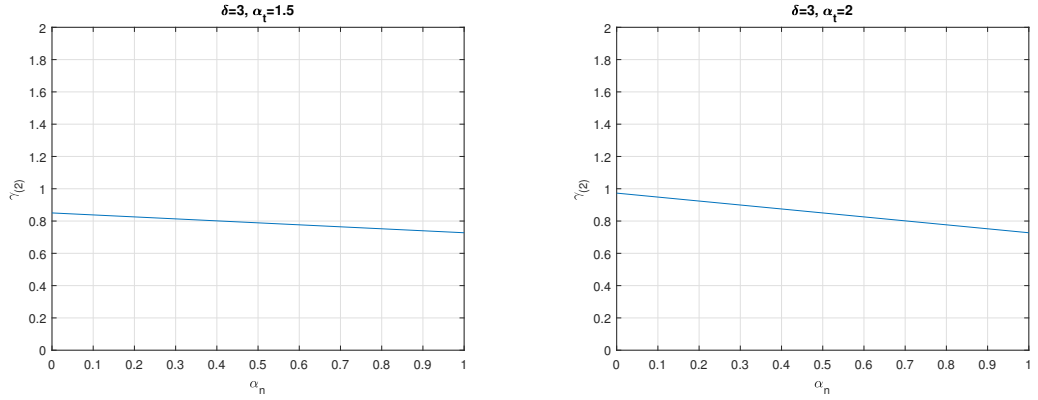

(a) $\delta = 3$, $\alpha_t = 1.5$. (b) $\delta = 3$, $\alpha_t = 2$.

Figure 3.20.: $\gamma_{(2)}$ for the fixed accommodation coefficient strictly bigger than 1

A final remark could be made on the physical meaning of the symmetry of $\gamma_{(2)}$ with respect to the exchange α_n with α_t and viceversa: this fact may be an indication that at large δ the two-parameter CL model may be reduced to a single-parameter one.

3.3.2. Higher orders

For the next orders, we limit ourselves to give the expression of the approximated γ, without any numerical or graphical analysis.

3.3.2.1. Order 3

$$\left(1 + \frac{\sigma_0^P \sigma_1^P}{\delta} + \frac{\sigma_0^P \sigma_2^P}{\delta^2}\right)^{-1} = 1 - \left(\frac{\sigma_0^P \sigma_1^P}{\delta} + \frac{\sigma_0^P \sigma_2^P}{\delta^2}\right) + \dots$$

Hence:

$$\gamma = \frac{\sigma_0^P \sigma_1^T}{\delta^2} + \frac{\sigma_0^P (\sigma_2^T - \sigma_0^P \sigma_1^P \sigma_1^T)}{\delta^3}\,. \tag{3.60}$$

3.3.2.2. Order 4

$$\begin{aligned}\left(1 + \frac{\sigma_0^P \sigma_1^P}{\delta} + \frac{\sigma_0^P \sigma_2^P}{\delta^2}\right)^{-1} &= 1 - \left(\frac{\sigma_0^P \sigma_1^P}{\delta} + \frac{\sigma_0^P \sigma_2^P}{\delta^2}\right) + \left(\frac{\sigma_0^P \sigma_1^P}{\delta} + \frac{\sigma_0^P \sigma_2^P}{\delta^2}\right)^2 + \dots \\ &= 1 - \frac{\sigma_0^P \sigma_1^P}{\delta} - \frac{\sigma_0^P \sigma_2^P}{\delta^2} + \frac{(\sigma_0^P \sigma_1^P)^2}{\delta^2} + \dots\end{aligned}$$

Hence:

$$\gamma = \frac{\sigma_0^P \sigma_1^T}{\delta^2} + \frac{\sigma_0^P (\sigma_2^T - \sigma_0^P \sigma_1^P \sigma_1^T)}{\delta^3} + \frac{-{\sigma_0^P}^2 (\sigma_1^P \sigma_2^T + \sigma_2^P \sigma_1^T - \sigma_0^P {\sigma_1^P}^2 \sigma_1^T)}{\delta^4}\,. \tag{3.61}$$

3.3.2.3. Order 5

$$\left(1+\frac{\sigma_0^P\sigma_1^P}{\delta}+\frac{\sigma_0^P\sigma_2^P}{\delta^2}\right)^{-1} = 1-\left(\frac{\sigma_0^P\sigma_1^P}{\delta}+\frac{\sigma_0^P\sigma_2^P}{\delta^2}\right)+\left(\frac{\sigma_0^P\sigma_1^P}{\delta}+\frac{\sigma_0^P\sigma_2^P}{\delta^2}\right)^2-\left(\frac{\sigma_0^P\sigma_1^P}{\delta}+\frac{\sigma_0^P\sigma_2^P}{\delta^2}\right)^3+\dots$$
$$= 1-\frac{\sigma_0^P\sigma_1^P}{\delta}-\frac{\sigma_0^P\sigma_2^P}{\delta^2}+\frac{(\sigma_0^P\sigma_1^P)^2}{\delta^2}+2\frac{{\sigma_0^P}^2\sigma_1^P\sigma_2^P}{\delta^3}-\frac{{\sigma_0^P}^3{\sigma_1^P}^3}{\delta^3}+\dots$$

Hence:

$$\gamma = \frac{\sigma_0^P\sigma_1^T}{\delta^2}+\frac{\sigma_0^P(\sigma_2^T-\sigma_0^P\sigma_1^P\sigma_1^T)}{\delta^3}+\frac{-{\sigma_0^P}^2(\sigma_1^P\sigma_2^T+\sigma_2^P\sigma_1^T-\sigma_0^P{\sigma_1^P}^2\sigma_1^T)}{\delta^4}$$
$$+\frac{-{\sigma_0^P}^2(\sigma_2^P\sigma_2^T-\sigma_0^P\sigma_1^P{}^2\sigma_2^T-2\sigma_0^P\sigma_1^P\sigma_2^P\sigma_1^T+{\sigma_0^P}^2{\sigma_1^P}^3\sigma_1^T)}{\delta^5}\,. \tag{3.62}$$

3.4. Comparison with numerical results: reliability of the variational approach

In this section, we present briefly the numerical results reported in [24] and compare them with our analytical solution.

The assumptions are the same of our model: the authors consider the LBE for a gas of hard spheres between two infinite parallel plates with Cercignani-Lampis boundary conditions and the true linearized collision operator. The difference with our work is that they directly solve numerically the LBE, without resorting to any variational method or analytical or semi-analytical approach. Therefore, their analysis holds for a wider range of rarefaction regimes, but coding and computational effort are not a trivial issue.
Making use of the Onsager-Casimir relation (with a different sign convention as it was written in previous sections)

$$G_T = -Q_P\,, \tag{3.63}$$

where Q_P is the heat flow rate in Poiseuille flow (that is, heat flow due to the mechanocaloric effect), the authors limit their attention to the Poiseuille problem, considering both mass and heat flow rate, rather than compute only mass flow rate but in two different cases (Poiseuille flow and thermal creep).
Therefore, γ can be rewritten as

$$\gamma = -\frac{Q_P}{G_P}\,. \tag{3.64}$$

The main points highlighted in the paper concerning the behaviour of Q_P and G_P are the following:

- fixed accommodation coefficients: Q_P always increases when δ decreases, while G_P first decreases and then increases with δ, with the minimum (Knudsen minimum, see [54]) at $\delta \approx 1$ (see Figs. 3.21a and 3.21b);
- δ and α_n fixed: G_P increases rapidly when α_t decreases;
- δ and α_t fixed: G_P increases slightly when α_n increases (decreases) if $\alpha_t > 1$ ($\alpha_t < 1$), and does not change if $\alpha_t = 1$;

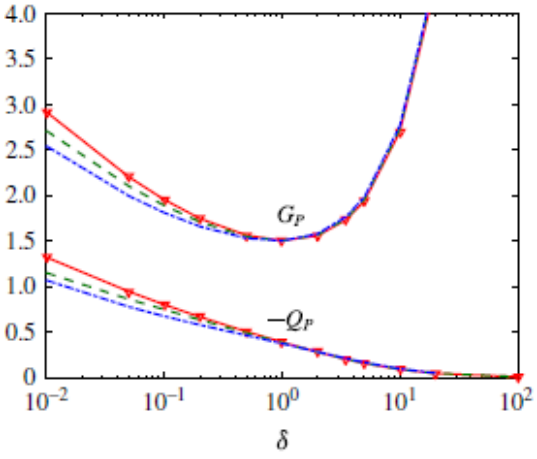

(a) CL b.c.: $\alpha_t = 1$, $\alpha_n = 1$.

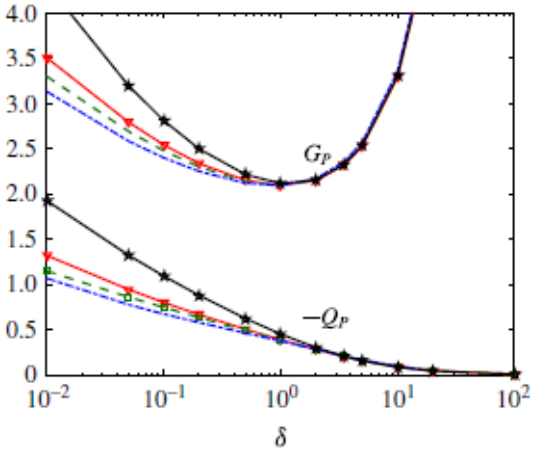

(b) CL b.c.: $\alpha_t = 0.75$, $\alpha_n = 1$. Maxwell b.c.: $\alpha = 0.75$.

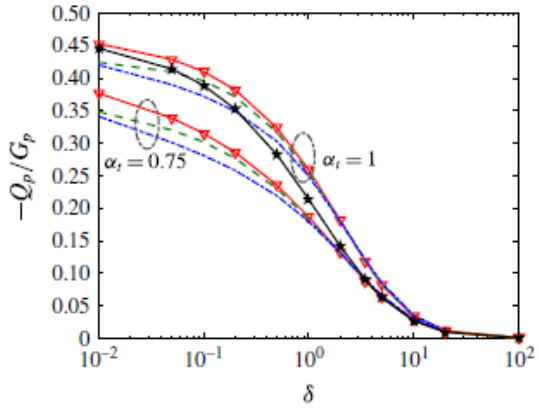

(c) The TPD exponent, γ.

Figure 3.21.: G_P, Q_P and the TPD exponent in the Poiseuille flow between two parallel plates, when the Cercignani-Lampis and Maxwell boundary conditions are used. Triangles: hard-spheres molecules (CL b.c.). Dashed lines: helium (CL b.c.). Dash-dotted lines: xenon (CL b.c.). Pentagrams: hard-spheres molecules (Maxwell b.c.). (from [24])

- δ and α_n fixed: Q_P increases slightly with α_t at large values of δ ($\simeq \delta > 3$), and increases with decreasing α_t at small values of δ ($\simeq \delta < 2.5$);
- δ and α_t fixed: Q_P decreases slightly when α_n increases (decreases) if $\alpha_t < 1$ ($\alpha_t > 1$) and if δ is small ($\simeq \delta < 2.5$), viceversa with large values of δ ($\simeq \delta > 3$), and does not change if $\alpha_t = 1$ (it can be proven that in this case the CL boundary condition is reduced to the diffuse boundary condition).

For what concerns the interval of δ of interest for us, we can immediately deduce that:

- fixed accommodation coefficients: γ is surely strictly decreasing as δ increases for δ larger than the Knudsen minimum;
- δ and α_n fixed: γ surely strictly increasing with α_t for $\delta > 3$;
- δ and α_t fixed: γ constant with respect to α_n if $\alpha_t = 1$, surely strictly increasing (decreasing) if $\alpha_t < 1$ ($\alpha_t > 1$) at large δ.

δ	α_t	$\alpha_n = 0.25$	$\alpha_n = 0.5$	$\alpha_n = 0.75$	$\alpha_n = 1$
3.5	0.5	0.0571	0.0577	0.0580	0.0586
	1	0.1160	0.1160	0.1160	0.1160
	1.5	0.1768	0.1758	0.1739	0.1722
10	0.5	0.01844	0.01907	0.01968	0.02025
	1	0.03298	0.03298	0.03298	0.03298
	1.5	0.04538	0.04410	0.04280	0.04158
20	0.5	0.00709	0.00738	0.00765	0.00791
	1	0.01101	0.01101	0.01101	0.01101
	1.5	0.01387	0.01346	0.01303	0.01258
100	0.5	4.674e-4	4.833e-4	5.041e-4	5.250e-4
	1	5.719e-4	5.719e-4	5.719e-4	5.719e-4
	1.5	6.459e-4	6.276e-4	6.038e-4	5.858e-4

Table 3.1.: γ for HS molecules between two infinite parallel plates, obtained from the linearized Boltzmann equation with the Cercignani-Lampis boundary conditions ([24] reports the values of G_P and Q_P, γ is computed by a plain ratio).

The exact values of γ computed in [24] are reported in Table 3.1.

It is definitely worth noting that in [24] the influence of the intermolecular potential between gas molecules is also investigated, as one can see from Figs. 3.21a and 3.21b. The influence of the intermolecular potential is obvious at small values of δ ($\delta < 1$). On the other hand, for $\delta > 2$ the results derived from the Boltzmann equation for hard-spheres and for the Lennard-Jones potential (which is considered a realistic potential) are closely related to each other: therefore, our use of the rigid spheres does not represent a limitation with respect to the generality of our results.
Finally, we highlight that we can consider Fig. 3.21c as a reliable substitute of actual experimental data (compare, e.g., with Fig. 11 and Fig. 12 of [72]), at least in a qualitative sense: in particular, we observe a clear inflection point at around $\delta = 1$, and a probable limit to a constant value as $\delta \to 0$, which has to be, as we know from the theory, $\gamma = 0.5$.

We now proceed with the comparison between the numerical results reported in [24] (Table 3.1) and the ones computed via our analytical expressions, which have been presented in Section 3.2 and Section 3.3.

3.4.1. Reference values

The comparison with the relative discrepancies between the results given in [24] and the ones computed via our reference model Eq. (3.19) is reported in Table 3.2.
The discrepancy is less than 10% already for $\delta = 3.5$, apart for small δ ($\delta = 3.5$), large α_t ($\alpha_t = 1.5$) and small α_n ($\alpha_n = 0.25, 0.5$): however, this may be expected, since it has already been noticed that our model is unreliable if $\delta \simeq 3$, α_t is large and α_n is small. For $\delta \geq 20$, the match is a bit better for small α_t.
We observe that for δ small (e.g., $\delta = 3.5$) and α_t fixed, the qualitative behaviour of γ with respect to α_n is the opposite in the two cases:

- if $\alpha_t < 1$, our reference γ decreases as α_n increases, while the numerical values from [24] increase with α_n;

- if $\alpha_t > 1$, reference γ increases with α_n, while the numerical values from [24] decrease as α_n increases.

Moreover, we can observe that, apart from the border case $\delta = 3.5$, the reference γ systematically overestimate the "true" numerical result.

3.4.2. Truncation at order 2

The comparison with the relative discrepancies between the results given in [24] and the ones computed via the truncated model Eq. (3.59) is reported in Table 3.3.
Approximating γ with only the second order in $1/\delta$ is not enough to have good numerical results: this approximation does not make sense for $\delta \leq 10$, especially with small α_t, and with $\delta = 100$ we still have a discrepancy of $10 - 25\%$.
This was to be expected too, since $\gamma_{(2)}$ always overestimates γ, for every (α_t, α_n) and for every δ, and the deviation is practically a non-sense for α_t small, even for δ quite big, because of the boundary layer of γ.

3.4.3. Truncation at higher orders

If we try to obtain a better approximation by using higher-order truncations of the reference model, that is, $\gamma_{(n)}$ given by Eqs. (3.60) to (3.62), things do not get much better (see Tables 3.4 to 3.6):

- for small δ and small α_t the absolute value of $\gamma_{(n)}$ explodes, and we even have a negative sign if the order of approximation is odd ($n = 3, 5$), while for big α_t the different values of γ become at least comparable;

- for bigger δ, the discrepancy between approximations and numerical results is comparable with the one between numerical results and the reference value, but we still have some problems for too small δ if α_t is small.

3.4.4. Conclusion

To conclude, we can say that we found our reference model quite satisfactory: the variational approach turned out to be a powerful technique in order to obtain fairly accurate numerical results with trivial coding and negligible computational effort.
The same surely does not hold for the series expansions of various orders of the reference γ, presented in Section 3.3: they are not suitable to obtain accurate numerical results even for $\delta = 10$, especially for small α_t, and they seem to become reliable only for δ very big, for which, conversely, as already noticed, these computations are quite useless.

The physical explanation for this behaviour may be the following. Writing the dimensionless mass fluxes for the Poiseuille and the thermal creep problems as in Eq. (3.13) and Eq. (3.14) respectively, we obtain expressions for the solution of the LBE which involve terms up to the second order in the Knudsen number *Kn* (see, e.g., [27, 73]). A further comparison of these resulting expressions with the solution of the Navier-Stokes equations coupled with the boundary conditions Eq. (2.57) and Eq. (2.57) gives the relations Eqs. (3.15) to (3.18), which links the actual slip coefficients, which appear in the boundary conditions, and the σ coefficients, which appear in the expressions

δ	α_t		$\alpha_n = 0.25$	$\alpha_n = 0.5$	$\alpha_n = 0.75$	$\alpha_n = 1$
3.5	0.5	γ_L	0.0625	0.0609	0.0590	0.0569
		WS	0.0571	0.0577	0.0580	0.0586
		%	9.5	5.5	1.7	-3
	1	γ_L	0.1153	0.1153	0.1153	0.1153
		WS	0.1160	0.1160	0.1160	0.1160
		%	-0.6	-0.6	-0.6	-0.6
	1.5	γ_L	0.1444	0.1554	0.1657	0.1754
		WS	0.1768	0.1758	0.1739	0.1722
		%	-22	-13	-5	1.9
10	0.5	γ_L	0.01974	0.02034	0.02085	0.02136
		WS	0.01844	0.01907	0.01968	0.02025
		%	7.1	6.7	6	5.5
	1	γ_L	0.03511	0.03511	0.03511	0.03511
		WS	0.03298	0.03298	0.03298	0.03298
		%	6.5	6.5	6.5	6.5
	1.5	L	0.04762	0.04670	0.04572	0.04468
		WS	0.04538	0.04410	0.04280	0.04158
		%	5	5.9	6.8	7.5
20	0.5	γ_L	0.00749	0.00779	0.00808	0.00838
		WS	0.00709	0.00738	0.00765	0.00791
		%	5.6	5.6	5.6	5.9
	1	γ_L	0.01173	0.01173	0.01173	0.01173
		WS	0.01101	0.01101	0.01101	0.01101
		%	6.5	6.5	6.5	6.5
	1.5	L	0.01493	0.01447	0.01400	0.01353
		WS	0.01387	0.01346	0.01303	0.01258
		%	7.6	7.5	7.4	7.6
100	0.5	γ_L	4.863e-4	5.093e-4	5.321e-4	5.550e-4
		WS	4.674e-4	4.833e-4	5.041e-4	5.250e-4
		%	4	5.4	5.6	5.7
	1	L	6.096e-4	6.096e-4	6.096e-4	6.096e-4
		WS	5.719e-4	5.719e-4	5.719e-4	5.719e-4
		%	6.6	6.6	6.6	6.6
	1.5	γ_L	7.080e-4	6.821e-4	6.562e-4	6.302e-4
		WS	6.459e-4	6.276e-4	6.038e-4	5.858e-4
		%	9.6	8.7	8.7	7.6

Table 3.2.: γ_L indicates the value of γ obtained by the reference expression Eq. (3.19), WS indicates the value of γ reported in [24]. % is the percent difference between the two values.

δ	α_t		$\alpha_n = 0.25$	$\alpha_n = 0.5$	$\alpha_n = 0.75$	$\alpha_n = 1$
3.5	0.5	$\gamma_{(2)}$	0.4668	0.4894	0.5119	0.5345
		WS	0.0571	0.0577	0.0580	0.0586
		%	720	750	780	810
	1	$\gamma_{(2)}$	0.5345	0.5345	0.5345	0.5345
		WS	0.1160	0.1160	0.1160	0.1160
		%	360	360	360	360
	1.5	$\gamma_{(2)}$	0.6021	0.5796	0.5570	0.5345
		WS	0.1768	0.1758	0.1739	0.1722
		%	240	230	220	210
10	0.5	$\gamma_{(2)}$	0.05719	0.05995	0.06271	0.06547
		WS	0.01844	0.01907	0.01968	0.02025
		%	210	210	220	220
	1	$\gamma_{(2)}$	0.06547	0.06547	0.06547	0.06547
		WS	0.03298	0.03298	0.03298	0.03298
		%	99	99	99	99
	1.5	$\gamma_{(2)}$	0.07376	0.07100	0.06823	0.06547
		WS	0.04538	0.04410	0.04280	0.04158
		%	63	61	59	57
20	0.5	$\gamma_{(2)}$	0.01430	0.01499	0.01568	0.01637
		WS	0.00709	0.00738	0.00765	0.00791
		%	100	100	110	110
	1	$\gamma_{(2)}$	0.01637	0.01637	0.01637	0.01637
		WS	0.01101	0.01101	0.01101	0.01101
		%	49	49	49	49
	1.5	$\gamma_{(2)}$	0.01844	0.01775	0.01706	0.01637
		WS	0.01387	0.01346	0.01303	0.01258
		%	33	32	31	30
100	0.5	$\gamma_{(2)}$	5.719e-4	5.995e-4	6.271e-4	6.547e-4
		WS	4.674e-4	4.833e-4	5.041e-4	5.250e-4
		%	22	24	24	25
	1	$\gamma_{(2)}$	6.547e-4	6.547e-4	6.547e-4	6.547e-4
		WS	5.719e-4	5.719e-4	5.719e-4	5.719e-4
		%	14	14	14	14
	1.5	$\gamma_{(2)}$	7.376e-4	7.100e-4	6.823e-4	6.547e-4
		WS	6.459e-4	6.276e-4	6.038e-4	5.858e-4
		%	14	13	13	12

Table 3.3.: Approximation of order 2: $\gamma_{(2)}$ indicates the value of γ obtained by Eq. (3.59), WS indicates the value of γ reported in [24]. % is the percent discrepancy between the two values.

δ	α_t		$\alpha_n = 0.25$	$\alpha_n = 0.5$	$\alpha_n = 0.75$	$\alpha_n = 1$
3.5	0.5	$\gamma_{(3)}$	-1.8601	-1.9630	-2.0663	-2.1702
		WS	0.0571	0.0577	0.0580	0.0586
		%	-	-	-	-
	1	$\gamma_{(3)}$	-0.5777	-0.5777	-0.5777	-0.5777
		WS	0.1160	0.1160	0.1160	0.1160
		%	-	-	-	-
	1.5	$\gamma_{(3)}$	-0.0969	-0.0799	-0.0636	-0.0477
		WS	0.1768	0.1758	0.1739	0.1722
		%	-	-	-	-
10	0.5	$\gamma_{(3)}$	-0.04258	-0.04520	-0.04783	-0.05049
		WS	0.01844	0.01907	0.01968	0.02025
		%	-	-	-	-
	1	$\gamma_{(3)}$	0.01779	0.01779	0.01779	0.01779
		WS	0.03298	0.03298	0.03298	0.03298
		%	-85	-85	-85	-85
	1.5	$\gamma_{(3)}$	0.04379	0.04272	0.04163	0.04051
		WS	0.04538	0.04410	0.04280	0.04158
		%	-3.6	-3.2	-2.8	-2.6
20	0.5	$\gamma_{(3)}$	0.00183	0.00184	0.00186	0.00187
		WS	0.00709	0.00738	0.00765	0.00791
		%	-290	-300	-310	-320
	1	$\gamma_{(3)}$	0.01041	0.01041	0.01041	0.01041
		WS	0.01101	0.01101	0.01101	0.01101
		%	-5.8	-5.8	-5.8	-5.8
	1.5	$\gamma_{(3)}$	0.01469	0.01421	0.01373	0.01325
		WS	0.01387	0.01346	0.01303	0.01258
		%	5.9	5.6	5.4	5.3
100	0.5	$\gamma_{(3)}$	4.721e-4	4.943e-4	5.166e-4	5.388e-4
		WS	4.674e-4	4.833e-4	5.041e-4	5.250e-4
		%	1	2.3	2.5	2.6
	1	$\gamma_{(3)}$	6.070e-4	6.070e-4	6.070e-4	6.070e-4
		WS	5.719e-4	5.719e-4	5.719e-4	5.719e-4
		%	6.1	6.1	6.1	6.1
	1.5	$\gamma_{(3)}$	7.076e-4	6.817e-4	6.557e-4	6.298e-4
		WS	6.459e-4	6.276e-4	6.038e-4	5.858e-4
		%	9.6	8.6	8.6	7.5

Table 3.4.: Order 3: $\gamma_{(3)}$ indicates the value of γ obtained by Eq. (3.60), WS indicates the value of γ reported in [24]. % is the percent discrepancy between the two values.

δ	α_t		$\alpha_n = 0.25$	$\alpha_n = 0.5$	$\alpha_n = 0.75$	$\alpha_n = 1$
3.5	0.5	$\gamma_{(4)}$	9.201	9.609	10.01	10.40
		WS	0.0571	0.0577	0.0580	0.0586
		%	-	-	-	-
	1	$\gamma_{(4)}$	1.220	1.220	1.220	1.220
		WS	0.1160	0.1160	0.1160	0.1160
		%	-	-	-	-
	1.5	$\gamma_{(4)}$	0.1428	0.1901	0.2320	0.2687
		WS	0.1768	0.1758	0.1739	0.1722
		%	-24	8	33	56
10	0.5	$\gamma_{(4)}$	0.1234	0.1285	0.1334	0.1382
		WS	0.01844	0.01907	0.01968	0.02025
		%	570	570	580	-
	1	$\gamma_{(4)}$	0.04476	0.04476	0.04476	0.04476
		WS	0.03298	0.03298	0.03298	0.03298
		%	36	36	36	36
	1.5	$\gamma_{(4)}$	0.04739	0.04677	0.04606	0.04526
		WS	0.04538	0.04410	0.04280	0.04158
		%	4.4	6.1	7.6	8.9
20	0.5	$\gamma_{(4)}$	0.01220	0.01270	0.01319	0.01367
		WS	0.00709	0.00738	0.00765	0.00791
		%	72	72	72	73
	1	$\gamma_{(4)}$	0.01209	0.01209	0.01209	0.01209
		WS	0.01101	0.01101	0.01101	0.01101
		%	9.8	9.8	9.8	9.8
	1.5	$\gamma_{(4)}$	0.01492	0.01448	0.01401	0.01354
		WS	0.01387	0.01346	0.01303	0.01258
		%	7.6	7.6	7.5	7.6
100	0.5	$\gamma_{(4)}$	4.887e-4	5.117e-4	5.347e-4	5.576e-4
		WS	4.674e-4	4.833e-4	5.041e-4	5.250e-4
		%	4.6	5.9	6.1	6.2
	1	$\gamma_{(4)}$	6.097e-4	6.097e-4	6.097e-4	6.097e-4
		WS	5.719e-4	5.719e-4	5.719e-4	5.719e-4
		%	6.6	6.6	6.6	6.6
	1.5	$\gamma_{(4)}$	7.080e-4	6.821e-4	6.562e-4	6.302e-4
		WS	6.459e-4	6.276e-4	6.038e-4	5.858e-4
		%	9.6	8.7	8.7	7.6

Table 3.5.: Order 4: $\gamma_{(4)}$ indicates the value of γ obtained by Eq. (3.61), WS indicates the value of γ reported in [24]. % is the percent discrepancy between the two values.

δ	α_t		$\alpha_n = 0.25$	$\alpha_n = 0.5$	$\alpha_n = 0.75$	$\alpha_n = 1$
3.5	0.5	$\gamma_{(5)}$	-43.38	-44.98	-46.53	-48.01
		WS	0.0571	0.0577	0.0580	0.0586
		%	-	-	-	-
	1	$\gamma_{(5)}$	-1.640	-1.640	-1.640	-1.640
		WS	0.1160	0.1160	0.1160	0.1160
		%	-	-	-	-
	1.5	$\gamma_{(5)}$	0.2266	0.1993	0.1735	0.1495
		WS	0.1768	0.1758	0.1739	0.1722
		%	28	13	0.23	-15
10	0.5	$\gamma_{(5)}$	-0.1527	-0.1583	-0.1636	-0.1686
		WS	0.01844	0.01907	0.01968	0.02025
		%	-	-	-	-
	1	$\gamma_{(5)}$	0.02974	0.02974	0.02974	0.02974
		WS	0.03298	0.03298	0.03298	0.03298
		%	-11	-11	-11	-11
	1.5	$\gamma_{(5)}$	0.04783	0.04682	0.04576	0.04463
		WS	0.04538	0.04410	0.04280	0.04158
		%	5.4	6.2	6.9	7.3
20	0.5	$\gamma_{(5)}$	0.00357	0.00374	0.00391	0.00408
		WS	0.00709	0.00738	0.00765	0.00791
		%	-99	-97	-96	-94
	1	$\gamma_{(5)}$	0.01162	0.01162	0.01162	0.01162
		WS	0.01101	0.01101	0.01101	0.01101
		%	5.5	5.5	5.5	5.5
	1.5	$\gamma_{(5)}$	0.01493	0.01447	0.01400	0.01353
		WS	0.01387	0.01346	0.01303	0.01258
		%	7.6	7.5	7.4	7.5
100	0.5	$\gamma_{(5)}$	4.859e-4	5.088e-4	5.317e-4	5.546e-4
		WS	4.674e-4	4.833e-4	5.041e-4	5.250e-4
		%	4	5.3	5.5	5.6
	1	$\gamma_{(5)}$	6.096e-4	6.096e-4	6.096e-4	6.096e-4
		WS	5.719e-4	5.719e-4	5.719e-4	5.719e-4
		%	6.6	6.6	6.6	6.6
	1.5	$\gamma_{(5)}$	7.080e-4	6.821e-4	6.562e-4	6.302e-4
		WS	6.459e-4	6.276e-4	6.038e-4	5.858e-4
		%	9.6	8.9	8.7	7.6

Table 3.6.: Order 5: $\gamma_{(5)}$ indicates the value of γ obtained by Eq. (3.62), WS indicates the value of γ reported in [24]. % is the percent discrepancy between the two values.

of the mass fluxes. This means that Eq. (3.13) and Eq. (3.14) are actually solutions of precise and consistent kinetic problems, and therefore a physical meaning may be ascribed to those expressions, although truncated at a certain order in Kn. This is in turn connected with the consistency of the coupling of the Navier-Stokes equations with higher-order boundary conditions, which in this way can supply realistic results well beyond the "usual" slip region, as it is by now generally accepted.
Most likely, the same does not hold for γ: probably, a series expansion of this quantity truncated at a finite order does not give good approximations of the TPD exponent because the truncations themselves does not have a physical meaning on their own.

For this reason, in the following only the reference model will be considered for the numerical computations of the quantity γ.

3.5. Presentation of the experimental results

The experimental data that we will consider refer to the experiment described in [74].

In this article, the thermal transpiration flow through a single channel with a rectangular cross-section is studied for various gas species. Five rare (noble) gases (Helium, Neon, Argon, Krypton and Xenon) and Nitrogen are employed to evaluate the influence of different molecular properties on the thermal transpiration flow. This flow is investigated as a function of the rarefaction parameter δ. The conditions for δ range from 0.7 up to 80 depending on the gas species, which corresponds to the rarefaction range from the transitional to the slip flow regime. The thermal transpiration flow dependence on the gas species is shown by evaluating three common parameters for the final equilibrium characteristics: the thermomolecular pressure difference (Δp), defined as the pressure difference between the hot side and the cold side; the thermomolecular pressure ratio (TPR), which is cold side to hot side pressure ratio; the TPD exponent γ, which we know very well by this time.
Moreover, another kind of data is available for this experiment: precisely, in the same experimental setup also the first- and second-order thermal slip coefficients for all the five noble gases considered (but not for Nitrogen) are measured, and presented in [75].

3.5.1. Experimental method

3.5.1.1. Experimental apparatus

A schematic image of the experimental set-up is shown in Fig. 3.22. The micro-channel has a rectangular cross-section with dimensions: height $H = 0.22 \pm 0.01\,\mathrm{mm}$, width $W = 6\,\mathrm{mm}$, and length $L = 73\,\mathrm{mm}$. The channel was grooved on a plate and covered by a flat plate. The plates were made of polyether ether ketone (PEEK), whose thermal conductivity is low, $0.25\,\mathrm{W\,m^{-1}\,K^{-1}}$. The advantage of this system is that the channel characteristics, such as material, geometry and dimensions, are easily interchangeable. However, a single geometry with a single material is used, in order to study the effect of the gas species on the phenomenon. Note that the geometry presented is consistent with our assumptions made in the theoretical deductions of the analytical expressions: the aspect ratio (height/width) is 27.27, large enough to be well approximated by a planar channel. To realize a temperature gradient along the micro-channel, two blocks with gas

reservoirs inside were placed vertically at each end of the channel. The two blocks were made of stainless steel (1.4301), whose temperatures were controlled by an electrical heater for the hot side and circulating water for the cold side, respectively. The pressure was measured at each reservoir by a high-speed response in time (30 ms) capacitance diaphragm gauge (CDG). The measurement accuracy for the pressure gauges were 0.15 % and 0.2 % for the hot and the cold side, respectively. The absolute pressure was measured by a CDG at the hot side, and the zero point of the CDG at the cold side was set equal to that of the hot side. There was a small difference in temperature between the reservoirs and the CDGs, and a possible parasitic thermal transpiration flow between the reservoir and the CDG for each side was found to be very small by using a semi-empirical formula. The temperature of each block was monitored by a K-type thermocouple (TC) placed on the outside of the blocks, and it was maintained constant during the measurement. However, there might be a small discrepancy between the monitored temperature and that at the channel wall. The hot and the cold reservoirs were connected not only by the micro-channel, but also by a tube with a large diameter compared to the micro-channel, forming a circuit, as in Fig. 3.22. A micro-valve was inserted in the large-diameter tube connection to capture the developed stationary thermal transpiration flow at the beginning of each experiment. The voltage applied to the micro-valve was monitored at 300 Hz to determine a precise closing time. The data from the CDGs and the TCs and the voltage of the micro-valve were captured by a data acquisition system (DAQ). The test section was also connected to a gas supply and a vacuum pump to control the pressure conditions.

3.5.1.2. Measurement procedure

The measurement procedure was as follows. Before the measurement, the whole system was evacuated for a long time, and the temperatures of the hot and the cold sides were set and controlled to a certain value. The temperature of each side was kept constant during the whole procedure. First, the pressure of the flow circuit was set to a certain condition, and then the line to the gas supply and the vacuum pump was disconnected by closing a bellows-sealed valve. At this moment, the pressures of both sides were equal due to the circuit connected by the large-diameter tube. After a certain period needed to stabilize pressure variations due to the closing of the bellows-sealed valve, the micro-valve was closed too. The pressure started to vary due to the thermal transpiration flow from the cold to the hot side. The closing of the micro-valve was monitored by an applied voltage, and the moment, time $t = 0$, was decided from this monitoring signal. Since the pressures of the two sides varied differently according to the thermal transpiration flow, a pressure-driven backflow was induced, and then these flows tended to reach equilibrium. After the pressures of the two reservoirs reached their final equilibrium state, the micro-valve was opened again to confirm the pressure equality after the measurement, accomplished by connecting the tube with a large diameter, and by checking the leakage rate throughout the measurement. The leakage rate was calculated from the pressure variation before closing and after opening the micro-valve, and it was checked to be small enough compared to the thermal transpiration flow rate. The pressure variation due to leakage was subtracted from the experimental pressure data to investigate only the thermal transpiration flow. It is clear that the pressures for both sides are equal to the initial pressure p_i before the closing of the micro-valve at time $t = 0$, and they gradually change their values from $t = 0$ to $t > 0$; the pressure

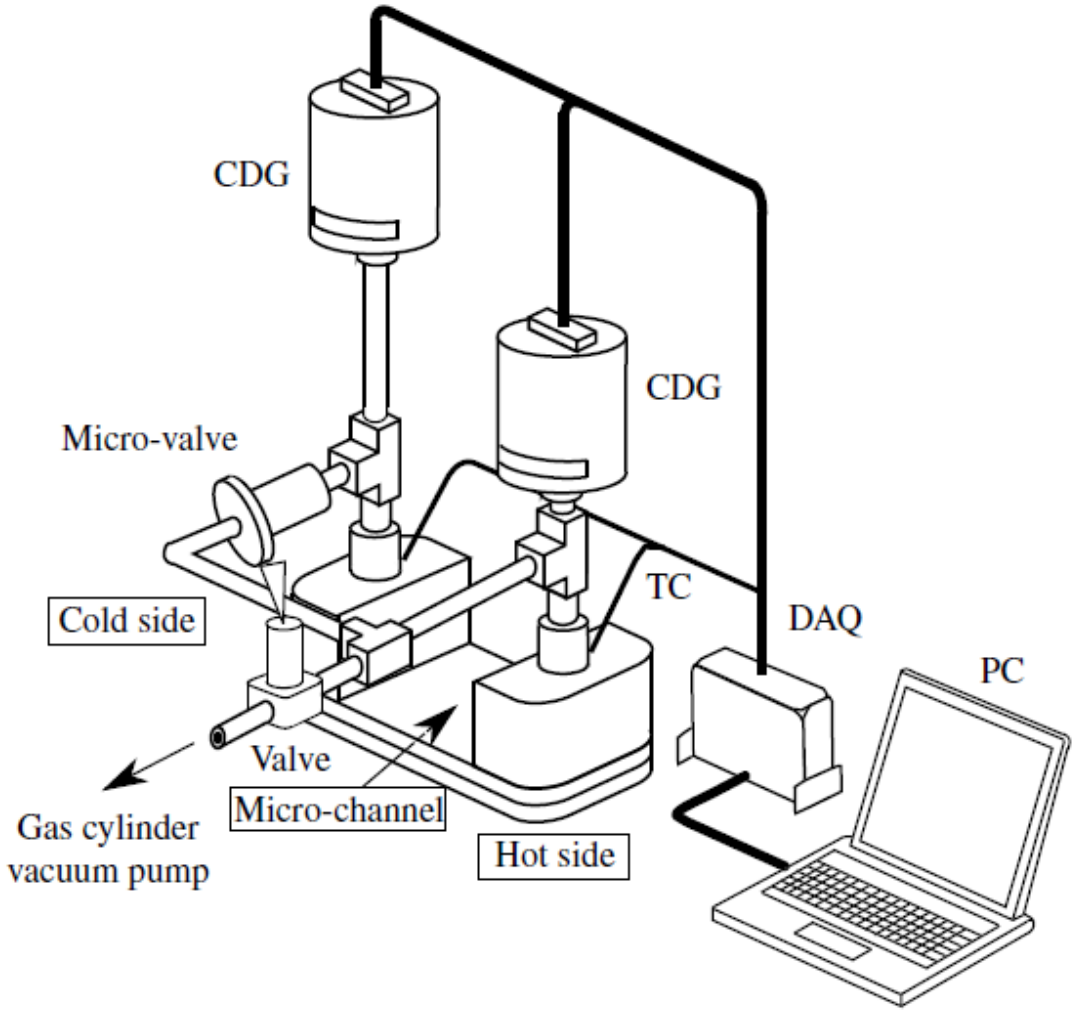

Figure 3.22.: Schematic image of experimental apparatus. Pressures for hot and cold sides were measured by capacitance manometers (CDGs). Temperatures were measured by thermocouples (TCs). Data were recorded by a data acquisition system (DAQ) (from [74]).

decreases in the cold side whereas it increases in the hot side. Then, the pressures reach their final equilibrium states as $p_{h,\infty}$ and $p_{c,\infty}$. The accomplished pressure differences for the cold and the hot sides are not the same due to the difference in volume for each side. Instantly after the opening of the micro-valve, the pressures return to the same initial pressure p_i. A comparison between the speeds of the pressure variation after the closing and the opening of the micro-valve confirms that the diameter of the connecting tubes is large enough.

3.5.1.3. Data analysis

Two series of experiments are performed, with temperatures for the hot and the cold reservoirs fixed to about 346 K and 289 K, and 336 K and 299 K, respectively. The temperature difference ΔT between the hot and the cold sides of every measurement was in the range 57.9 ± 0.6 K and 37.9 ± 0.6 K respectively, where twice the standard deviation (2σ) was used as the uncertainty. For both the experiments, the initial pressure p_i was varied from 66.66 Pa to 1266 Pa for every gas species.

The thermal transpiration flow was evaluated by three parameters for the final equilibrium characteristics: the thermomolecular pressure difference (Δp), the thermomolecular pressure ratio (TPR) and the TPD exponent (γ), defined as

$$\Delta p = p_{h,\infty} - p_{c,\infty}\,, \tag{3.65}$$

$$\mathrm{TPR} = \frac{p_{c,\infty}}{p_{h,\infty}}\,, \tag{3.66}$$

$$\frac{p_{h,\infty}}{p_{c,\infty}} = \left(\frac{T_h}{T_c}\right)^{\gamma}\,. \tag{3.67}$$

It is important to notice that in the above equations Δp is a dimensional value, while TPR and γ are dimensionless values.
These parameters were analysed as a function of the rarefaction parameter

$$\delta = \frac{pL}{\mu v}\,, \tag{3.68}$$

where

$$v = \sqrt{\frac{2k_B T}{m}} \tag{3.69}$$

is the most probable molecular velocity, k_B is the Boltzmann constant, m is the molecular mass, p and T are the gas pressure and temperature, respectively, and L is the characteristic length of the system, represented here by the channel height H. The variable hard-sphere (VHS) model ([18]) was employed to evaluate the gas viscosity

$$\mu = \mu_{\mathrm{ref}} \left(\frac{T}{T_{\mathrm{ref}}}\right)^{\omega}\,, \tag{3.70}$$

where ω is the viscosity index, which depends on the nature of the gas, and μ_{ref} is the gas viscosity at temperature $T_{\mathrm{ref}} = 273$ K.

Since the temperatures of the hot and cold sides were different, the mean temperature $T_{\mathrm{av}} = (T_h + T_c)/2$ was employed in order to characterize the rarefaction level δ for each experiment. Note that T_{av} was the same for each of the two series of experiments,

Gas	Symbol	Mass [amu]
Helium	He	4.002602
Neon	Ne	20.1797
Nitrogen	N_2	28.0134
Argon	Ar	39.948
Krypton	Kr	83.798
Xenon	Xe	131.293

Table 3.7.: Molecular masses of the different gases employed in the experiments.

that is, $T_{\text{av}} = 317.5\,\text{K}$. Let us recall that the temperatures T_h and T_c are maintained constant during the whole experimental series.
The pressure range that was used in order to perform the experimental campaign was the same for the whole of the experimental series, independently of the gas species used. Therefore, it is chosen to characterize a single experiment by associating the rarefaction parameter δ with the initial pressure $p = p_i$, where the thermal transpiration flow is stationary, fully developed and not yet perturbed by the subsequent pressure variation with time. Even if the pressure range chosen for the experimental series did not vary as a function of the gas species used, the rarefaction parameter range did. The rarefaction parameter is directly proportional to the square root of gas molecular mass, too, which makes the rarefaction ranges investigated slightly different for every gas species used. By setting the range of the initial pressure p_i between 66.66 Pa and 1266 Pa, the range varied from 0.7 to 80 when considering all the gas species used. For the different values of the molecular masses of the employed gases we refer to Table 3.7.

It is worth noticing that the experimental data rely on measurements of pressures, and therefore the TPD exponent is computed through its actual definition Eq. (2.67); on the other hand, the analytical expression is derived from mass fluxes, as in Eq. (2.70): any agreement between numerical and experimental results would support the use of the second expression of γ and of the linearization assumption Eq. (2.68).

3.5.2. Results

The Δp turned out to be strongly dependent on the gas species; conversely, TPR and γ, closely related via

$$\gamma = \frac{\ln(p_{h,\infty}/p_{c,\infty})}{\ln(T_h/T_c)} \propto \ln\frac{p_{h,\infty}}{p_{c,\infty}} = -\ln \text{TPR} \tag{3.71}$$

and, therefore, mirror images of each other, are very weakly dependent on the gas species. The explanation for that is exactly that Δp is a dimensional quantity (it is a pressure), while TPR and γ are dimensionless numbers. We underline that γ is calculated directly from its definition as

$$\gamma = \frac{\ln(p_{h,\infty}/p_{c,\infty})}{\ln(T_h/T_c)}\,, \tag{3.72}$$

that is, from measurements of pressure (and temperature) instead of mass fluxes.

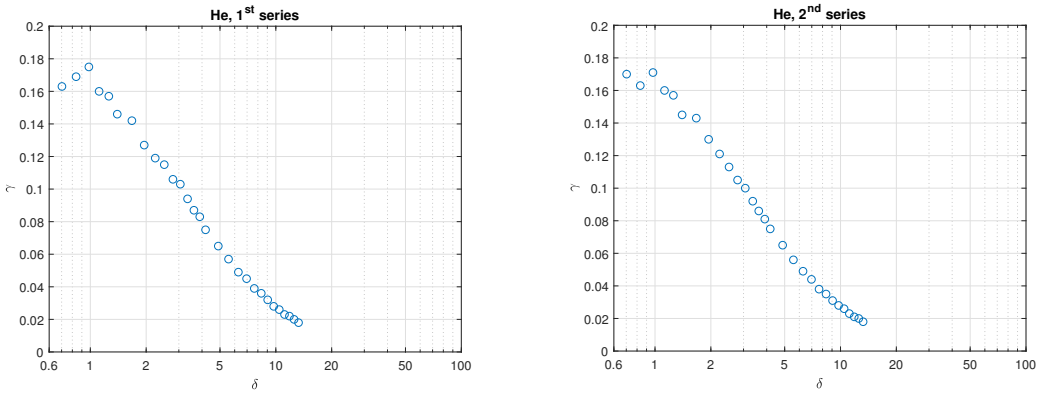

(a) 1^{st} series. (b) 2^{nd} series.

Figure 3.23.: Experimental TPD exponent for He.

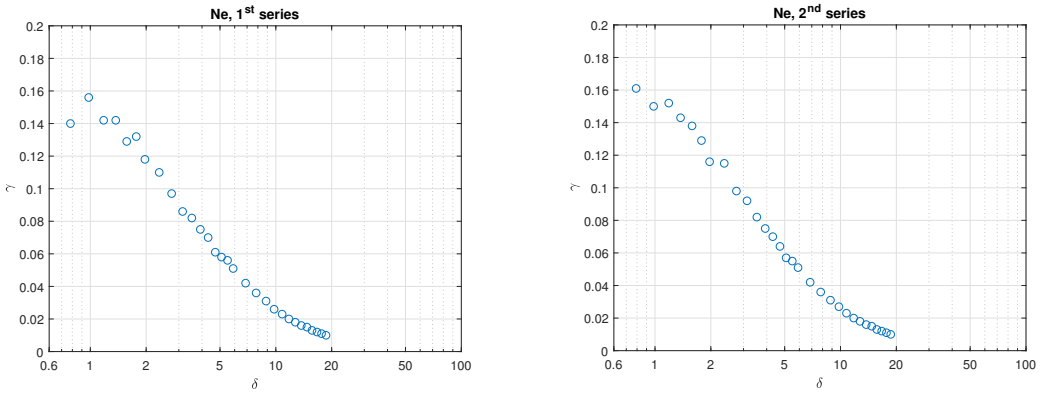

(a) 1^{st} series. (b) 2^{nd} series.

Figure 3.24.: Experimental TPD exponent for Ne.

3.5.2.1. Visualization of the data for the TPD exponent

The plots of the raw data are reported and commented in the following. The expressions "1^{st} series" and "2^{nd} series" refer to the series of experiments with $T_{h,1} = 346\,\mathrm{K}$ and $T_{c,1} = 289\,\mathrm{K}$, and $T_{h,2} = 336\,\mathrm{K}$ and $T_{c,2} = 299\,\mathrm{K}$, respectively. For every gas and every series, approximately 30 different δs are picked, more or less uniformly distributed (in a logarithmic scale). For each plot, we maintain the axes limits to $0.6 \div 100$ (in a logarithmic scale) for the abscissae axis (δ) and to $0 \div 0.2$ for the ordinates axis (γ) to ease visual comparison between different graphs.

In Figs. 3.23 to 3.28 the TPD exponent for each gas and each experimental series separately are reported. It is immediate to observe that the heavier the gas is, the wider the explored range of δ is: for example, we go from 0.6 to 13 for He, and from 2 to 80 for Xe, the two limit cases. For every plot, we note that γ is always strictly decreasing (up to experimental error and statistical fluctuations) and tending to zero as δ goes to infinity.

In Fig. 3.29 we plot in the same graph, for each gas separately, both the experimental series of that gas. We know that, as we said in Section 2.3.2.2, the coefficient γ depends

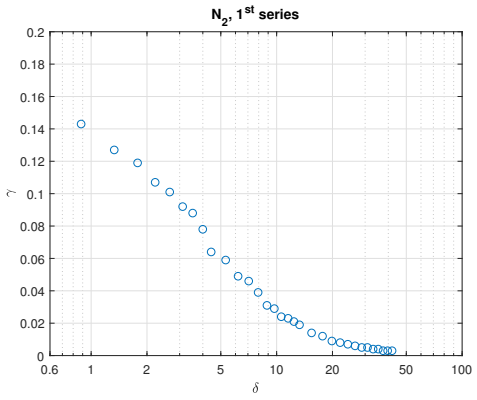

(a) 1^{st} series.

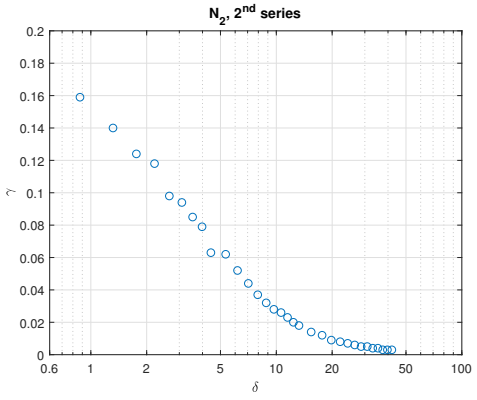

(b) 2^{nd} series.

Figure 3.25.: Experimental TPD exponent for N_2.

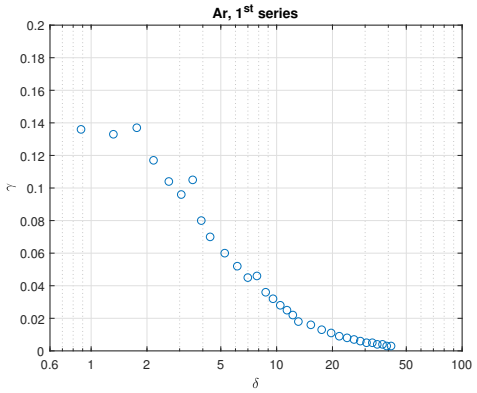

(a) 1^{st} series.

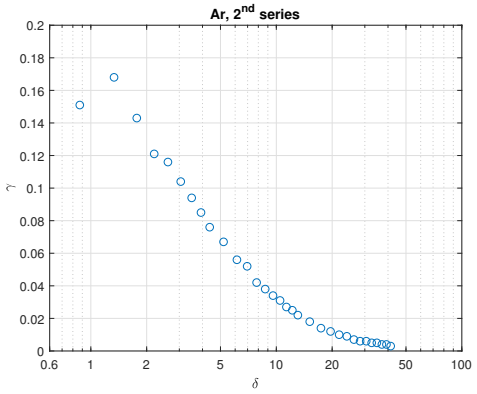

(b) 2^{nd} series.

Figure 3.26.: Experimental TPD exponent for Ar.

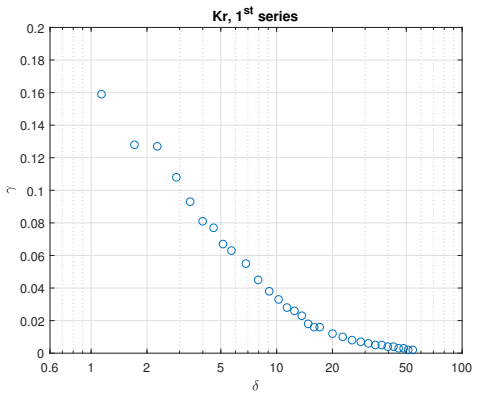

(a) 1^{st} series.

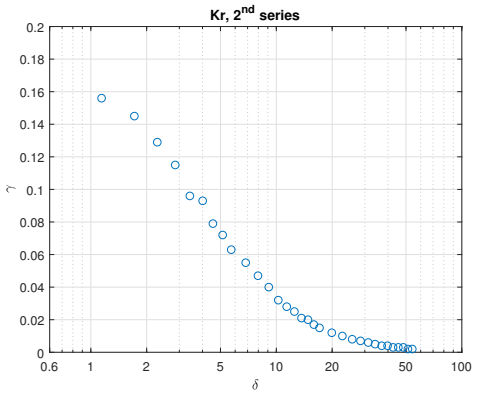

(b) 2^{nd} series.

Figure 3.27.: Experimental TPD exponent for Kr.

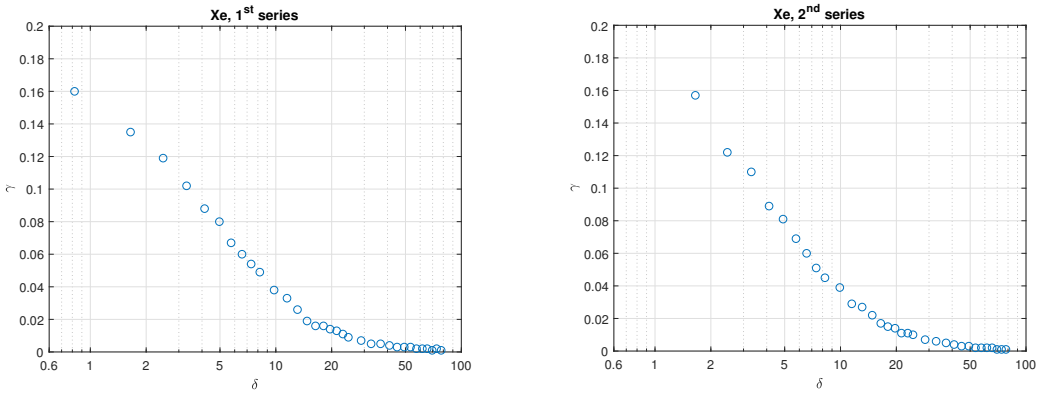

(a) 1^{st} series. (b) 2^{nd} series.

Figure 3.28.: Experimental TPD exponent for Xe.

mainly on geometry of the capillary, type of the gas, nature of the gas-surface interaction and, especially, degree of rarefaction. Moreover, being the range of initial pressures the same for both the experimental series, also the range of δ (that, we recall, is characterized by the value of the initial pressure) is, for each gas singularly, practically the same for both series (depending on the precision of p_i). Therefore, the practical consequence is basically that for each gas we have two values of γ for every δ considered and, since each of the most important parameters on which γ depends are the same in the two series, these two values must be the same. Luckily, this is exactly (up to experimental error and statistical fluctuations) what happens: the overlapping between the data of the two different series is evident, they are indistinguishable. We are then allowed to consider the data of the two experimental series as belonging to the same physical phenomenon: therefore, in the data analysis performed in Section 3.6, we shall merge, for each gas, the two series, treating them as one single experiment, forgetting the origin of the single data.

Finally, in Fig. 3.30, we consider in the same graph, for each series separately, all the gases at the same time. Geometry and material of the channel are always the same, for each gas and each series (the experimental set-up does not change), and the ranges of δ for the different gases largely overlap, so most of the different measurements are comparable, referring to the same regime of rarefaction. The only thing that changes is the gas flowing in the channel, but, apart from the case of nitrogen, this is not a big deal: the noble gases have all very similar physical structure and very similar chemical properties one to each other, so the role of gas-surface interaction is likely to be almost the same. (In principle, a quite different issue may be the case of nitrogen, being not only a non-noble gas, but also non-monatomic.) It seems that the only gas property that varies significantly is the molecular mass: Kr has about half of the mass of Xe, and is twice heavier than Ar and 4 times heavier than Ne, which is 5 times heavier than He. However, despite this apparently large mass difference, the different plot are actually very similar as the gas varies. In general, we observe that, as the mass increases, the different curves are slightly shifted to the right; that is, the same value of γ is reached for bigger values of δ if the mass is bigger, or equivalently, for the same value of δ the TPD exponent is bigger if the mass is bigger. Actually, this trend is not clearly visible for He, Ne and N_2 (Fig. 3.31), if not even the opposite behaviour is present, while for

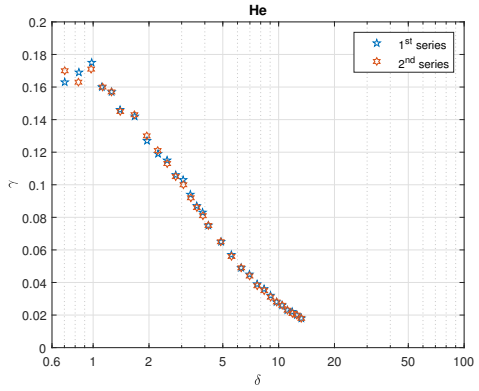

(a) Helium.

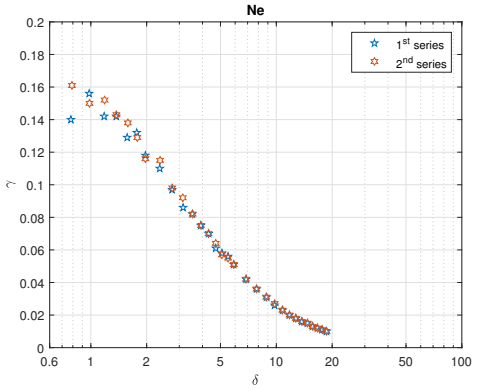

(b) Neon.

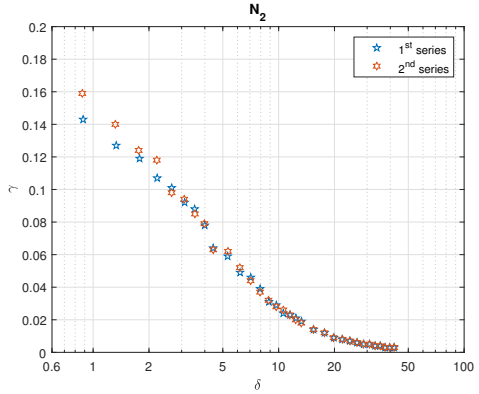

(c) Nitrogen.

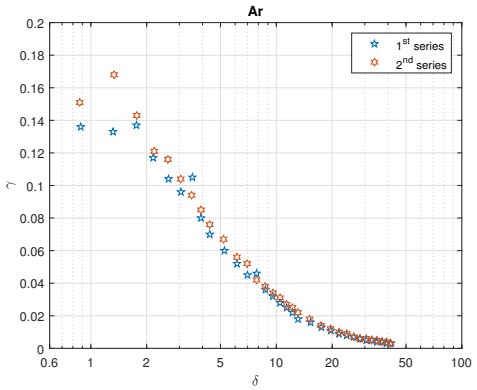

(d) Argon.

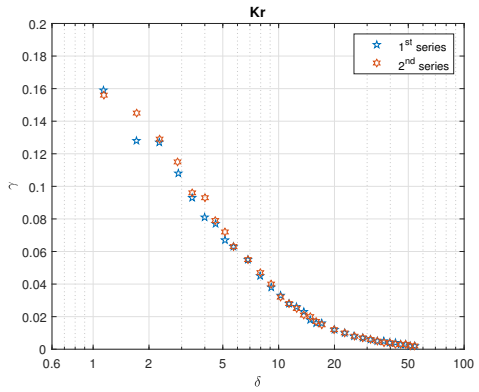

(e) Krypton.

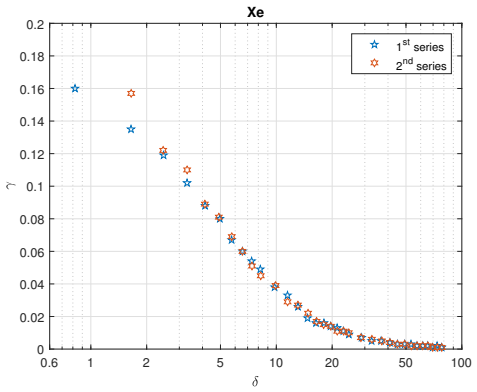

(f) Xenon.

Figure 3.29.: Experimental TPD exponent: overlapping of the two experimental series for each gas.

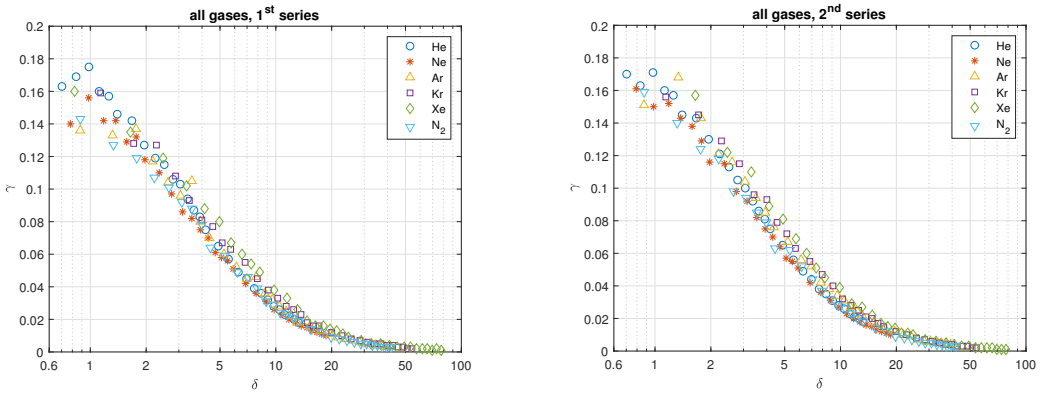

(a) 1^{st} series. (b) 2^{nd} series.

Figure 3.30.: Experimental TPD exponent: overlapping of all gases for each of the two experimental series.

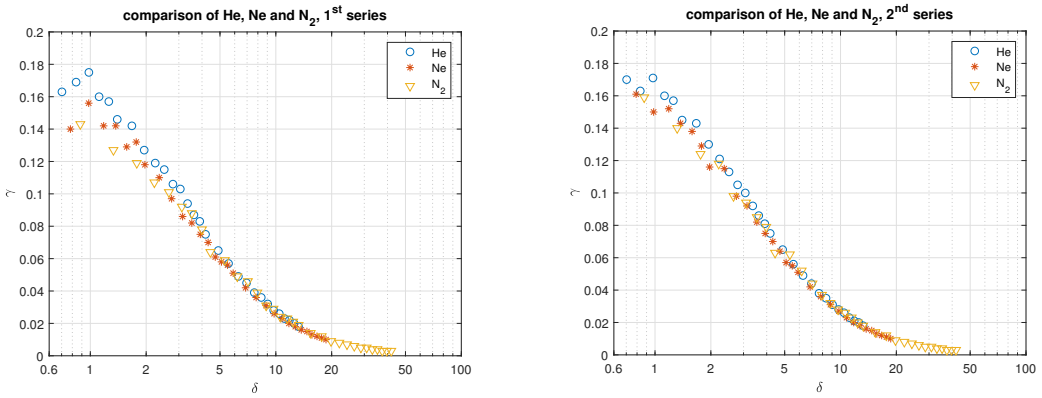

(a) 1^{st} series. (b) 2^{nd} series.

Figure 3.31.: Experimental TPD exponent: comparison between the TPD exponent of the three lighter gases.

Ar, Kr and Xe the shift is small but visible (Fig. 3.32).

3.5.2.2. The thermal slip coefficients

In Table 3.8 the experimental measurements of the thermal slip coefficients for the different gases (except nitrogen) are reported (given in [75]). Qualitatively, we can observe that the (absolute value of) the second-order coefficient increases with the molecular mass, while almost the same is true for the first-order coefficient, apart for the anomaly of Ne, whose coefficient is slightly smaller than the one of He.

3.6. Assessment of the accommodation coefficients

In this section we commit ourselves to the assessment of the accommodation coefficients starting from the experimental results presented in the previous section. Obviously, note that the ACs, in general, will be different from gas to gas.

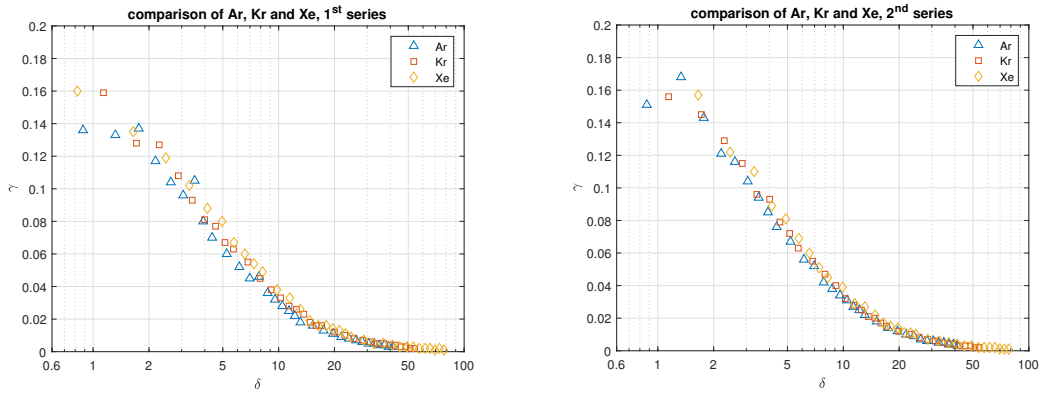

(a) 1^{st} series.

(b) 2^{nd} series.

Figure 3.32.: Experimental TPD exponent: comparison between the TPD exponent of the three heavier gases.

Gas	$A_{1\,\mathrm{exp}}^{T}$	$A_{2\,\mathrm{exp}}^{T}$
He	1.006 ± 0.020	-1.147 ± 0.113
Ne	0.998 ± 0.029	-1.226 ± 0.172
Ar	1.017 ± 0.057	-1.274 ± 0.406
Kr	1.061 ± 0.053	-1.327 ± 0.400
Xe	1.102 ± 0.085	-1.746 ± 0.626

Table 3.8.: Experimental values of the thermal slip coefficients for the five noble gases (reported in [75]).

Practically, we will proceed as follows. We start from certain experimental data and try to reproduce them with the analytical expressions of the corresponding physical quantity presented in Section 3.2: the right ACs are the ones which, inserted in these analytical expression, allow the best approximation of the experimental data. We finally validate the results using the assessed ACs to compute other physical quantities from their analytical expression, comparing it with the corresponding experimental data.
Depending from the experimental data at our hand, this analysis can be performed essentially in two ways:

- we extract the accommodation coefficients from the thermal slip coefficients and validate the results comparing the data concerning the TPD exponent;
- we extract the ACs from the TPD exponent and validate the results comparing the data concerning the TSCs.

We shall follow both these paths and compare the results.

3.6.1. Assessment of the accommodation coefficients from the thermal slip coefficients

In this section we use our analytical expression of the thermal slip coefficients to reproduce the experimental results reported in Table 3.8 and consequently extract appropriate accommodation coefficients for every gas considered. The resulting ACs will be validated by comparing experimental and analytical data about the TPD exponent.

3.6.1.1. Extraction of the accommodation coefficients

What we have to face now is basically an optimization problem of a particular kind: the aim is to find for each gas the α_t and α_n in order to obtain the best fit between the experimental data and our analytical expression of the slip coefficients.
The implementation of this optimization procedure in MATLAB® is quite intuitive: it is sufficient to nest two `for` loops to span the whole domain of both the accommodation coefficients, compute in the inner loop the thermal slip coefficients from their analytical expression for the fixed values of α_t and α_n, compute the value of the (relative) error between the experimental values and the analytical ones related to these particular αs storing it, e.g., in a matrix, and, once outside the outer loop, find the minimum and finally recover the corresponding αs. The results of this procedure are reported in Table 3.9. The agreement between the analytical outputs obtained via variational techniques and the experimental data looks quite good for each of the gases considered, but some comments are in order.

With a more careful analysis of the error, we find that the pairs of ACs which guarantees relative errors similar to the ones reported in Table 3.9 spread along a stripe that spans almost all the values of α_n and about half of the domain of α_t (see Fig. 3.33): this means that *a priori* a pair of ACs which gives an error very close to the optimal one may be very different from the optimal pair, so the procedure described above may look intrinsically unstable. Actually, this is why the validation *a posteriori* is needed. In particular, we observe that the ACs for Xe are likely to be far from the correct ones, being at the boundary of their domain of validity, especially regarding α_t. Indeed, the physical meaning of $\alpha_t = 2$ is that all the molecules of that gas are

Gas	α_t	α_n	$A_{1\,\mathrm{exp}}^T$	$A_{2\,\mathrm{exp}}^T$	A_1^T	A_2^T	Δ_{max} (%)
He	0.80	0.08	1.006 ± 0.020	-1.147 ± 0.113	1.0429	-1.1067	3.7
Ne	0.79	0.26	0.998 ± 0.029	-1.226 ± 0.172	1.0536	-1.1615	5.6
Ar	0.77	0.45	1.017 ± 0.057	-1.274 ± 0.406	1.0644	-1.2174	4.7
Kr	0.87	0.36	1.061 ± 0.053	-1.327 ± 0.400	1.0807	-1.3028	1.9
Xe	2	0.93	1.102 ± 0.085	-1.746 ± 0.626	1.1382	-1.6938	3.3

Table 3.9.: ACs extracted from the error-minimizing fitting of the TSCs through their analytical expressions; also the TSCs are reported, both the experimental ones and the ones obtained via analytical expressions with the corresponding ACs. The last column is the maximum relative discrepancy between experimental and analytical TSCs.

Gas	α_t	α_n	$A_{1\,\mathrm{exp}}^T$	$A_{2\,\mathrm{exp}}^T$	A_1^T	A_2^T	Δ_{max} (%)
He	0.80	0.15	1.006 ± 0.020	-1.147 ± 0.113	1.0481	-1.1334	4.2
Ne	0.80	0.25	0.998 ± 0.029	-1.226 ± 0.172	1.0556	-1.1718	5.7
Ar	0.83	0.28	1.017 ± 0.057	-1.274 ± 0.406	1.0659	-1.2255	4.8
Kr	0.88	0.33	1.061 ± 0.053	-1.327 ± 0.400	1.0817	-1.3083	1.9
Xe	1.16	0.35	1.102 ± 0.085	-1.746 ± 0.626	1.1509	-1.6881	4.4

Table 3.10.: ACs reported in [28] with corresponding experimental and analytical values of the TSCs and their maximum relative discrepancy.

back-scattered by the gas surface interaction, which seems very unlikely to be actually true. For this reason, for what concerns Xe, we choose to refer to the ACs tuned in [28], which turned out to be appropriate to fit the dimensionless mass flow rate for the thermal creep problem. These values, for all the noble gases, are reported in Table 3.10. Finally, we note that, apart from Xe, the values of α_t and α_n in Tables 3.9 and 3.10 are quite similar for the same gas, in particular α_t, and give rise to similar errors.

3.6.1.2. Validation of the results: comparison of the TPD data

We now try to validate the results obtained previously: in particular, we use the accommodation coefficients reported in Table 3.9 ("first table") and Table 3.10 ("second table") to compute the TPD exponent for all the gases, in order to compare these values with corresponding experimental results.

Helium The comparison is shown in Fig. 3.34a. The agreement between analytical and experimental data is acceptable: the qualitative behaviour is captured by the analytical values, but the experimental data are slightly overestimated. The two different choices of the accommodation coefficients lead to two practically identical γ: this is not surprising, since the α_t are the same and the α_n are quite similar, and we know that γ is very weakly dependent on α_n, especially when α_t is close to 1. Both the choices lead to an error in fitting γ of about 11% at $\delta = 4.18$ (the error is computed as defined in Eq. (3.73), in the next section).

Neon The comparison is shown in Fig. 3.34b. The considerations are the same as in the case of He: the qualitative behaviour is correct, but the experimental data are

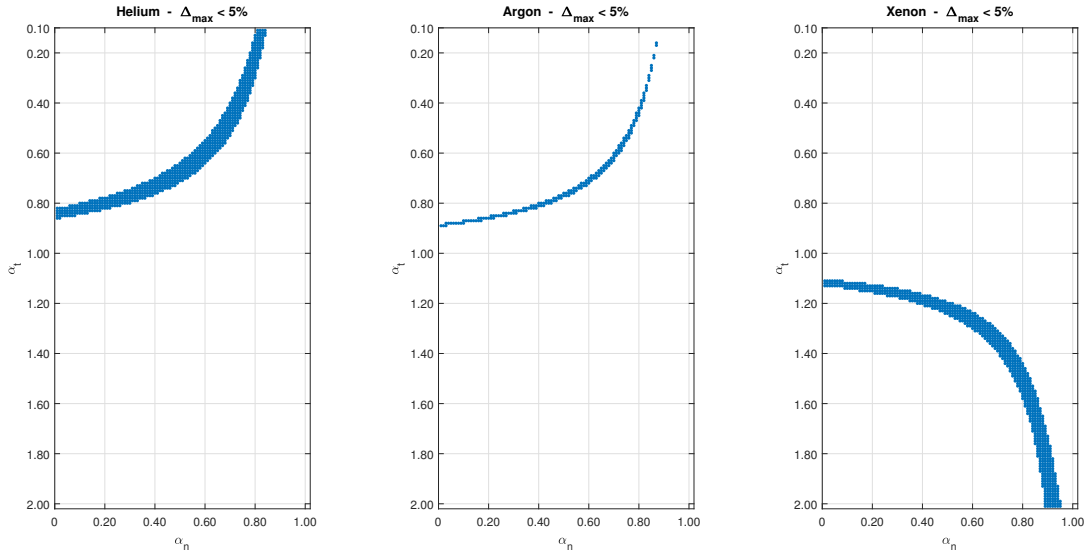

Figure 3.33.: Samples of the (relative) fitting error for the TSCs of He, Ar and Xe for all the possible pairs of ACs: the blue dots indicate the pairs (α_t,α_n) for which the discrepancy between analytical and experimental values is less than 5%. We observe the particular distribution of the pairs of ACs with low fitting error: in particular, they can have very different values of both α_t and α_n.

overestimated, and more evidently than in the previous case. The two choices of α_t and α_n lead to practically the same γ, with a fitting error of about 20% in $\delta = 3.144$.

Argon The comparison is shown in Fig. 3.35a. The fitting of the experimental data through analytical ones is very good. The two different α_t used are quite similar, and this reflects in similar γ; as already seen in previous sections, the discrepancy becomes more evident for small δ.

Krypton The comparison is shown in Section 3.6.1.2. The quantitative agreement between the two datasets is quite good. In this case, both the accommodation coefficients are practically the same, and the two analytical γ overlap.

Xenon The comparison is shown in Fig. 3.36. We can clearly see that the accommodation coefficients obtained with the optimization procedure introduced at the beginning of this section are totally inadequate to describe the behaviour of the TPD exponent for Xe, especially for small δ, as we may have expected. For what concerns the second choice of α_t and α_n, we have a good agreement for $\delta > 10$, but for smaller δ experimental data are again overestimated, with a local error comparable with the one in the case of Ne.

The fitting error for Ar, Kr and Xe is not reported because it is neither meaningful nor reliable: in all three cases, the largest discrepancy appear at big δ, where the values of γ are rather small, so experimental error, sensitivity of the instruments and statistical fluctuations play an important role. Actually, we highlight that the global fitting error for these gases is always achieved in correspondence of a δ for which the two

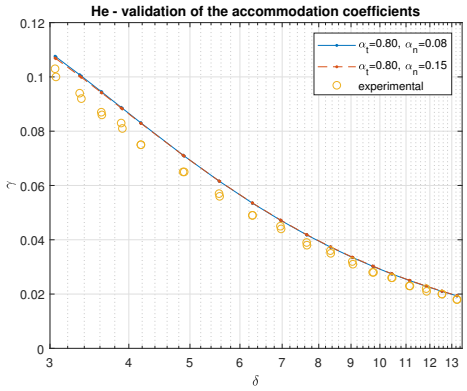

(a) He.

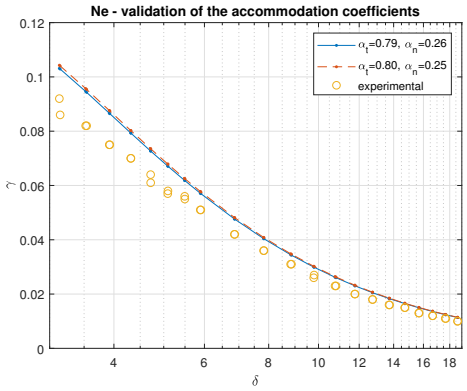

(b) Ne.

Figure 3.34.: He and Ne: validation of ACs extracted from experimental TSCs. Solid lines: first table; dashed lines: second table.

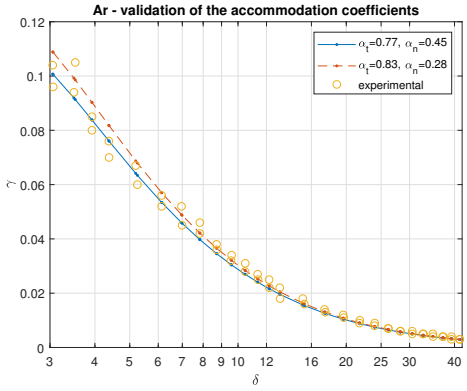

(a) Ar.

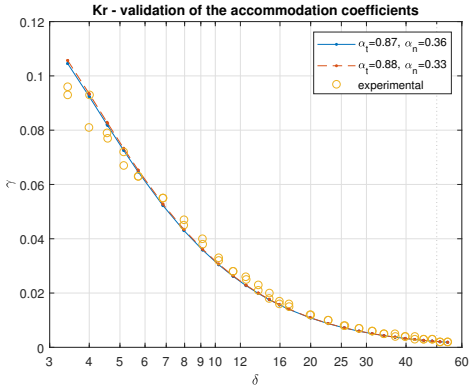

(b) Kr.

Figure 3.35.: Ar and Kr: validation of ACs extracted from experimental TSCs. Solid lines: first table; dashed lines: second table.

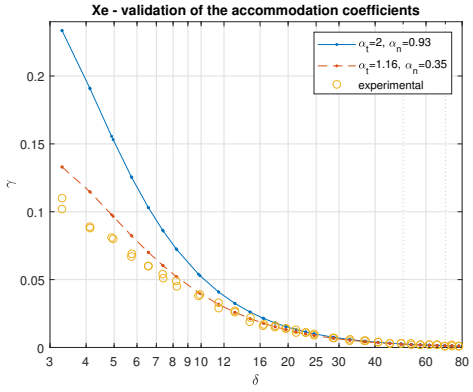

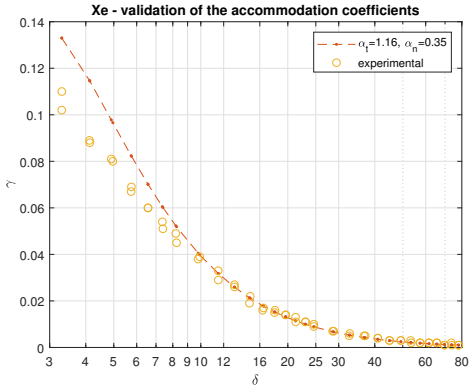

Figure 3.36.: Xe: validation of ACs extracted from experimental TSCs. Solid lines: first table; dashed lines: second table.

Gas	α_t	α_n
He	0.80	0.08
Ne	0.79	0.26
Ar	0.77	0.45
Kr	0.87	0.36
Xe	1.16	0.35

Table 3.11.: Accommodation coefficients assessed from the fitting of the thermal slip coefficients.

experimental series give very different values, one well-fitted and the other much further. This is a strong indication that we may be in presence of statistical fluctuations and/or experimental error, which are more dangerous if the value of the physical quantity to be measured is comparable with the amplitude of the fluctuation or with the sensitivity of the measure itself. This fact may suggest that a better way to compute the fitting error could be to consider only the fit for δ under a certain value, or at least to give to these δ more importance in the computation of the error. This problem will be faced in the next section.

3.6.1.3. Conclusions

After the validation, the accommodation coefficients are assessed, and are resumed in Table 3.11.

Despite its apparent intrinsic instability, the optimization procedure employed for the extraction of the ACs through the fitting of the thermal slip coefficients produced quite acceptable results in general. The different masses do not appear to play a main role for what concerns α_n, in the sense that the variation of this AC from gas to gas does not seem to be strongly related to the value of molecular masses (e.g., it is not monotonically increasing or decreasing as mass increases). Regarding α_t, it is practically the same for the two lighter gases, He and Ne, while for the three heavier gases, Ar, Kr and Xe, it strictly and sensibly increases as the molecular mass increases. This behaviour is very similar to the one of A_1^T, as observed in Section 3.5.2.2.
About the validation step, we can observe that:

- for He, Ne, Ar and Kr the optimization procedure of the TSCs turned out to be a useful technique to capture the qualitative behaviour of the TPD exponent, with also acceptable or even good quantitative matching, especially for Ar and Kr;
- for Xe, the plain optimization process leads to accommodation coefficients which are unable to reproduce the TPD exponent for $\delta < 15$, but even with a more careful choice the qualitative and quantitative match is good only above a certain regime of rarefaction. This may even give rise to some doubts about the suitability of such a model for the boundary conditions in the case of Xe.

3.6.2. Assessment of the accommodation coefficients from the TPD exponent

In this section we use our analytical expression of γ to reproduce the experimental results on the TPD exponent and consequently extract appropriate accommodation

coefficients for every gas considered. The resulting ACs will be validated by comparing experimental and analytical data about the slip coefficients.

3.6.2.1. Extraction of the accommodation coefficients

The optimization problem is practically the same as in the previous section: the aim is to find for each gas the α_t and α_n in order to obtain the best fit between the experimental data and our analytical expression of γ. However, there are some critical differences, and some important remarks are in order.
The first thing to notice is that we cannot hope to find a good fit in the whole experimental domain of δ, but in general we have to exclude *a priori* all the too small δ (at least $\delta < 3$, as already seen), since we know that they are out of the rigorous regime of validity of the model, assessed numerically in Section 3.4 and in [28]. The best we can do to consider also these data is to find the best fit between model and experimental data in the domain of validity of the model, and check only *a posteriori* the agreement between this best model and the experimental data also beyond the validity domain. This may be useful also to determine in a more precise way the actual domain of validity of the second-order slip model for Eq. (3.13) and Eq. (3.14).
The second issue is the definition of "best fit". The most intuitive way to proceed is to define an "error" as a function of the accommodation coefficients and the experimental data: for each gas, the couple (α_t, α_n) which minimizes this error is considered to be the most suitable choice to obtain the best fit. An appropriate definition of the error may be the following:

$$\mathrm{err}(\alpha_t, \alpha_n) = \max_{\delta} \frac{\gamma(\delta, \alpha_n, \alpha_t) - \gamma_{\mathrm{exp}}(\delta)}{\min\left\{\gamma(\delta, \alpha_n, \alpha_t), \gamma_{\mathrm{exp}}(\delta)\right\}}\,, \tag{3.73}$$

where γ is the well-known reference model for the TPD exponent, given by Eq. (3.19), γ_{exp} are the experimental data (which are given as a function of δ), and the denominator is needed in order to be allowed to call this quantity "relative error". Practically speaking, the idea is to find the α_t and α_n which minimizes the largest relative discrepancy between the reference model and the experimental data. We highlight again that this procedure has to be made separately for each gas, since the two accommodation coefficients which describe the gas-surface interaction may be different from gas to gas.
A slightly different definition of the error may be

$$\mathrm{err}'(\alpha_t, \alpha_n) = \max_{\delta} \frac{\gamma(\delta, \alpha_n, \alpha_t) - \gamma_{\mathrm{exp}}(\delta)}{\delta \min\left\{\gamma(\delta, \alpha_n, \alpha_t), \gamma_{\mathrm{exp}}(\delta)\right\}}\,, \tag{3.74}$$

where the δ at denominator is an attempt to weigh more the errors at small δ, since it may be reasonably more probable to find larger percent discrepancies with smaller values of the measured quantity γ, and therefore at bigger δ, due to the sensitivity and accuracy of the instruments: the smaller the measured value is, the more it becomes comparable to the amplitude of possible fluctuations and to the accuracy of the instrument itself. The effect of minimizing this quantity instead of the first one should be to obtain a better fit for smaller δ as it would be with the minimization of Eq. (3.73). This different choice of the quantity to be minimized makes sense also from a purely physical point of view: we know that the thermal creep, and consequently the TPD effect, is more important at higher degrees of rarefaction, therefore we may be reasonably more

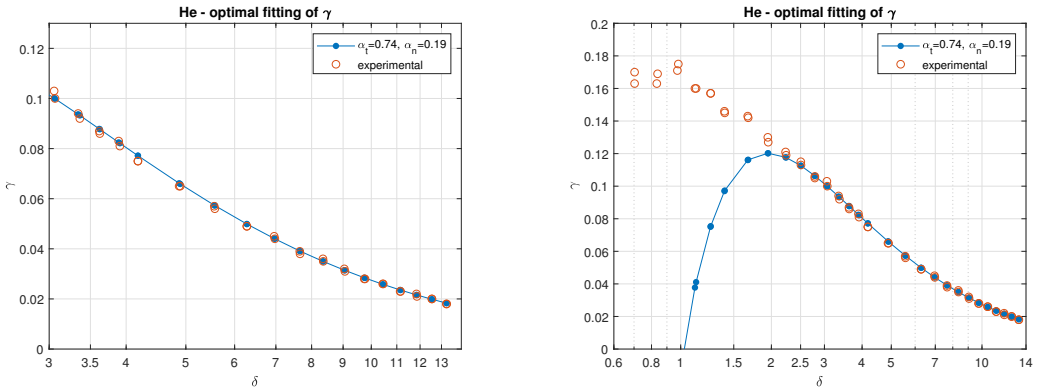

(a) Second-order slip regime.

(b) Whole experimental range.

Figure 3.37.: He: optimal fitting of the experimental TPD exponent.

interested in having a better fit in that domain of δ.
A final general remark on the choice of the best accommodation coefficients is that a bit of common sense from the human being is not inappropriate: for example, as already observed, even if the optimal choice, from a purely numerical point of view, is a very small or a very large AC, it may be physically inadequate and only due to some statistical fluctuation in the measurement, or to a not perfect choice of the definition of the "error" to be minimized. In general, therefore, our opinion is that it is important not to rely completely on some dumb automated numerical procedure, but also to look directly at the data. This problem appeared also in the previous section, regarding the accommodation coefficients for Xe extracted by a purely numerical minimization of the fitting error for the thermal slip coefficients.

The implementation of this optimization procedure in MATLAB® is similar to the one in the previous section: it is sufficient to nest two `for` loops to span the whole domain of both the accommodation coefficients, compute in the inner loop the reference γ on the experimental range of δ for the fixed values of α_t and α_n, compute the value of the above-mentioned error related to these particular αs storing it, e.g., in a matrix, and, once outside the outer loop, find the minimum and finally recover the corresponding αs.
We present now the results for every gas.

Helium The optimal accommodation coefficients for He, according to the minimization of the quantity Eq. (3.73), are

$$\alpha_t = 0.74 \quad \alpha_n = 0.19\,, \tag{3.75}$$

and the resulting plots are reported in Fig. 3.37. The maximum relative error is 2.9 % and is attained for $\delta = 4.180$, where $\gamma = 0.0772$ and $\gamma_{\text{exp}} = 0.075$.
The fit is therefore very good for $\delta \geq 3$, and the validity of the "extended" slip regime is confirmed.

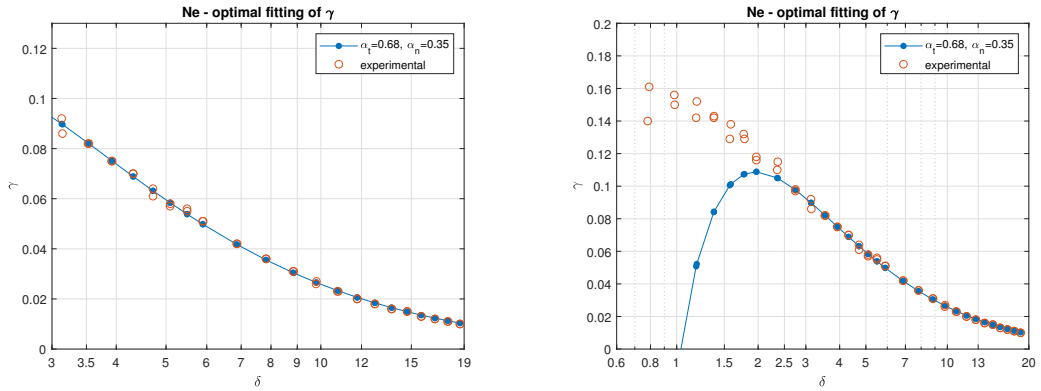

(a) Second-order slip regime.

(b) Whole experimental range.

Figure 3.38.: Ne: optimal fitting of the experimental TPD exponent.

Neon The optimal accommodation coefficients for Ne, according to the minimization of the quantity Eq. (3.73), are

$$\alpha_t = 0.68 \quad \alpha_n = 0.35\,, \tag{3.76}$$

and the resulting plots are reported in Fig. 3.38. The maximum relative error is 4.4 % and is attained for $\delta = 15.667$, where $\gamma = 0.0136$ and $\gamma_{\text{exp}} = 0.013$.
The considerations about the domain of validity of the model are the same as in the case of He.

Nitrogen The optimal accommodation coefficients for N_2, according to the minimization of the quantity Eq. (3.73), are

$$\alpha_t = 0.71 \quad \alpha_n = 0.35\,, \tag{3.77}$$

and the resulting plots are reported in Fig. 3.39. The maximum relative error is 11 % and is attained for $\delta = 37.460$, where $\gamma = 0.0033$ and $\gamma_{\text{exp}} = 0.003$.
The considerations on the validity domain are exactly the same as in the case of He and Ne.

Argon In the case of Ar, we perform the optimization considering both the minimization of Eq. (3.73) and Eq. (3.74).

The optimal accommodation coefficients according to the minimization of the quantity Eq. (3.73) are

$$\alpha_t = 0.85 \quad \alpha_n = 0.95\,. \tag{3.78}$$

The maximum relative error in this case is 18 % and is attained for $\delta = 13.097$, where $\gamma = 0.0213$ and $\gamma_{\text{exp}} = 0.018$.

The optimal ACs according to the minimization of the quantity Eq. (3.74) are

$$\alpha_t = 0.80 \quad \alpha_n = 0.37\,. \tag{3.79}$$

The maximum relative error in this case is 25 % and is attained for $\delta = 34.827$, where $\gamma = 0.0040$ and $\gamma_{\text{exp}} = 0.005$. Both the resulting plots are reported in Fig. 3.40.

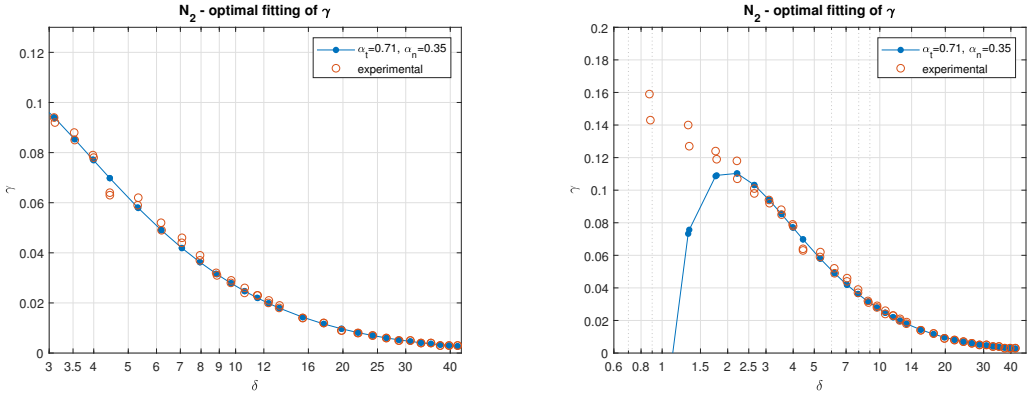

(a) Second-order slip regime.

(b) Whole experimental range.

Figure 3.39.: N_2: optimal fitting of the experimental TPD exponent.

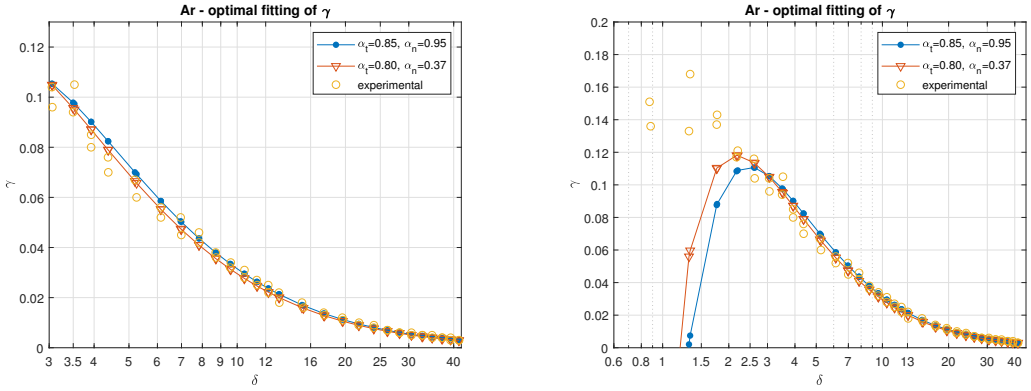

(a) Second-order slip regime.

(b) Whole experimental range.

Figure 3.40.: Ar: optimal fitting of the experimental TPD exponent.

For both models, the fit is quite good for $\delta \geq 3$, and the validity of "extended" slip model is confirmed also in this case. Moreover, for $\delta < 7$, both models apparently slightly overestimate the experimental results, but the agreement is a bit better for the second choice. They are practically equivalent for bigger δ. The result is that the second model looks overall better, for both the graphical fit and the ACs, which seem more reasonable and similar to the ones for lighter gases. Therefore, we choose to keep as final values for the ACs the second ones.

Krypton In the case of Kr, we perform the optimization considering both the minimization of Eq. (3.73) and Eq. (3.74).

The optimal accommodation coefficients according to the minimization of the quantity Eq. (3.73) are

$$\alpha_t = 1.01 \quad \alpha_n = 0.00\,. \tag{3.80}$$

The optimal ACs according to the minimization of the quantity Eq. (3.74) are

$$\alpha_t = 0.83 \quad \alpha_n = 0.95\,. \tag{3.81}$$

All the resulting plots are reported in Fig. 3.41.

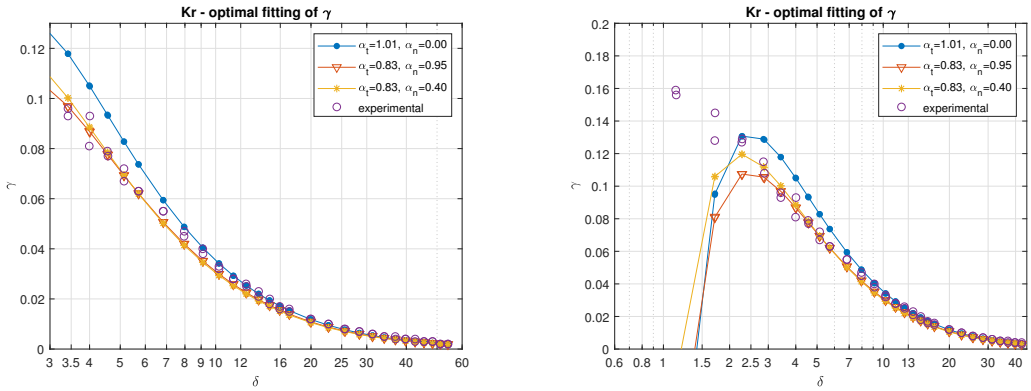

(a) Second-order slip regime.

(b) Whole experimental range.

Figure 3.41.: Kr: optimal fitting of the experimental TPD exponent.

For $\delta > 3$, the first model visibly overestimates the experimental data for $\delta < 7$, but the second one slightly underestimate data for $7 < \delta < 12$; they are practically equivalent for bigger δ. The result is that the overall fit is not bad, for both models, but the second one looks better.

At this point, we resort to some of the above-mentioned common sense, also in view of the rigorous considerations made in Sections 3.2.2.2 and 3.2.2.3. We note that both the values $\alpha_n = 0$ and $\alpha_n = 0.95$ are very different from the values of α_n previously assessed for other gases, and also a bit "strange", since they are close to the extremal values for α_n, 0 and 1 . Furthermore, we recall that the dependence of γ on α_n is quite weak for $\delta > 4$, especially if α_t is close to 1, as in this case. Therefore we choose to study the model with parameters

$$\alpha_t = 0.83 \quad \alpha_n = 0.40\,, \tag{3.82}$$

that is, α_t is unchanged from the second model, and α_n is almost the mean value between the other two.
As foreseen, this model is practically equivalent, for $\delta > 3$, to the second one, for both the graph and the maximum relative deviation, therefore the same considerations as before hold. What is quite different is what happens beyond $\delta = 3$: the extension of the third model, almost up to $\delta = 2$, looks better than the second one, and way better than the first one. Therefore, we choose to keep as final values for the ACs the third ones.

Xenon In the case of Xe, we perform the optimization considering both the minimization of Eq. (3.73) and Eq. (3.74).

The optimal accommodation coefficients according to the minimization of the quantity Eq. (3.73) are

$$\alpha_t = 1.51 \quad \alpha_n = 0.00\,. \tag{3.83}$$

The optimal ACs according to the minimization of the quantity Eq. (3.74) are

$$\alpha_t = 0.91 \quad \alpha_n = 1.00\,. \tag{3.84}$$

All the resulting plots are reported in Fig. 3.42.

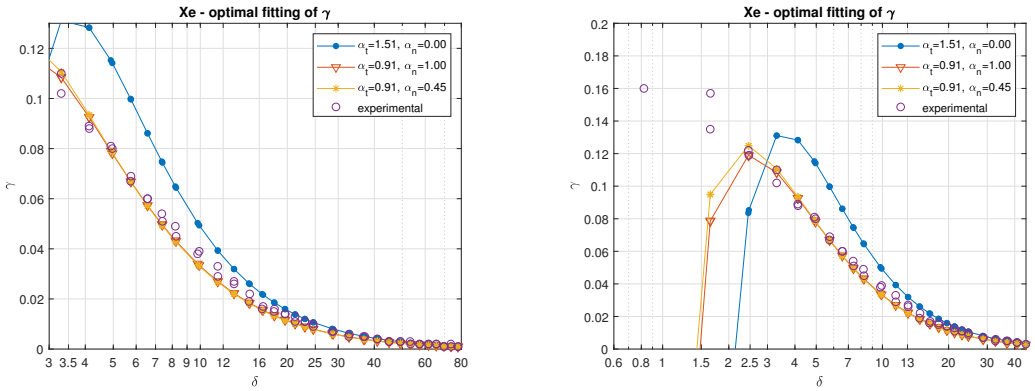

(a) Second-order slip regime.

(b) Whole experimental range.

Figure 3.42.: Xe: optimal fitting of the experimental TPD exponent.

Gas	α_t	α_n
He	0.74	0.19
Ne	0.68	0.35
N_2	0.71	0.35
Ar	0.80	0.37
Kr	0.83	0.40
Xe	0.91	0.45

Table 3.12.: Accommodation coefficients assessed from the fitting of the TPD exponent.

For $\delta > 3$, the first model visibly overestimates the experimental data for $\delta < 16$, but the second one slightly underestimate data for $7 < \delta < 14$; they are practically equivalent for $\delta > 25$. Moreover, the first model has a visible maximum for $3 < \delta < 3.5$, therefore its validity domain cannot reach $\delta = 3$.

Finally, repeating the same exact argumentations as in the case of Kr, we choose to study the model with parameters

$$\alpha_t = 0.91 \quad \alpha_n = 0.45\,, \tag{3.85}$$

that is, α_t is unchanged from the second model, and α_n is almost the mean value between the other two.
As foreseen, this model is practically equivalent to the second one for $\delta > 3$, for both the graph and the maximum relative deviation, therefore the same considerations as before hold. Furthermore, it seems slightly better than the second model for $\delta = 2.5$, while the first one, as already said, is inadequate for $\delta = 3$, and therefore also for δ smaller. Therefore, we choose to keep as final values for the ACs the third ones.

Observe that also in this case the relative discrepancy of Kr and Xe between analytical and experimental results is not reported, with the same exact considerations made at the end of Section 3.6.1.2.

We sum up all the extracted accommodation coefficients in Table 3.12.

Gas	$A_{1\,\mathrm{exp}}^{T}$	A_1^T (Eq. (3.17))	$\Delta_{\%}$
He	$1.006 \pm 0.020^{28,76}$	1.0329	2.7
Ne	$0.998 \pm 0.029^{28,76}$	1.0339	3.6
Ar	$1.017 \pm 0.057^{28,76}$	1.0646	4.7
Kr	$1.061 \pm 0.053^{28,76}$	1.0736	1.2
Xe	$1.102 \pm 0.085^{28,76}$	1.0933	0.79

Table 3.13.: First-order thermal slip coefficients: validation of ACs extracted from experimental TPD exponent.

Gas	$A_{2\,\mathrm{exp}}^{T}$	A_2^T (Eq. (3.18))	$\Delta_{\%}$
He	$-1.147 \pm 0.113^{28,76}$	-1.0563	7.9
Ne	$-1.226 \pm 0.172^{28,76}$	-1.0611	13
Ar	$-1.274 \pm 0.406^{28,76}$	-1.2185	4.4
Kr	$-1.327 \pm 0.400^{28,76}$	-1.2656	4.6
Xe	$-1.746 \pm 0.626^{28,76}$	-1.3702	22

Table 3.14.: Second-order thermal slip coefficients: validation of ACs extracted from experimental TPD exponent.

3.6.2.2. Validation of the results: computation of the thermal slip coefficients

We now try to validate the results obtained previously: in particular, we use the accommodation coefficients reported in Table 3.12 to compute first- and second-order thermal slip coefficients for all the gases, in order to compare these values with corresponding experimental results. The comparison is reported in Table 3.13 and Table 3.14.
We observe that:

- the results about the first-order TSC are very good in all the cases considered;
- the relative error in the computation of the second-order TSC is in general worse than for the first-order one, but still acceptable, apart from the cases of Ne (for which the relative error was the highest one also in the extraction of α_t and α_n directly from the TSCs, see Tables 3.9 and 3.10) and Xe (for which, again, this model of the gas-surface interaction does not seem to be the best one).

3.6.2.3. Conclusions

The optimization procedure for the three lighter gases (including N_2) was plain and always the same, and lead to similar results in all three cases (similar numerical values of α_t and relative deviations, similar qualitative considerations). The different masses do not appear to play a main role, in the sense that the variation of the accommodation coefficients from gas to gas does not seem to be strongly related to the value of molecular masses (e.g., they are not monotonically increasing or decreasing as mass increases).
For the three heavier gases, the procedure was more involved than the lighter ones: we had to change slightly the formulation of the optimization problem (in particular, the quantity to be minimized), and for Kr and Xe we also had to adjust a coefficient

Gas	via slip coefficients		via TPD exponent	
	α_t	α_n	α_t	α_n
He	0.80	0.08	0.74	0.19
Ne	0.79	0.26	0.68	0.35
Ar	0.77	0.45	0.80	0.37
Kr	0.87	0.36	0.83	0.40
Xe	1.16	0.35	0.91	0.45

Table 3.15.: Accommodation coefficients assessed from the fitting of the thermal slip coefficients (first two columns) and of the TPD exponent (second two columns).

"manually", in order to obtain more appealing results. The mass, conversely, seems to be related to the variation of α_t, which increases as the mass increases. The same consideration cannot be made for α_n, which in all these cases is pretty "artificial".
About the optimization procedure used to extract the accommodation coefficients from TPD data, we observe that for Ar and Kr the solutions that it produces look unstable in the coefficient α_n with respect to the "norm" chosen to minimize the error: with different "norms", i.e. Eq. (3.73) and Eq. (3.74), the resulting α_n are pretty different. This may be due to the fact that in these two cases both norms gives an α_t quite similar and close to 1, and γ itself is weakly dependent on α_n in this situation. For the Xe case, also α_t changes quite a lot if the norm varies: this is another indication that, as observed in previous section, this model of the boundary conditions may be inappropriate to describe the behaviour of this gas.

3.6.3. Comparison of the two assessment procedures

The accommodation coefficients obtained in the two different ways presented in previous sections are resumed and compared in Table 3.15.

Apart from Xe, we observe a fairly good agreement for what concerns α_t for all gases, and in the cases of Ar and Kr also α_n has an acceptable match (even though we remember that α_n in the case of Kr is somewhat artificial). However, in general, the agreement is better for α_t rather than α_n, and this may be an indication of some sort of instabilities in the extraction of α_n, probably due to a weaker dependence of the physical quantities on this AC, as happens in the case of the TPD exponent.
It is interesting to notice that, in extracting the ACs from the TSCs and consequently trying to reproduce the TPD exponent through the boundary conditions assessed in this way, we are actually reproducing a phenomenon which involves both pressure- and thermal-driven flows, that is, the TPD effect, from the knowledge of quantities which involves only thermal-driven flows, that is, the TSCs. Therefore, we should be able to reproduce results concerning pressure-driven flows, such as the viscous slip coefficients: this may actually be an important benchmark for a further and more precise validation of the ACs.
We remain skeptical about the case of Xe, for which the agreement between the two assessed α_t is not very good, and for which both the validation steps were not so satisfactory (ACs which guarantee a good fit for the TSCs do not entail a good reproduction of the TPD effect, and viceversa).

4. Binary gas mixtures: thermal creep and thermomolecular pressure difference

In this chapter we address the second main topic of this thesis:
we deal with the concept of TPD effect in the case of gaseous mixtures and outline a path that can be followed to study this particular phenomenon when more than one gas is present. Note that, even if the generalization to the case of three or more gases could be straightforward, at least conceptually, from the practical point of view we shall consider only binary mixtures.

4.1. General considerations about gaseous mixtures

In many practical problems, one is dealing not with pure gases but with gas mixtures. A wide range of applications include scientific and industrial processes: there are many gas mixtures used in clinical and medical practice, in the food industry and in manufacturing (see [77] for more details). Moreover, thanks to the technological progress, the challenge has become that of integrating into a simple micro-sized system, operations that commonly solicit a whole laboratory: as already seen in Chapter 1, microfluidic devices exploit the physical and chemical properties of liquids and gases at the microscale, offering several benefits over conventionally sized systems. For these reasons, internal flows of rarefied gaseous mixtures caused by pressure, temperature and density (or concentration) gradients are of major importance in several applications in physics and engineering. Despite this fact, compared to the huge amount of work done for the case of a single gas, the available literature for the case of gas mixtures is not extensive. In particular, we are not aware of previous works that try to deal in a systematic way, either theoretically (or numerically) or even experimentally, with the study of the TPD effect in a quantitative way, through the TPD exponent.

4.1.1. TPD effect and TPD exponent

All the considerations made in Section 2.3.2 hold unchanged if more than one gas is present: hence, the qualitative description of the TPD effect is exactly the same in the case of gas mixtures. The second step is the definition of the TPD exponent. To this aim, an idea may be to move from the single-gas case, starting from Eq. (2.70):

$$\gamma = \frac{G_T}{G_P} \,. \tag{4.1}$$

In Section 2.3.2.2, this formula was derived rigorously for the case of single gas, and a basic starting approach for mixtures could be to take it as a definition. We shall adopt this point of view in the following.

Nonetheless, some problems may arise. For example, a significant question is: what actually *are* G_P and G_T in this case? In the framework of single-gas flow, they were the kinetic coefficients of the mass flux, that is, the coefficients of the linear combination that allows to write the dimensionless mass flux in terms of the dimensionless gradients of pressure and temperature respectively. Trivially, they can be seen as the mass fluxes due to a pressure and a temperature gradient separately (thanks to the linearization) and represent the Poiseuille flow and the thermal creep flow, respectively. The point is that now we have two different gases, so we can further split these fluxes into two more contributions due exactly to these gases. Eventually, we realize that we can define the TPD exponent in two ways:

- defining a global coefficient as the ratio between the mass fluxes due to the temperature and pressure gradients without splitting them in the two single-gas contributions;
- defining a coefficient for each gas involved as the ratio between the thermal creep and Poiseuille mass fluxes due to that specific gas.

Both definitions seem to have advantages and disadvantages and may be complementary: with the first definition, we sketch the behaviour of the mixture as a whole, while with the second one we try to extract the contribution of the single gas to the phenomenon.

Concerning mixtures, a last remark is in order. In this case, there is another way to induce a mass flux, apart from pressure (Poiseuille flow) and temperature (thermal creep flow) gradients: the **diffusion flow**, induced by a **concentration gradient**, which does not occur in single-component gases. We do not consider it even in this case because, via linearization, if the gradients are sufficiently small, we can distinguish each contribution and consider them separately, limiting our attention to fluxes caused by pressure and temperature differences only.

4.2. The thermal creep problem for a binary mixture

Let us consider a binary gaseous mixture confined between two flat, infinite and parallel plates located at $x = -d/2$ and $x = d/2$. A temperature gradient is imposed at the boundaries. We assume that the mixture flows parallel to the plates, in the z direction, due to this gradient, which is taken to be small. Under these conditions, following for example[37, 78], the Boltzmann equation can be linearized about local Maxwellian distributions by putting

$$f_s(x, z, \boldsymbol{\xi}) = f_{s,0}\left[1 + \left(\lambda_s \xi^2 - \frac{5}{2}\right)\tau z + h_s(x, \boldsymbol{\xi})\right] \quad s = 1, 2 \tag{4.2}$$

where

$$f_{s,0} = n_{s,0}\left(\frac{\lambda_s}{\pi}\right)^{3/2} \exp\left(-\lambda_s \xi^2\right), \quad \lambda_s = m_s/(2k_B T_0)\,. \tag{4.3}$$

Here, k_B is the Boltzmann constant, m_s and $n_{s,0}$ are the mass and the equilibrium number density of the s-th species, x is the spatial variable in the transverse, or cross-channel, direction, z is the spatial variable in the longitudinal direction, $\boldsymbol{\xi}$ is the molecular velocity, and T_0 is a reference temperature. $s = 1$ shall always denote the lighter

gas species.
Finally, $|h_s| \ll 1$ is the small perturbation with respect to the equilibrium state, and $\tau = \frac{1}{T}\frac{\partial T}{\partial z}$ is the small and constant temperature gradient which drives the flow. Then, the perturbations h_s satisfy the system of coupled Boltzmann equations

$$\xi_x \frac{\partial h_s}{\partial x} + \xi_z \left(\lambda_s \xi^2 - \frac{5}{2}\right)\tau = Lh^{(s)}{}_{MC} \quad s = 1, 2 \tag{4.4}$$

where $Lh^{(s)}{}_{MC}$ is the linearized collision operator modelled with the McCormack model, introduced in Eqs. (2.33) and (2.34) (we shall omit the subscript $_{MC}$ in the following). We introduce the dimensionless quantities

$$M_{12} = \frac{m_1}{m_2} \quad \mu_{12} = \frac{m_1 m_2}{m_1 + m_2} \quad \mathbf{c} = \sqrt{\lambda_1}\boldsymbol{\xi} = \mathbf{c}^1 \quad \mathbf{c}^2 = \frac{\mathbf{c}}{\sqrt{M_{12}}}\,. \tag{4.5}$$

Moreover, we define the characteristic times

$$\theta_s = \frac{1}{\gamma_s} \tag{4.6}$$

where γ_s is the same as in Eqs. (2.33) and (2.34), and

$$\Theta_{12} = \frac{\theta_1}{\theta_2} = \frac{\gamma_2}{\gamma_1} \tag{4.7}$$

is the macroscopic collision frequency ratio.
Therefore we can define consistently the dimensionless lengths

$$\tilde{x} = \frac{x}{\theta_1/\sqrt{\lambda_1}} \quad \tilde{z} = \frac{z}{\theta_1/\sqrt{\lambda_1}} \quad \delta = \frac{d}{\theta_1/\sqrt{\lambda_1}}\,. \tag{4.8}$$

δ is the dimensionless distance between the channel walls as well as the rarefaction parameter (inverse Knudsen number) of the species $s = 1$.
Finally we define the dimensionless constant temperature gradient as

$$\hat{\tau} = \frac{1}{T}\frac{\partial T}{\partial \tilde{z}}\,; \tag{4.9}$$

therefore

$$\hat{\tau} = \frac{1}{T}\frac{\partial T}{\partial \tilde{z}} = \frac{1}{T}\frac{\partial T}{\partial z}\frac{\theta_1}{\sqrt{\lambda_1}} = \tau\frac{\theta_1}{\sqrt{\lambda_1}}\,. \tag{4.10}$$

We proceed now with the adimensionalization of the equations, substituting Eqs. (4.5), (4.8) and (4.10) in Eq. (4.4):

$$\begin{aligned} &\frac{c_x}{\sqrt{\lambda_1}}\frac{\partial h_1}{\partial \tilde{x}}\frac{\sqrt{\lambda_1}}{\theta_1} + \frac{c_z}{\sqrt{\lambda_1}}\left(\lambda_1\frac{c^2}{\lambda_1} - \frac{5}{2}\right)\hat{\tau}\frac{\sqrt{\lambda_1}}{\theta_1} = Lh^{(1)} \\ &\qquad\qquad \Rightarrow \qquad c_x\frac{\partial h_1}{\partial \tilde{x}} + c_z\left(c^2 - \frac{5}{2}\right)\hat{\tau} = \theta_1 Lh^{(1)} \end{aligned} \tag{4.11}$$

$$\frac{c_x}{\sqrt{\lambda_1}}\frac{\partial h_2}{\partial \tilde{x}}\frac{\sqrt{\lambda_1}}{\theta_1} + \frac{c_z}{\sqrt{\lambda_1}}\left(\lambda_2\frac{c^2}{\lambda_1} - \frac{5}{2}\right)\hat{\tau}\frac{\sqrt{\lambda_1}}{\theta_1} = Lh^{(2)}$$

$$\Rightarrow \qquad c_x\frac{\partial h_2}{\partial\tilde{x}}+c_z\left(\frac{c^2}{M_{12}}-\frac{5}{2}\right)\hat{\tau}=\theta_1 L h^{(2)} \quad (4.12)$$

Substituting explicitly Eqs. (2.33) and (2.34) and Eqs. (4.6) and (4.7):

$$\begin{aligned}
c_x\frac{\partial h_1}{\partial\tilde{x}}+c_z\left(c^2-\frac{5}{2}\right)\hat{\tau}+h_1 &= \rho^{(1)}+2\left(1-\eta_{1,2}^{(1)}\right)\mathbf{c}\cdot\mathbf{v}^{(1)}-2\eta_{1,2}^{(2)}\mathbf{c}\cdot\mathbf{q}^{(1)}\\
&\quad+\left[1-\frac{2\eta_{1,2}^{(1)}M_{12}}{1+M_{12}}\right]\left(c^2-\frac{3}{2}\right)\tau^{(1)}\\
&\quad+2\left(1+\eta_{1,1}^{(4)}-\eta_{1,1}^{(3)}-\eta_{1,2}^{(3)}\right)c_ic_j\tilde{P}_{ij}^{(1)}+\frac{8}{5}\left(1+\eta_{1,1}^{(6)}-\eta_{1,1}^{(5)}-\eta_{1,2}^{(5)}\right)\left(c^2-\frac{5}{2}\right)\mathbf{c}\cdot\mathbf{q}^{(1)}\\
&\quad-\eta_{1,2}^{(2)}\left(c^2-\frac{5}{2}\right)\mathbf{c}\cdot\mathbf{v}^{(1)}+2\eta_{1,2}^{(1)}\mathbf{c}\cdot\mathbf{v}^{(2)}+2M_{12}\eta_{1,2}^{(2)}\mathbf{c}\cdot\mathbf{q}^{(2)}+\eta_{1,2}^{(2)}\left(c^2-\frac{5}{2}\right)\mathbf{c}\cdot\mathbf{v}^{(2)}\\
&\quad+\frac{2\eta_{1,2}^{(1)}M_{12}}{1+M_{12}}\left(c^2-\frac{3}{2}\right)\tau^{(2)}+\frac{2\eta_{1,2}^{(4)}}{M_{12}}c_ic_j\tilde{P}_{ij}^{(2)}+\frac{8\eta_{1,2}^{(6)}}{5\sqrt{M_{12}}}\left(c^2-\frac{5}{2}\right)\mathbf{c}\cdot\mathbf{q}^{(2)} \quad (4.13)
\end{aligned}$$

$$\begin{aligned}
c_x\frac{\partial h_2}{\partial\tilde{x}}+c_z\left(\frac{c^2}{M_{12}}-\frac{5}{2}\right)\hat{\tau} &= \Theta_{12}\left\{\rho^{(2)}+\frac{2}{M_{12}}\left(1-\eta_{2,1}^{(1)}\right)\mathbf{c}\cdot\mathbf{v}^{(2)}-\frac{2\eta_{2,1}^{(2)}}{M_{12}}\mathbf{c}\cdot\mathbf{q}^{(2)}\right.\\
&\quad+\left[1-\frac{2\eta_{2,1}^{(1)}}{1+M_{12}}\right]\left(\frac{c^2}{M_{12}}-\frac{3}{2}\right)\tau^{(2)}\\
&\quad+\frac{2}{{M_{12}}^2}\left(1+\eta_{2,2}^{(4)}-\eta_{2,2}^{(3)}-\eta_{2,1}^{(3)}\right)c_ic_j\tilde{P}_{ij}^{(2)}+\frac{8}{5M_{12}}\left(1+\eta_{2,2}^{(6)}-\eta_{2,2}^{(5)}-\eta_{2,1}^{(5)}\right)\left(\frac{c^2}{M_{12}}-\frac{5}{2}\right)\mathbf{c}\cdot\mathbf{q}^{(2)}\\
&\quad-\frac{\eta_{2,1}^{(2)}}{M_{12}}\left(\frac{c^2}{M_{12}}-\frac{5}{2}\right)\mathbf{c}\cdot\mathbf{v}^{(2)}+\frac{2\eta_{2,1}^{(1)}}{M_{12}}\mathbf{c}\cdot\mathbf{v}^{(1)}+\frac{2\eta_{2,1}^{(2)}}{{M_{12}}^2}\mathbf{c}\cdot\mathbf{q}^{(1)}+\frac{\eta_{2,1}^{(2)}}{M_{12}}\left(\frac{c^2}{M_{12}}-\frac{5}{2}\right)\mathbf{c}\cdot\mathbf{v}^{(1)}\\
&\quad\left.+\frac{2\eta_{2,1}^{(1)}}{1+M_{12}}\left(\frac{c^2}{M_{12}}-\frac{3}{2}\right)\tau^{(1)}+\frac{2\eta_{2,1}^{(4)}}{M_{12}}c_ic_j\tilde{P}_{ij}^{(1)}+\frac{8\eta_{2,1}^{(6)}}{5\sqrt{M_{12}}}\left(\frac{c^2}{M_{12}}-\frac{5}{2}\right)\mathbf{c}\cdot\mathbf{q}^{(1)}\right\}-\Theta_{12}h_2
\end{aligned} \quad (4.14)$$

where the definitions of the macroscopic quantities $\eta_{i,j}^{(s)}$, $\rho^{(s)}$, $\mathbf{v}^{(s)}$, $\tau^{(s)}$, $\tilde{P}_{ij}^{(s)}$, $\mathbf{q}^{(s)}$, are the same as in Section 2.2.2.2.

Without any computation, we can immediately observe that, due to the symmetry of the problem, the macroscopic quantities $v_y^{(s)}$, $q_y^{(s)}$, $\tilde{P}_{xy}^{(s)}$, $\tilde{P}_{yz}^{(s)}$, $s=1,2$, are zero. The resulting equations are

$$\begin{aligned}
c_x\frac{\partial h_1}{\partial\tilde{x}}+c_z\left(c^2-\frac{5}{2}\right)\hat{\tau}+h_1 &= \rho^{(1)}+2\left(1-\eta_{1,2}^{(1)}\right)c_xv_x^{(1)}+2\left(1-\eta_{1,2}^{(1)}\right)c_zv_z^{(1)}\\
&\quad-2\eta_{1,2}^{(2)}c_xq_x^{(1)}-2\eta_{1,2}^{(2)}c_zq_z^{(1)}+\left[1-\frac{2\eta_{1,2}^{(1)}M_{12}}{1+M_{12}}\right]\left(c^2-\frac{3}{2}\right)\tau^{(1)}\\
&\quad+2\left(1+\eta_{1,1}^{(4)}-\eta_{1,1}^{(3)}-\eta_{1,2}^{(3)}\right)c_x^2\tilde{P}_{xx}^{(1)}+2\left(1+\eta_{1,1}^{(4)}-\eta_{1,1}^{(3)}-\eta_{1,2}^{(3)}\right)c_y^2\tilde{P}_{yy}^{(1)}\\
&\quad+2\left(1+\eta_{1,1}^{(4)}-\eta_{1,1}^{(3)}-\eta_{1,2}^{(3)}\right)c_z^2\tilde{P}_{zz}^{(1)}+2\left(1+\eta_{1,1}^{(4)}-\eta_{1,1}^{(3)}-\eta_{1,2}^{(3)}\right)c_xc_z\tilde{P}_{xz}^{(1)}
\end{aligned}$$

$$
\begin{aligned}
&+\frac{8}{5}\left(1+\eta_{1,1}^{(6)}-\eta_{1,1}^{(5)}-\eta_{1,2}^{(5)}\right)\left(c^2-\frac{5}{2}\right)c_x q_x^{(1)}\\
&+\frac{8}{5}\left(1+\eta_{1,1}^{(6)}-\eta_{1,1}^{(5)}-\eta_{1,2}^{(5)}\right)\left(c^2-\frac{5}{2}\right)c_z q_z^{(1)}\\
&-\eta_{1,2}^{(2)}\left(c^2-\frac{5}{2}\right)c_x v_x^{(1)}-\eta_{1,2}^{(2)}\left(c^2-\frac{5}{2}\right)c_z v_z^{(1)}+2\eta_{1,2}^{(1)}c_x v_x^{(2)}+2\eta_{1,2}^{(1)}c_z v_z^{(2)}\\
&+2M_{12}\eta_{1,2}^{(2)}c_x q_x^{(2)}+2M_{12}\eta_{1,2}^{(2)}c_z q_z^{(2)}+\eta_{1,2}^{(2)}\left(c^2-\frac{5}{2}\right)c_x v_x^{(2)}+\eta_{1,2}^{(2)}\left(c^2-\frac{5}{2}\right)c_z v_z^{(2)}\\
&+\frac{2\eta_{1,2}^{(1)}M_{12}}{1+M_{12}}\left(c^2-\frac{3}{2}\right)\tau^{(2)}+\frac{2\eta_{1,2}^{(4)}}{M_{12}}c_x^2\tilde{P}_{xx}^{(2)}+\frac{2\eta_{1,2}^{(4)}}{M_{12}}c_y^2\tilde{P}_{yy}^{(2)}+\frac{2\eta_{1,2}^{(4)}}{M_{12}}c_z^2\tilde{P}_{zz}^{(2)}+\frac{2\eta_{1,2}^{(4)}}{M_{12}}c_x c_z\tilde{P}_{xz}^{(2)}\\
&+\frac{8\eta_{1,2}^{(6)}}{5\sqrt{M_{12}}}\left(c^2-\frac{5}{2}\right)c_x q_x^{(2)}+\frac{8\eta_{1,2}^{(6)}}{5\sqrt{M_{12}}}\left(c^2-\frac{5}{2}\right)c_z q_z^{(2)} \qquad (4.15)
\end{aligned}
$$

$$
\begin{aligned}
c_x\frac{\partial h_2}{\partial\tilde{x}}+c_z\left(\frac{c^2}{M_{12}}-\frac{5}{2}\right)\hat{\tau}+\Theta_{12}h_2 &= \Theta_{12}\left\{\rho^{(2)}+\frac{2}{M_{12}}\left(1-\eta_{2,1}^{(1)}\right)c_x v_x^{(2)}+\frac{2}{M_{12}}\left(1-\eta_{2,1}^{(1)}\right)c_z v_z^{(2)}\right.\\
&-\frac{2\eta_{2,1}^{(2)}}{M_{12}}c_x q_x^{(2)}-\frac{2\eta_{2,1}^{(2)}}{M_{12}}c_z q_z^{(2)}+\left[1-\frac{2\eta_{2,1}^{(1)}}{1+M_{12}}\right]\left(\frac{c^2}{M_{12}}-\frac{3}{2}\right)\tau^{(2)}\\
&+\frac{2}{{M_{12}}^2}\left(1+\eta_{2,2}^{(4)}-\eta_{2,2}^{(3)}-\eta_{2,1}^{(3)}\right)c_x^2\tilde{P}_{xx}^{(2)}\\
&+\frac{2}{{M_{12}}^2}\left(1+\eta_{2,2}^{(4)}-\eta_{2,2}^{(3)}-\eta_{2,1}^{(3)}\right)c_y^2\tilde{P}_{yy}^{(2)}+\frac{2}{{M_{12}}^2}\left(1+\eta_{2,2}^{(4)}-\eta_{2,2}^{(3)}-\eta_{2,1}^{(3)}\right)c_z^2\tilde{P}_{zz}^{(2)}\\
&+\frac{2}{{M_{12}}^2}\left(1+\eta_{2,2}^{(4)}-\eta_{2,2}^{(3)}-\eta_{2,1}^{(3)}\right)c_x c_z\tilde{P}_{xz}^{(2)}+\frac{8}{5M_{12}}\left(1+\eta_{2,2}^{(6)}-\eta_{2,2}^{(5)}-\eta_{2,1}^{(5)}\right)\left(\frac{c^2}{M_{12}}-\frac{5}{2}\right)c_x q_x^{(2)}\\
&+\frac{8}{5M_{12}}\left(1+\eta_{2,2}^{(6)}-\eta_{2,2}^{(5)}-\eta_{2,1}^{(5)}\right)\left(\frac{c^2}{M_{12}}-\frac{5}{2}\right)c_z q_z^{(2)}\\
&-\frac{\eta_{2,1}^{(2)}}{M_{12}}\left(\frac{c^2}{M_{12}}-\frac{5}{2}\right)c_x v_x^{(2)}-\frac{\eta_{2,1}^{(2)}}{M_{12}}\left(\frac{c^2}{M_{12}}-\frac{5}{2}\right)c_z v_z^{(2)}+\frac{2\eta_{2,1}^{(1)}}{M_{12}}c_x v_x^{(1)}+\frac{2\eta_{2,1}^{(1)}}{M_{12}}c_z v_z^{(1)}+\frac{2\eta_{2,1}^{(2)}}{{M_{12}}^2}c_x q_x^{(1)}\\
&+\frac{2\eta_{2,1}^{(2)}}{{M_{12}}^2}c_z q_z^{(1)}+\frac{\eta_{2,1}^{(2)}}{M_{12}}\left(\frac{c^2}{M_{12}}-\frac{5}{2}\right)c_x v_x^{(1)}+\frac{\eta_{2,1}^{(2)}}{M_{12}}\left(\frac{c^2}{M_{12}}-\frac{5}{2}\right)c_z v_z^{(1)}\\
&+\frac{2\eta_{2,1}^{(1)}}{1+M_{12}}\left(\frac{c^2}{M_{12}}-\frac{3}{2}\right)\tau^{(1)}+\frac{2\eta_{2,1}^{(4)}}{M_{12}}c_x^2\tilde{P}_{xx}^{(1)}+\frac{2\eta_{2,1}^{(4)}}{M_{12}}c_y^2\tilde{P}_{yy}^{(1)}+\frac{2\eta_{2,1}^{(4)}}{M_{12}}c_z^2\tilde{P}_{zz}^{(1)}+\frac{2\eta_{2,1}^{(4)}}{M_{12}}c_x c_z\tilde{P}_{xz}^{(1)}\\
&\left.+\frac{8\eta_{2,1}^{(6)}}{5\sqrt{M_{12}}}\left(\frac{c^2}{M_{12}}-\frac{5}{2}\right)c_x q_x^{(1)}+\frac{8\eta_{2,1}^{(6)}}{5\sqrt{M_{12}}}\left(\frac{c^2}{M_{12}}-\frac{5}{2}\right)c_z q_z^{(1)}\right\} \qquad (4.16)
\end{aligned}
$$

4.2.1. Projection procedure for the thermal creep problem

Since the problem under consideration is one-dimensional in space, the unknown perturbed distribution functions h_s, as well as the overall quantities, depend only on the x coordinate. Likewise, we can reduce the dimensionality of the molecular-velocity space by the **projection procedure**, presented for example in [37] and [78].

4.2.1.1. Projection for $s = 1$

First, we multiply Eq. (4.15) by $\frac{1}{\pi} c_z e^{-\left(c_y^2+c_z^2\right)}$ and we integrate over $dc_y dc_z$, defining the reduced unknown distribution function

$$Z^{(1)}(x, c_x) = \frac{1}{\pi} \int_{-\infty}^{+\infty} \int_{-\infty}^{+\infty} h_1(x, \mathbf{c}) c_z e^{-\left(c_y^2+c_z^2\right)} dc_y dc_z \,. \tag{4.17}$$

In order to compute these integrals, it may be useful to observe that the macroscopic quantities do not depend on $\mathbf{c}$ and that

$$\int_{-\infty}^{+\infty} x^{2n} e^{-x^2} dx = \frac{(2n)!}{2^{2n} n!} \sqrt{\pi} \,.$$

The resulting equation is

$$\begin{aligned} c_x \frac{\partial Z^{(1)}}{\partial \tilde{x}} + Z^{(1)} + \frac{1}{2}\left(c_x^2 - \frac{1}{2}\right)\hat{\tau} &= \left(1 - \eta_{1,2}^{(1)}\right) v_z^{(1)} - \eta_{1,2}^{(2)} q_z^{(1)} + \left(1 + \eta_{1,1}^{(4)} - \eta_{1,1}^{(3)} - \eta_{1,2}^{(3)}\right) c_x \tilde{P}_{xz}^{(1)} \\ &+ \frac{4}{5}\left(1 + \eta_{1,1}^{(6)} - \eta_{1,1}^{(5)} - \eta_{1,2}^{(5)}\right)\left(c_x^2 - \frac{1}{2}\right) q_z^{(1)} - \frac{1}{2}\eta_{1,2}^{(2)}\left(c_x^2 - \frac{1}{2}\right) v_z^{(1)} + \eta_{1,2}^{(1)} v_z^{(2)} \\ &+ M_{12}\eta_{1,2}^{(2)} q_z^{(2)} + \frac{1}{2}\eta_{1,2}^{(2)}\left(c_x^2 - \frac{1}{2}\right) v_z^{(2)} + \frac{\eta_{1,2}^{(4)}}{M_{12}} c_x \tilde{P}_{xz}^{(2)} + \frac{4\eta_{1,2}^{(6)}}{5\sqrt{M_{12}}}\left(c_x^2 - \frac{1}{2}\right) q_z^{(2)} \end{aligned} \tag{4.18}$$

Then, we multiply Eq. (4.15) by $\frac{1}{\pi}\left(c_y^2 + c_z^2 - 2\right) c_z e^{-\left(c_y^2+c_z^2\right)}$ and we integrate over $dc_y dc_z$, defining the reduced unknown distribution function

$$Y^{(1)}(x, c_x) = \frac{1}{\pi} \int_{-\infty}^{+\infty} \int_{-\infty}^{+\infty} h_1(x, \mathbf{c}) c_z \left(c_y^2 + c_z^2 - 2\right) e^{-\left(c_y^2+c_z^2\right)} dc_y dc_z \,. \tag{4.19}$$

The resulting equation is

$$c_x \frac{\partial Y^{(1)}}{\partial \tilde{x}} + Y^{(1)} + \hat{\tau} = -\eta_{1,2}^{(2)} v_z^{(1)} + \frac{8}{5}\left(1 + \eta_{1,1}^{(6)} - \eta_{1,1}^{(5)} - \eta_{1,2}^{(5)}\right) q_z^{(1)} + \eta_{1,2}^{(2)} v_z^{(2)} + \frac{8\eta_{1,2}^{(6)}}{5\sqrt{M_{12}}} q_z^{(2)} \tag{4.20}$$

The macroscopic fields appearing on the right-hand side of these equations can be written as

$$v_z^{(1)}(x) = \frac{1}{\sqrt{\pi}} \int_{-\infty}^{+\infty} Z^{(1)} e^{-c_x^2} dc_x \tag{4.21}$$

$$q_z^{(1)}(x) = \frac{1}{2\sqrt{\pi}} \int_{-\infty}^{+\infty} \left[\left(c_x^2 - \frac{1}{2}\right) Z^{(1)} + Y^{(1)}\right] e^{-c_x^2} dc_x \tag{4.22}$$

$$\tilde{P}_{xz}^{(1)}(x) = \frac{1}{\sqrt{\pi}} \int_{-\infty}^{+\infty} c_x Z^{(1)} e^{-c_x^2} dc_x \tag{4.23}$$

4.2.1.2. Projection for $s = 2$

First, we multiply Eq. (4.16) by $\frac{1}{\pi M_{12}} \frac{c_z}{\sqrt{M_{12}}} e^{-\frac{\left(c_y^2+c_z^2\right)}{M_{12}}}$ and we integrate over $dc_y dc_z$, defining the reduced unknown distribution function

$$Z^{(2)}(x, c_x) = \frac{1}{\pi {M_{12}}^{3/2}} \int_{-\infty}^{+\infty} \int_{-\infty}^{+\infty} h_2(x, \mathbf{c}) c_z e^{-\frac{\left(c_y^2+c_z^2\right)}{M_{12}}} dc_y dc_z \,. \tag{4.24}$$

The resulting equation is

$$c_x\frac{\partial Z^{(2)}}{\partial\tilde{x}}+\Theta_{12}Z^{(2)}+\frac{\sqrt{M_{12}}}{2}\left(\frac{c_x^2}{M_{12}}-\frac{1}{2}\right)\hat{\tau}=\Theta_{12}\left\{\frac{1}{\sqrt{M_{12}}}\left(1-\eta_{2,1}^{(1)}\right)v_z^{(2)}-\frac{1}{\sqrt{M_{12}}}\eta_{2,1}^{(2)}q_z^{(2)}\right.$$
$$+\frac{1}{{M_{12}}^{3/2}}\left(1+\eta_{2,2}^{(4)}-\eta_{2,2}^{(3)}-\eta_{2,1}^{(3)}\right)c_x\tilde{P}_{xz}^{(2)}$$
$$+\frac{4}{5\sqrt{M_{12}}}\left(1+\eta_{2,2}^{(6)}-\eta_{2,2}^{(5)}-\eta_{2,1}^{(5)}\right)\left(\frac{c_x^2}{M_{12}}-\frac{1}{2}\right)q_z^{(2)}-\frac{\eta_{2,1}^{(2)}}{2\sqrt{M_{12}}}\left(\frac{c_x^2}{M_{12}}-\frac{1}{2}\right)v_z^{(2)}+\frac{\eta_{2,1}^{(1)}}{\sqrt{M_{12}}}v_z^{(1)}$$
$$\left.+\frac{\eta_{2,1}^{(2)}}{{M_{12}}^{3/2}}q_z^{(1)}+\frac{\eta_{2,1}^{(2)}}{2\sqrt{M_{12}}}\left(\frac{c_x^2}{M_{12}}-\frac{1}{2}\right)v_z^{(1)}+\frac{\eta_{2,1}^{(4)}}{\sqrt{M_{12}}}c_x\tilde{P}_{xz}^{(1)}+\frac{4\eta_{2,1}^{(6)}}{5}\left(\frac{c_x^2}{M_{12}}-\frac{1}{2}\right)q_z^{(1)}\right\} \tag{4.25}$$

Then, we multiply Eq. (4.16) by $\frac{1}{\pi M_{12}}\left(\frac{c_y^2+c_z^2}{M_{12}}-2\right)\frac{c_z}{\sqrt{M_{12}}}e^{-\frac{\left(c_y^2+c_z^2\right)}{M_{12}}}$ and we integrate over dc_ydc_z, defining the reduced unknown distribution function

$$Y^{(2)}(x,c_x)=\frac{1}{\pi{M_{12}}^{3/2}}\int_{-\infty}^{+\infty}\int_{-\infty}^{+\infty}h_2(x,\mathbf{c})c_z\left(\frac{c_y^2+c_z^2}{M_{12}}-2\right)e^{-\frac{\left(c_y^2+c_z^2\right)}{M_{12}}}dc_ydc_z\,. \tag{4.26}$$

The resulting equation is

$$c_x\frac{\partial Y^{(2)}}{\partial\tilde{x}}+\Theta_{12}Y^{(2)}+\sqrt{M_{12}}\hat{\tau}=\Theta_{12}\left\{-\frac{\eta_{2,1}^{(2)}}{\sqrt{M_{12}}}v_z^{(2)}+\frac{8}{5\sqrt{M_{12}}}\left(1+\eta_{2,2}^{(6)}-\eta_{2,2}^{(5)}-\eta_{2,1}^{(5)}\right)q_z^{(2)}\right.$$
$$\left.+\frac{\eta_{2,1}^{(2)}}{\sqrt{M_{12}}}v_z^{(1)}+\frac{8\eta_{2,1}^{(6)}}{5}q_z^{(1)}\right\} \tag{4.27}$$

The macroscopic fields appearing on the right-hand side of these equations can be written as

$$v_z^{(2)}(x)=\frac{1}{\sqrt{\pi}}\int_{-\infty}^{+\infty}Z^{(2)}e^{-c_x^2/M_{12}}dc_x \tag{4.28}$$
$$q_z^{(2)}(x)=\frac{1}{2\sqrt{\pi}}\int_{-\infty}^{+\infty}\left[\left(\frac{c_x^2}{M_{12}}-\frac{1}{2}\right)Z^{(2)}+Y^{(2)}\right]e^{-c_x^2/M_{12}}dc_x \tag{4.29}$$
$$\tilde{P}_{xz}^{(2)}(x)=\frac{1}{\sqrt{\pi}}\int_{-\infty}^{+\infty}c_xZ^{(2)}e^{-c_x^2/M_{12}}dc_x \tag{4.30}$$

4.3. The coupled Poiseuille and thermal creep problems

In order to consider also the Poiseuille problem, whose equations are available in [37] and are obtained with the same projection procedure described above, it is sufficient to add to the left-hand side the corresponding source term; the resulting equations are:

$$c_x\frac{\partial Z^{(1)}}{\partial\tilde{x}}+Z^{(1)}+\frac{1}{2}\left(c_x^2-\frac{1}{2}\right)\hat{\tau}+\hat{k}=\left(1-\eta_{1,2}^{(1)}\right)v_z^{(1)}-\eta_{1,2}^{(2)}q_z^{(1)}+\left(1+\eta_{1,1}^{(4)}-\eta_{1,1}^{(3)}-\eta_{1,2}^{(3)}\right)c_x\tilde{P}_{xz}^{(1)}$$

$$+\frac{4}{5}\left(1+\eta_{1,1}^{(6)}-\eta_{1,1}^{(5)}-\eta_{1,2}^{(5)}\right)\left(c_x^2-\frac{1}{2}\right)q_z^{(1)}-\frac{1}{2}\eta_{1,2}^{(2)}\left(c_x^2-\frac{1}{2}\right)v_z^{(1)}+\eta_{1,2}^{(1)}v_z^{(2)}$$
$$+M_{12}\eta_{1,2}^{(2)}q_z^{(2)}+\frac{1}{2}\eta_{1,2}^{(2)}\left(c_x^2-\frac{1}{2}\right)v_z^{(2)}+\frac{\eta_{1,2}^{(4)}}{M_{12}}c_x\tilde{P}_{xz}^{(2)}+\frac{4\eta_{1,2}^{(6)}}{5\sqrt{M_{12}}}\left(c_x^2-\frac{1}{2}\right)q_z^{(2)} \quad (4.31)$$

$$c_x\frac{\partial Z^{(2)}}{\partial\tilde{x}}+\Theta_{12}Z^{(2)}+\frac{\sqrt{M_{12}}}{2}\left(\frac{c_x^2}{M_{12}}-\frac{1}{2}\right)\hat{\tau}+\sqrt{M_{12}}\hat{k}=\Theta_{12}\left\{\frac{1}{\sqrt{M_{12}}}\left(1-\eta_{2,1}^{(1)}\right)v_z^{(2)}-\frac{1}{\sqrt{M_{12}}}\eta_{2,1}^{(2)}q_z^{(2)}\right.$$
$$+\frac{1}{{M_{12}}^{3/2}}\left(1+\eta_{2,2}^{(4)}-\eta_{2,2}^{(3)}-\eta_{2,1}^{(3)}\right)c_x\tilde{P}_{xz}^{(2)}$$
$$+\frac{4}{5\sqrt{M_{12}}}\left(1+\eta_{2,2}^{(6)}-\eta_{2,2}^{(5)}-\eta_{2,1}^{(5)}\right)\left(\frac{c_x^2}{M_{12}}-\frac{1}{2}\right)q_z^{(2)}-\frac{\eta_{2,1}^{(2)}}{2\sqrt{M_{12}}}\left(\frac{c_x^2}{M_{12}}-\frac{1}{2}\right)v_z^{(2)}+\frac{\eta_{2,1}^{(1)}}{\sqrt{M_{12}}}v_z^{(1)}$$
$$\left.+\frac{\eta_{2,1}^{(2)}}{{M_{12}}^{3/2}}q_z^{(1)}+\frac{\eta_{2,1}^{(2)}}{2\sqrt{M_{12}}}\left(\frac{c_x^2}{M_{12}}-\frac{1}{2}\right)v_z^{(1)}+\frac{\eta_{2,1}^{(4)}}{\sqrt{M_{12}}}c_x\tilde{P}_{xz}^{(1)}+\frac{4\eta_{2,1}^{(6)}}{5}\left(\frac{c_x^2}{M_{12}}-\frac{1}{2}\right)q_z^{(1)}\right\} \quad (4.32)$$

$$c_x\frac{\partial Y^{(1)}}{\partial\tilde{x}}+Y^{(1)}+\hat{\tau}=-\eta_{1,2}^{(2)}v_z^{(1)}+\frac{8}{5}\left(1+\eta_{1,1}^{(6)}-\eta_{1,1}^{(5)}-\eta_{1,2}^{(5)}\right)q_z^{(1)}+\eta_{1,2}^{(2)}v_z^{(2)}+\frac{8\eta_{1,2}^{(6)}}{5\sqrt{M_{12}}}q_z^{(2)} \quad (4.33)$$

$$c_x\frac{\partial Y^{(2)}}{\partial\tilde{x}}+\Theta_{12}Y^{(2)}+\sqrt{M_{12}}\hat{\tau}=\Theta_{12}\left\{-\frac{\eta_{2,1}^{(2)}}{\sqrt{M_{12}}}v_z^{(2)}+\frac{8}{5\sqrt{M_{12}}}\left(1+\eta_{2,2}^{(6)}-\eta_{2,2}^{(5)}-\eta_{2,1}^{(5)}\right)q_z^{(2)}\right.$$
$$\left.+\frac{\eta_{2,1}^{(2)}}{\sqrt{M_{12}}}v_z^{(1)}+\frac{8\eta_{2,1}^{(6)}}{5}q_z^{(1)}\right\} \quad (4.34)$$

where $\hat{k}=\dfrac{1}{p}\dfrac{\partial p}{\partial\tilde{z}}$ is the small and constant dimensionless pressure gradient. The definitions of the unknown distribution functions and of the macroscopic quantities are the same as before.
Therefore, the complete set of equations governing the Poiseuille-thermal creep problem is given by Eqs. (4.31) to (4.34). As before, it is a system of four *coupled integro-differential equations* in the four unknown functions $Z^{(1)}$, $Y^{(1)}$, $Z^{(2)}$, $Y^{(2)}$.

Finally, we define the reduced mass and heat flow rates as

$$G_i^{(s)}=-\frac{1}{\delta^2}\int_{-\delta/2}^{\delta/2}v_{z,i}^{(s)}(x)dx \quad (4.35)$$

and

$$Q_i^{(s)}=-\frac{1}{\delta^2}\int_{-\delta/2}^{\delta/2}q_{z,i}^{(s)}(x)dx \quad (4.36)$$

where $s=1,2$ represents the gas species and $i=P,T$ indicates to which effect (pressure or temperature gradient) that physical quantity is due (e.g.: $Q_T^{(1)}$ is the heat flow rate of species 1 due to the temperature gradient).

4.3.1. Boundary conditions

Due to the much greater complexity of the governing equations of this problem with respect to the single-component case, the most used model for the boundary conditions is the Maxwell model; the two accommodation coefficients are denoted by α_s, $s = 1, 2$, and need not be the same. In terms of the perturbed distribution functions h_s, the model is written as ([78])

$$\begin{cases} h_s\left(-\frac{\delta}{2}, c_x, c_y, c_z\right) = (1-\alpha_s) h_s\left(-\frac{\delta}{2}, -c_x, c_y, c_z\right) + \alpha_s \mathcal{I}\left\{h_s\right\}\left(-\frac{\delta}{2}\right) \\ h_s\left(\frac{\delta}{2}, -c_x, c_y, c_z\right) = (1-\alpha_s) h_s\left(\frac{\delta}{2}, c_x, c_y, c_z\right) + \alpha_s \mathcal{I}\left\{h_s\right\}\left(\frac{\delta}{2}\right) \end{cases} \tag{4.37}$$

for $c_x > 0$ and all c_y, c_z. The diffuse term is

$$\mathcal{I}\left\{h_s\right\}(x) = \frac{2}{\pi} \int_{-\infty}^{\infty} \int_{-\infty}^{\infty} \int_{0}^{\infty} e^{-c^2} c_x h_s(x, -c_x, c_y, c_z) dc_x dc_y dc_z \,. \tag{4.38}$$

In terms of the reduced distribution functions we have

$$\begin{cases} Z^{(s)}\left(-\frac{\delta}{2}, c_x\right) = (1-\alpha_s) Z^{(s)}\left(-\frac{\delta}{2}, -c_x\right) \\ Z^{(s)}\left(\frac{\delta}{2}, -c_x\right) = (1-\alpha_s) Z^{(s)}\left(\frac{\delta}{2}, c_x\right) \\ Y^{(s)}\left(-\frac{\delta}{2}, c_x\right) = (1-\alpha_s) Y^{(s)}\left(-\frac{\delta}{2}, -c_x\right) \\ Y^{(s)}\left(\frac{\delta}{2}, -c_x\right) = (1-\alpha_s) Y^{(s)}\left(\frac{\delta}{2}, c_x\right) \end{cases} \tag{4.39}$$

In Section 4.4 we shall consider almost only the case of diffuse reflection, for which $\alpha_1 = \alpha_2 = 1$.

4.3.2. Definition of the TPD exponent in the case of a binary gas mixture

Following what we said in Section 4.1.1, we will consider two different definitions for the TPD exponent: the **"single-gas" definition**,

$$\gamma_s = \frac{G_T^{(s)}}{G_P^{(s)}} \,, \tag{4.40}$$

and the **"global" definition**,

$$\gamma_{\text{global}} = \frac{C_0 G_T^{(1)} + (1-C_0) G_T^{(2)}}{C_0 G_P^{(1)} + (1-C_0) G_P^{(2)}} \,, \tag{4.41}$$

where $C_0 = \dfrac{n_{1,0}}{n_{1,0} + n_{2,0}}$ is the equilibrium molar concentration. In the global definition, in order to consider correctly the contributions of both gases to the total mass flux, we weight each term by the molar concentration of the corresponding gas.
Note that ([79, 80])

$$\Lambda_{Pi} = C_0 G_i^{(1)} + (1-C_0) G_i^{(2)} \quad i = P, T \tag{4.42}$$

are the kinetic coefficients representing the mass fluxes caused by gradients of pressure and temperature, respectively. Hence, we can actually rewrite Eq. (4.41) as

$$\gamma_{\text{global}} = \frac{\Lambda_{PT}}{\Lambda_{PP}} \,. \tag{4.43}$$

4.4. Numerical behaviour of the TPD exponent

In general, there are several aspects to be considered in the analysis of the behaviour of a mixture, and this holds for the particular case of the TPD effect. This analysis can be more easily performed by changing, one by one, different physical parameters of the problem under study, such as:

- molecular masses and diameters, in order to simulate the behaviour of combinations of different gases;
- relative molar concentrations;
- intermolecular potential, in order to deduce how the behaviour of the mixture changes by using different models of molecular interaction.

For example, by changing some of the above-mentioned parameters, it is possible to obtain the limit of single gas: by letting the relative concentration C_0 go to 0 or to 1, or by choosing equal the molecular masses and diameters. It may be useful to compare the actual behaviour of the single gas with these limits of the binary mixture: indeed, we expect them to be the same.
Another feature of γ is its behaviour in the limit cases $\delta \to 0$ and $\delta \to \infty$, for which, in the single-gas case, we have $\gamma \to 0.5$ and $\gamma \to 0$ respectively (for diffuse boundary conditions). We expect these conditions to be verified also in the mixture case: at very low densities, the gas-gas interaction does not play a relevant role, and therefore the behaviour of the mixture is likely similar to the single-gas case; on the other hand, the thermal creep phenomenon is a peculiar feature of rarefied flows, and therefore, as all the cross effects, it vanishes in the hydrodynamic regime. For this same reason, we expect a strictly decreasing γ also in the mixture case (see Section 2.3.2).
A general remark about the influence on the numerical results of the mathematical model used in the study of the physical problem is the following. The choice of a particular model for the boundary conditions does not necessarily entail a loss of generality in a merely qualitative analysis. Indeed, we expect that a possible discrepancy of the functional dependence of γ on δ in the mixture case with respect to, for example, the single-gas case will appear for every choice of the boundary conditions, since this difference would probably be due to the gas-gas interaction, rather than to the gas-surface one. In this regard, what should have a much more relevant effect in the behaviour of the TPD exponent for a mixture is the model of the gas-gas interaction, rather than the boundary conditions. Therefore, it may be useful to compare the results obtained not only with different intermolecular potentials, but also with different models of the whole collision integral.

The approach to the numerical analysis of the TPD exponent in this chapter is completely different from the one adopted for the single-gas case: in Chapter 3 we exploited

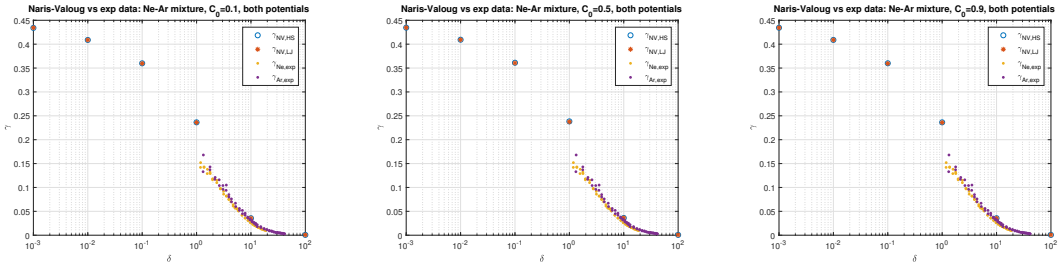

(a) $C_0 = 0.1$. (b) $C_0 = 0.5$. (c) $C_0 = 0.9$.

Figure 4.1.: Ne-Ar mixture: TPD exponent computed via Eq. (4.43) for different values of C_0 (NV). ○: HS interaction; ∗: LJ potential; ●: single-gas experimental data for Ne and Ar.

a variational method to obtain analytical expressions of the physical quantities of interest valid only in some rarefaction regime; viceversa, here we will rely on numerical computations, but performed for a much wider range of rarefaction.
To perform the numerical analysis, we shall rely on some datasets already present in literature about kinetic coefficients and mass fluxes computed as a function of the rarefaction parameter. In particular, we shall refer to [79, 78, 81]. Two different mixtures of noble gases will be studied: Ne-Ar mixture, for which the two molecular masses are quite similar, and He-Xe, for which, viceversa, the masses are very different.

4.4.1. Effect of the intermolecular potential

In [79] (NV) are reported numerical data on the kinetic coefficients for both mixtures for a wide range of δ and for different relative concentrations. The reported results refer to the case of diffuse reflection and the collision model is the McCormack model. Moreover, to study the influence of the intermolecular interaction potential, two molecular models are used: the rigid spheres and a more realistic potential, that is, the Lennard-Jones model.
Since the available data concern the kinetic coefficients, we will study the TPD exponent as defined in Eq. (4.43), γ_{global}.

4.4.1.1. Ne-Ar mixture

The results concerning Ne-Ar mixture are reported in Figs. 4.1 and 4.2.
From Fig. 4.1, in which we compare the intermolecular potentials for fixed values of C_0, we deduce that γ does not depend on the intermolecular potential for all molar concentrations. This is not necessarily in contrast with the fact that a correct description of the interparticle force law is of paramount importance to reproduce properly experimental results for gas mixtures ([37]). Indeed, being the TPD exponent a ratio between quantities, it may involve a sort of "normalization" with respect the effect of the potential. Actually, the effect of the potential is visible in the kinetic coefficients involving the concentration gradient, particularly when $\delta > 10^{-1}$, but our definitions of γ are independent from this effect.
In Fig. 4.2, we compare the different molar concentrations for the same potential: we see that γ is practically independent also from the value of C_0 for both potentials.
Both these facts agree with what is observed by the authors:

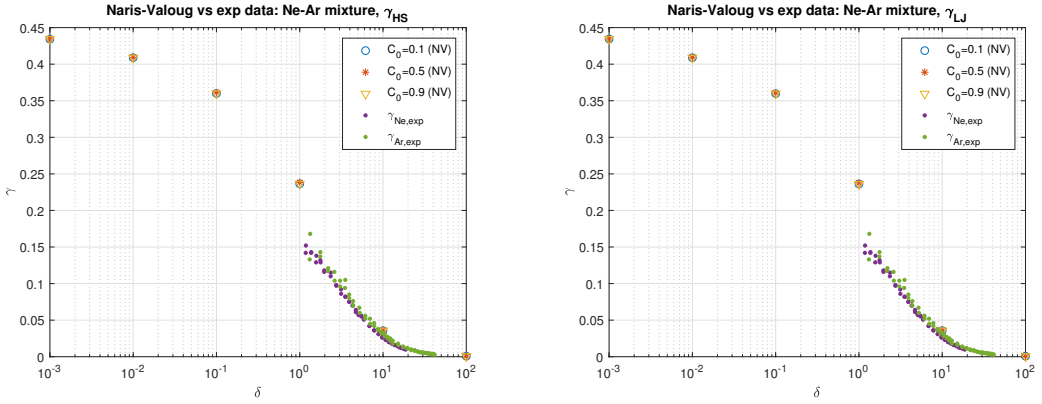

(a) HS interaction. (b) LJ potential.

Figure 4.2.: Ne-Ar mixture: TPD exponent computed via Eq. (4.43) for different intermolecular potentials (NV). ○: $C_0 = 0.1$; ∗: $C_0 = 0.5$; ▽: $C_0 = 0.9$; ●: single-gas experimental data for Ne and Ar.

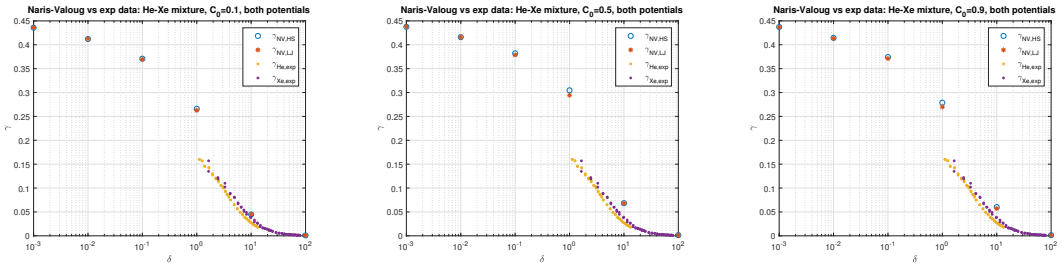

(a) $C_0 = 0.1$. (b) $C_0 = 0.5$. (c) $C_0 = 0.9$.

Figure 4.3.: He-Xe mixture: TPD exponent computed via Eq. (4.43) for different values of C_0 (NV). ○: HS interaction; ∗: LJ potential; ●: single-gas experimental data for He and Xe.

- Λ_{PP} is practically insensitive to the intermolecular potential, and Λ_{PT} is only slightly sensitive on it;
- in the Ne-Ar case, both Λ_{PP} and Λ_{PT} are practically independent from the molar concentration.

Finally, we notice that in all cases the numerical TPD exponent has the correct limits for $\delta \to 0$ and $\delta \to \infty$ and a qualitative behaviour similar to the numerical single-gas one presented, e.g., in Fig. 3.21c. Moreover, in the experimental range of δ the trend is similar to the experimental single-gas TPD exponents.

4.4.1.2. He-Xe mixture

The results concerning He-Xe mixture are reported in Figs. 4.3 and 4.4.
From Fig. 4.3, in which we compare the intermolecular potentials for fixed values of C_0, we see that γ is slightly dependent on the interaction potential, especially for intermediate regimes of rarefaction ($\delta \approx 1$).
In Fig. 4.4, we compare the different C_0 for the same fixed potential: we see that the value of the molar concentration has a visible effect on γ, especially for $10^{-1} < \delta < 10$. In particular, we can observe that γ for large C_0 ($C_0 \approx 1$) is similar to the one for small

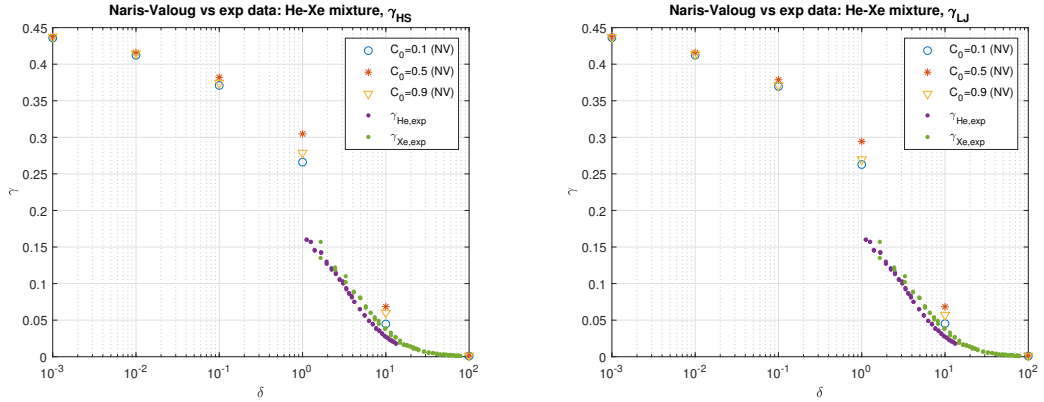

(a) HS interaction.

(b) LJ potential.

Figure 4.4.: He-Xe mixture: TPD exponent computed via Eq. (4.43) for different intermolecular potentials (NV). ○: $C_0 = 0.1$; ∗: $C_0 = 0.5$; ▽: $C_0 = 0.9$; ●: single-gas experimental data for He and Xe.

C_0 ($C_0 \approx 0$), and is bigger than both of these for intermediate values of C_0 ($C_0 \approx 0.5$). Both these facts agree with what is observed in the paper:

- Λ_{PP} is still practically insensitive to the intermolecular potential, and Λ_{PT} is still only slightly sensitive on it, but the effect of the intermolecular potential is more dominant in the He-Xe mixture rather than in the Ne-Ar mixture, so a possible discrepancy between the effects of the two potentials is amplified in the He-Xe case;

- in the He-Xe case, the variation of C_0 has a much more significant effect on both Λ_{PP} and Λ_{PT} than in the Ne-Ar case, but each of these kinetic coefficients has practically the same value for the two concentrations $C_0 = 0$ and $C_0 = 1$.

Finally, we notice that, as for the Ne-Ar mixture, in all cases the numerical TPD exponent has the correct limits for $\delta \to 0$ and $\delta \to \infty$ and a qualitative behaviour similar to the numerical single-gas one. Moreover, in the experimental range of δ the trend is similar to the experimental single-gas TPD exponents.

4.4.2. "Single-gas" and "global" definitions

In [78] (SV) are reported numerical data, for a wide range of δ, on the species-specific mass and heat fluxes due to both pressure and temperature gradients for both mixtures. Also in this case, the effect of different relative concentrations is studied. The reported results refer to the case of hard-sphere interaction and diffuse boundary conditions, and the collision model is still the McCormack model.
In this case, since species-specific data are available, we can analyse both the definitions of TPD exponent for a mixture that we conjectured in Section 4.3.2: the single-gas definition Eq. (4.40), γ_s, and the global definition Eq. (4.41), γ_{global}.

4.4.2.1. Ne-Ar mixture

The results concerning Ne-Ar mixture are reported in Figs. 4.5 to 4.7.
In Fig. 4.5, we compare the single-gas and global definitions of the TPD exponent for

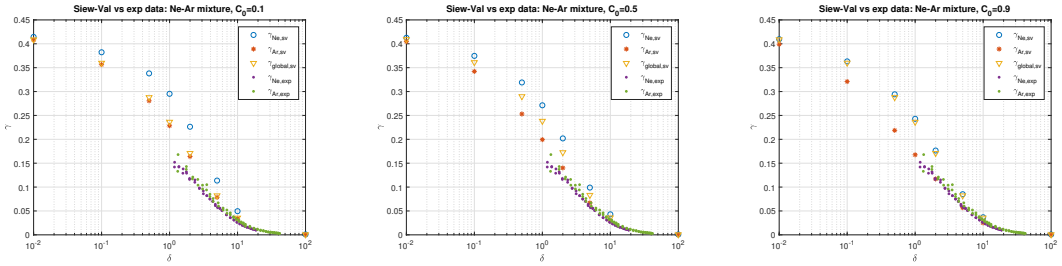

(a) $C_0 = 0.1$. (b) $C_0 = 0.5$. (c) $C_0 = 0.9$.

Figure 4.5.: Ne-Ar mixture: TPD exponent for different values of C_0 (SV). ○: single-gas γ computed via Eq. (4.40) for Ne; ∗: single-gas γ computed via Eq. (4.40) for Ar; ▽: global γ computed via Eq. (4.41); ●: single-gas experimental data for Ne and Ar.

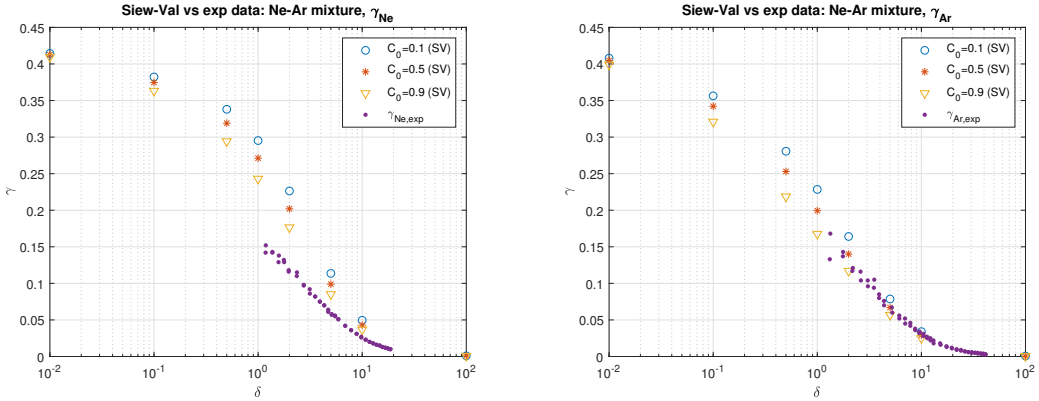

(a) Ne. (b) Ar.

Figure 4.6.: Ne-Ar mixture: TPD exponent computed via Eq. (4.40) for both Ne (Fig. 4.6a) and Ar (Fig. 4.6b) (SV). ○: $C_0 = 0.1$; ∗: $C_0 = 0.5$; ▽: $C_0 = 0.9$; ●: single-gas experimental data for Ne and Ar.

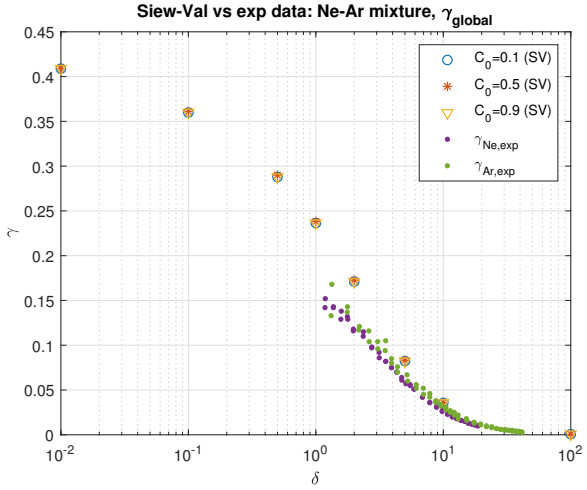

Figure 4.7.: Ne-Ar mixture: TPD exponent computed via Eq. (4.41) (SV). ○: $C_0 = 0.1$; ∗: $C_0 = 0.5$; ▽: $C_0 = 0.9$; ●: single-gas experimental data for Ne and Ar.

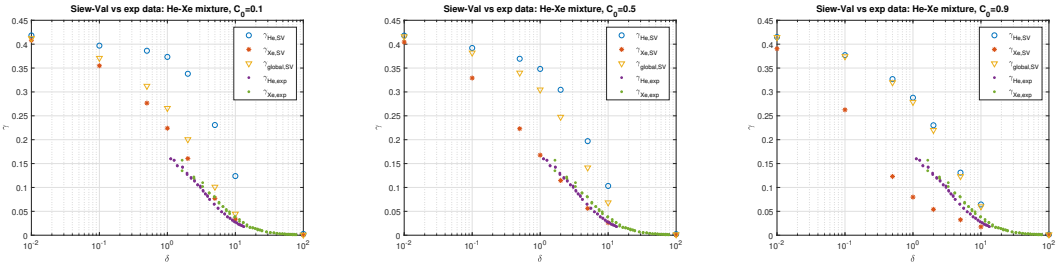

(a) $C_0 = 0.1$. (b) $C_0 = 0.5$. (c) $C_0 = 0.9$.

Figure 4.8.: He-Xe mixture: TPD exponent for different values of C_0 (SV). ○: single-gas γ computed via Eq. (4.40) for He; ∗: single-gas γ computed via Eq. (4.40) for Xe; ▽: global γ computed via Eq. (4.41); ●: single-gas experimental data for He and Xe.

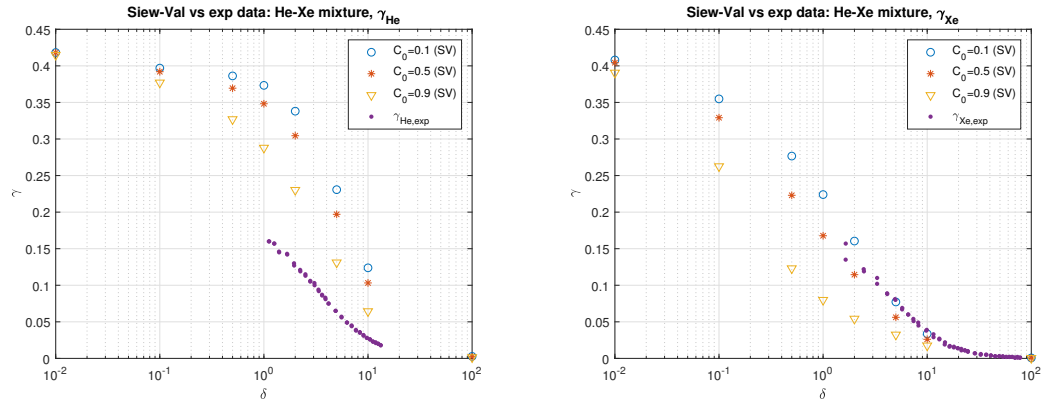

(a) He. (b) Xe.

Figure 4.9.: He-Xe mixture: TPD exponent computed via Eq. (4.40) for both He (Fig. 4.9a) and Xe (Fig. 4.9b) (SV). ○: $C_0 = 0.1$; ∗: $C_0 = 0.5$; ▽: $C_0 = 0.9$; ●: single-gas experimental data for He and Xe.

different fixed values of C_0. We can observe that for $C_0 = 0.1$ the single-gas γ for Ar is very similar to the global one, while for $C_0 = 0.9$ γ_{global} is closer to the single-gas one for Ne. We may interpret this as the fact that for extremal values of C_0 we reach the limit of single-gas behaviour.
In Fig. 4.6, we evaluate the effect of different values of C_0 on the single-gas TPD exponent Eq. (4.40) for both gases separately. Also in this case, we observe that the single-gas γ for Ne (Fig. 4.6a) seems to tend to the single-gas experimental one as $C_0 \to 1$. In the case of Ar (Fig. 4.6b), the behaviour is more ambiguous.
In Fig. 4.7, we consider the effect of different values of the molar concentration on the global TPD exponent. Since Eq. (4.42) holds, this graph is exactly the same as Fig. 4.2a, up to at most a negligible discrepancy due to different numerical schemes. Hence, the considerations are the same.
Finally, we notice that, as in the previous cases, the numerical TPD exponent has the correct limits for $\delta \to 0$ and $\delta \to \infty$ and a qualitative behaviour similar to the numerical single-gas one. Moreover, in the experimental range of δ the trend is similar to the experimental single-gas TPD exponents.

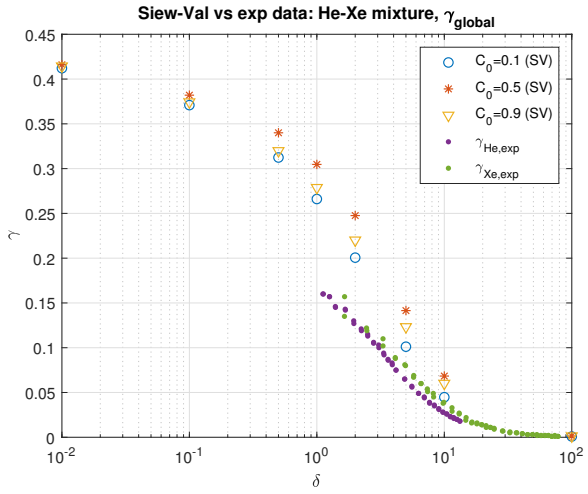

Figure 4.10.: He-Xe mixture: TPD exponent computed via Eq. (4.41) (SV). ○: $C_0 = 0.1$; ∗: $C_0 = 0.5$; ▽: $C_0 = 0.9$; •: single-gas experimental data for He and Xe.

4.4.2.2. He-Xe mixture

The results concerning He-Xe mixture are reported in Figs. 4.8 to 4.10.
In Fig. 4.8, we compare the single-gas and global definitions of the TPD exponent for different fixed values of C_0. We can observe that for $C_0 = 0.1$ the single-gas γ for Xe is closer to γ_{global}, while for $C_0 = 0.9$ γ_{global} is much more similar to the single-gas one for He. We may interpret this as the fact that for extremal values of C_0 we reach the limit of single-gas behaviour. We observe that the convergence of γ_{global} to γ_s is much faster when $C_0 \to 1$ (that is, converging toward the lighter species, $s = 1$, He) rather than $C_0 \to 0$ (that is, converging toward the heavier species, $s = 2$, Xe). In fact, when $C_0 = 0.5$ γ_{global} is visibly closer to γ_{He} rather than to γ_{Xe}. Actually, this seems to be true also for the Ne-Ar mixture, but it is much more evident in the He-Xe case.
In Fig. 4.9, we evaluate the effect of different values of C_0 on the single-gas TPD exponent Eq. (4.40) for both gases separately. We observe that γ_{He} (Fig. 4.9a) seems to tend to the single-gas experimental γ as $C_0 \to 1$. In the case of Xe (Fig. 4.9b), the behaviour is even more evident: for $C_0 = 0.1$, γ_{Xe} and $\gamma_{\text{Xe,exp}}$ practically overlap in the experimental range.
In Fig. 4.10, we consider the effect of different values of the molar concentration on the global TPD exponent. Since Eq. (4.42) holds, this graph is exactly the same as Fig. 4.4a, up to at most a negligible discrepancy due to different numerical schemes. Hence, the considerations are the same.
Finally, we notice that, as in the previous cases, the numerical TPD exponent has the correct limits for $\delta \to 0$ and $\delta \to \infty$ and a qualitative behaviour similar to the numerical single-gas one. Moreover, in the experimental range of δ the trend is similar to the experimental single-gas TPD exponents.

4.4.3. Effect of the collision model

In [81] (GS) are reported numerical data, for a wide range of δ, on the species-specific mass and heat fluxes due to both pressure and temperature gradients for both mixtures. Only the case $C_0 = 0.4$ is considered. The reported results refer to the case of hard-

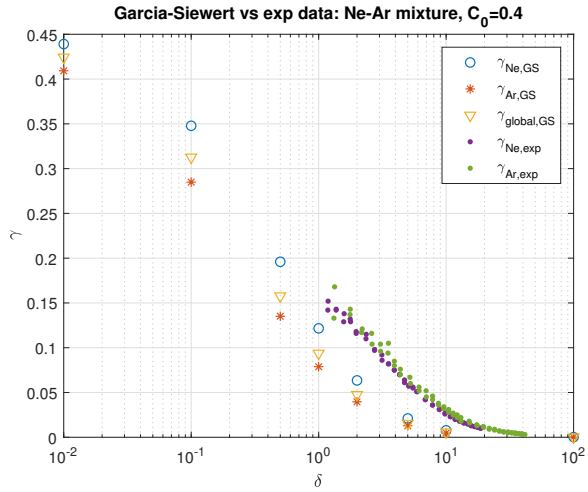

Figure 4.11.: Ne-Ar mixture: TPD exponent computed via Eq. (4.40) and Eq. (4.41) (GS). ○: γ via Eq. (4.40) for Ne; ∗: γ via Eq. (4.40) for Ar; ▽: global γ; ●: single-gas experimental data for Ne and Ar.

sphere interaction and Maxwell boundary conditions, chosen differently in the lower and upper plates: $\alpha_1 = 0.2$, $\alpha_2 = 0.4$ for the lower plate, $\beta_1 = 0.6$, $\beta_2 = 0.8$ for the upper plate. This time, the LBE is solved, so no kinetic model is used.
In this case, since species-specific data are available, we can analyse both the definitions of TPD exponent for a mixture that we conjectured in Section 4.3.2: the "single-gas" definition Eq. (4.40) and the "global" definition Eq. (4.41).

4.4.3.1. Ne-Ar mixture

The results concerning Ne-Ar mixture are reported in Fig. 4.11, in which we compare the single-gas and global definitions of the TPD exponent with experimental data. We observe that γ_{global} is about the mean between the two numerical single-gas γ, but closer to γ_{Ar}: this makes sense, since $C_0 = 0.4$.
Moreover, we notice that, as in the previous cases, the numerical TPD exponent has the correct limits for $\delta \to 0$ and $\delta \to \infty$ and a qualitative behaviour similar to the numerical single-gas one.

4.4.3.2. He-Xe mixture

The results concerning He-Xe mixture are reported in Fig. 4.12, in which we compare the single-gas and global definitions of the TPD exponent with experimental data. We observe that γ_{global} is about the mean between the two numerical single-gas γ, but closer to γ_{Xe}: this makes sense, since $C_0 = 0.4$.
Moreover, we notice that, as in the previous cases, the numerical TPD exponent has the correct limits for $\delta \to 0$ and $\delta \to \infty$.
and a qualitative behaviour similar to the numerical single-gas one. Moreover, in the experimental range of δ the trend is similar to the experimental single-gas TPD exponents.

However, even if some of the qualitative features of the TPD exponent (limits as $\delta \to 0$ and $\delta \to \infty$, strict monotonicity, inflection point at $\delta \approx 1$) seem to appear also in the LBE description, the quantitative values are rather different. In particular, the

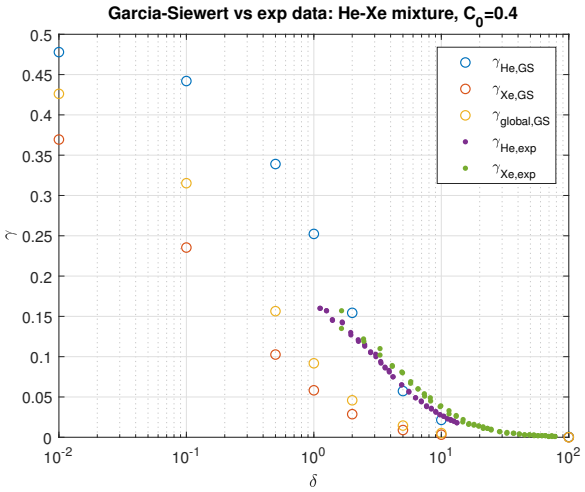

Figure 4.12.: He-Xe mixture: TPD exponent computed via Eq. (4.40) and Eq. (4.41) (GS). ○: γ via Eq. (4.40) for He; ∗: γ via Eq. (4.40) for Xe; ▽: global γ; ●: single-gas experimental data for He and Xe.

results in (GS) often underestimates the ones in (NV) and (SV), which on the other hand seem to be physically more consistent, both in the quantitative values in the experimental range and in the behaviour of single-gas limit. (Actually, this last remark cannot be done for (GS) data, since only one value of C_0 is considered.) It is difficult to tell precisely if this fact is due to the different choice of the collision model or to the different boundary conditions (which, in (GS), are chosen in a rather arbitrary and probably non physical way), so this comparison is not useful to conclude whether the McCormack model is a valid alternative to the LBE, at least in the study of the TPD effect.

5. Conclusions and future research

5.1. Conclusions

5.1.1. Single gas

In the case of single gases, the aim was to exploit the TPD effect in order to improve the gas-surface models in a rarefied gas and to refine the description of second-order slip boundary conditions in the transition regime.

Concerning the first goal, we have studied the linearized Boltzmann equation for the Poiseuille-thermal creep problem for a single monatomic gas flowing between two infinite parallel plates. The Cercignani-Lampis boundary conditions have been considered. Firstly, we have recalled that, via a variational method, it is possible to obtain analytical expressions of slip coefficients and mass flow rates (and, hence, also of the TPD coefficient). The analytical expressions presented here are valid only, *a priori*, in the slip (and hydrodynamic) regime. Then, we have tried to extract the two accommodation coefficients describing the CL model by the use of these analytical expressions for five noble gases: Helium, Neon, Argon, Krypton, Xenon.
Despite an apparent intrinsic instability in both the extraction procedures presented, especially about α_n, we have found a quite good agreement in the numerical values of both accommodation coefficients, obtained in two independent ways, and in their validation, for almost all the noble gases involved. The only unsatisfactory case was the one of Xenon, for which the validation step and the agreement between the two pairs of accommodation coefficients were the worst.

About the second goal, we have confirmed that the "extended" slip regime goes well beyond the classical one, including a part of the transition regime: the second-order slip model can be considered reliable up to a rarefaction regime of at least $\delta = 3$ for all gases involved.

5.1.2. Gaseous mixtures

Previous literature concerning the TPD effect in gaseous mixtures is rather poor, especially about the rigorous definition of the TPD coefficient and its systematic study through numerical results. For this reason, we have chosen as starting point the formulation of a good definition of the TPD exponent in the case of mixtures. In order to achieve this, we have moved directly from its definition in the single-gas case, simply as the ratio between the thermal creep and the Poiseuille mass fluxes, but considering first the two gases separately and then the mixture as a whole.
The second step has been to derive, via the projection procedure, the Boltzmann-type equations governing the thermal creep problem in a planar channel for a binary mixture described by the McCormack model. Due to the much higher complexity of these

equations with respect to the single-gas case, we have chosen the Maxwell model for boundary conditions. Then, we have exploited some datasets, already present in literature, derived from the numerical solution of the same equations we reported here, for two different binary mixtures (Ne-Ar and He-Xe). Hence, we could use both the new definitions of the TPD coefficient to compute this quantity, for diffuse boundary conditions but for a much wider range of the gas rarefaction than the single-gas case, thanks to the direct numerical solution of the Boltzmann equation (rather than the Navier-Stokes ones with slip boundary conditions).
Despite the quite *naïve* approach, we were able to point out several interesting aspects of the TPD effect for a gaseous mixture. For example, we found that the functional dependence of γ on δ and its qualitative behaviour seem to be the same as the single-gas one in the whole regime of rarefaction, including the limit cases of free-molecular and continuum regimes.
We have also tried to evaluate the effect of the choice of different intermolecular interaction potentials. Our conclusion is that the TPD effect seems to be practically insensitive to the interaction potential (and hence the hard-spheres model can be adopted) if the molecular masses are close enough (Ne-Ar), while the discrepancy is still small, but visible, if the mass ratio is sufficiently large (He-Xe), especially for $\delta \approx 1$ and $C_0 \approx 0.5$.
Finally, we have also compared the effect of different choices of the model for the collision integral. Due to the limited data available in this case, we have not been able to conclude whether the McCormack model is a valid alternative to the LBE description.

5.2. Future research

There are still several issues that deserve to be analysed.

5.2.1. Single gas

Extension of the rarefaction range The variational approach turned out to be very useful in order to determine analytical expressions for various physical quantities, to obtain a very precise assessment of the accommodation coefficients. The limitation is that these expressions, in particular the ones of the Poiseuille and thermal creep mass fluxes, are obtained with a comparison with the analytical solutions of the Navier-Stokes equation with second-order slip boundary conditions, and therefore are valid only in the slip regime. A step further may be to solve numerically the LBE with the CL boundary conditions assessed in this work and compare the results with some experimental data, in order to check if these accommodation coefficients can reproduce the real behaviour of the gases considered in the whole rarefaction regime. To this end, much more experimental data will be needed, especially in conditions of very high rarefaction.

Different geometries The channel flow was a good benchmark case to test the reliability of the TPD effect in the study of single-gas flows driven by pressure and temperature gradients. Nonetheless, it would be useful to generalize this procedure to other geometries (e.g., circular, elliptical or square tubes), to perform a systematic study on the influence of the shape of the gas container on the gas-surface interaction and on the TPD phenomenon.

5.2.2. Gaseous mixtures

Accurate numerical analysis Even for binary mixtures, there are much more parameters that may influence the behaviour of the mixture than in the single-gas case. These parameters are, for example, the diameters, masses and number densities of the species, or the accommodation coefficients. An accurate and systematic numerical analysis on the behaviour of such a mixture could be useful to analyse in detail how the different physical quantities of interest (mass flow rates, kinetic coefficients, etc.) change when, for example, one gas is much or slightly heavier than the other, or as the relative molar concentration C_0 change continuously from 0 to 1. To this end, one should have the possibility to change arbitrarily the above-mentioned physical parameters, and therefore a code should be exploited, to solve numerically the equations for whatever choice of the parameters.

Different boundary conditions The CL model for the boundary conditions is more refined than the Maxwell model, but it is much more complex. This complexity is still manageable in the single-gas case, but this is no more true when dealing with mixtures. Nonetheless, to obtain accurate model for mixture-surface interaction, in the future it may be necessary to try to implement some more refined model. To begin with, it would be useful to have complete and detailed datasets, concerning the quantities of interest, not only for diffuse boundary conditions, but for at least different values of the only accommodation coefficient of the Maxwell model, to perform a rigorous analysis of its effects on the TPD phenomenon.

Different collisional models One of the most critical issues in this problem is the choice of a realistic collisional model. The McCormack model is often chosen because it is able to give correct results in both Poiseuille and thermal creep problems, which both, in turn, have a leading role in the study of the TPD effect. Nonetheless, as already seen, a more rigorous analysis on its reliability as an alternative to the LBE for gas mixtures is mandatory (see [81]). On the other hand, this model, although being already an "economical alternative" to the LBE, is still quite complex to manage from both analytical and numerical point of view. Hence, another idea, in contrast with preferring the LBE instead of a less refined model, is to simplify more: for example, it would be useful to compare the results of the modified-BGK model (see [37]) for thermal creep problem with the McCormack ones. If they turn out to be quite similar, the BGK-type model will be an interesting alternative to the McCormack one, due to its much simpler equations, allowing even a semi-analytical representation of the solution.

Experimental data What is lacking in the mixtures case, with respect to the single-gas case, is the availability of experimental data about the TPD effect, to be used to check the reliability of the many approximations used to model a problem of such complexity.

References

Books

[1] P. Tabeling. *Introduction to Microfluidics*. Oxford University Press, 2005.

[6] C. Cercignani. *The Boltzmann Equation and Its Applications*. Applied Mathematical Sciences. Springer-Verlag New York, 1988.

[7] G. Karniadakis, A. Beskok, and N. Aluru. *Microflows and Nanoflows: Fundamentals and Simulation*. Interdisciplinary Applied Mathematics. Springer-Verlag New York, 2005.

[13] C. Cercignani, R. Illner, and M. Pulvirenti. *The Mathematical Theory of Dilute Gases*. Applied Mathematical Sciences. Springer-Verlag New York, 1994.

[18] G. A. Bird. *Molecular Gas Dynamics and the Direct Simulation of Gas Flows*. Oxford Engineering Science Series. Oxford University Press, 1994.

[19] Y. Sone. *Kinetic Theory and Fluid Dynamics*. Modeling and Simulation in Science, Engineering and Technology. Birkhäuser Basel, 2002.

[21] C. Cercignani. *Mathematical Methods in Kinetic Theory*. Springer US, 1969.

[22] C. Cercignani. *Rarefied Gas Dynamics. From Basic Concepts to Actual Calculations*. Cambridge Texts in Applied Mathematics. Cambridge University Press, 2000.

[31] F. Sharipov. *Rarefied Gas Dynamics. Fundamentals for Research and Practice*. Wiley-VCH, 2015.

[35] J. M. Burgers. *Flow Equations for Composite Gases*. Applied Mathematics and Mechanics. Academic Press, 1969.

[38] S. Chapman and T. G. Cowling. *The mathematical theory of non-uniform gases: an account of the kinetic theory of viscosity, thermal conduction, and diffusion in gases*. Cambridge Mathematical Library. Cambridge University Press, 1970.

[48] E. H. Kennard. *Kinetic Theory Of Gases With An Introduction To Statistical Mechanics*. International Series In Pure And Applied Physics. McGraw-Hill Book Company, Inc., 1938.

[49] Y. Sone. *Molecular gas dynamics: theory, techniques, and applications*. Modeling and Simulation in Science, Engineering, and Technology. Birkhäuser, 2007.

[52] S. R. de Groot and P. Mazur. *Non-equilibrium thermodynamics*. Dover Publications, 1984.

[77] N. A. Downie. *Industrial gases*. Kluwer Academic Publishers, 2002.

[84] J. O. Hirshfelder, C. F. Curtiss, and R. B. Bird. *Molecular theory of gases and liquids*. John Wiley & Sons, 1964.

Articles

[2] R. P. Feynman. ≪There's Plenty of Room at the Bottom. An invitation to open up a new field of physics.≫ In: *Engineering and Science* 23.5 (1960). URL: https://resolver.caltech.edu/CaltechES:23.5.0.

[3] D. Eigler and E. Schweizer. ≪Positioning single atoms with a scanning tunnelling microscope≫. In: *Nature* 344.5 (1990). DOI: 10.1038/344524a0.

[4] IBM. *A Boy And His Atom: The World's Smallest Movie*. 2013. URL: https://www.research.ibm.com/articles/madewithatoms.shtml (visited on 12/03/2020). (accessed on December 2020).

[5] IBM. *A Boy And His Atom: The World's Smallest Movie*. 2013. URL: https://www.youtube.com/watch?v=oSCX78-8-q0 (visited on 12/03/2020). (accessed on December 2020).

[8] D. J. Laser and J. G. Santiago. ≪A review of micropumps≫. In: *Journal of Micromechanics and Microengineering* 14 (2004). DOI: 10.1088/0960-1317/14/6/R01.

[9] R. M. Young. ≪Analysis of a micromachine based vacuum pump on a chip actuated by the thermal transpiration effect≫. In: *Journal of Vacuum Science & Technology B* 17 (1999). DOI: 10.1116/1.590551.

[10] K. Pharas and S. McNamara. ≪Knudsen pump driven by a thermoelectric material≫. In: *Journal of Micromechanics and Microengineering* 20 (2010). DOI: 10.1088/0960-1317/20/12/125032.

[11] J. Hobson and D. Salzman. ≪Review of pumping by thermal molecular pressure≫. In: *Journal of Vacuum Science & Technology A* 18 (2000). DOI: 10.1116/1.582420.

[12] A. Maniou. ≪Preliminary design of a Knudsen pump≫. MSc Thesis. University of Thessaly, 2011.

[14] C. Bardos, F. Golse, and C. D. Levermore. ≪Fluid dynamic limits of kinetic equations. I. Formal derivations≫. In: *Journal of Statistical Physics* 63 (1991). DOI: 10.1007/BF01026608.

[15] C. Bardos, F. Golse, and C. D. Levermore. ≪Fluid dynamic limits of kinetic equations. II. Convergence proofs for the boltzmann equation≫. In: *Communications on Pure and Applied Mathematics* 46 (1993). DOI: 10.1002/cpa.3160460503.

[16] B. Desjardins et al. ≪Incompressible limit for solutions of the isentropic Navier-Stokes equations with Dirichlet boundary conditions≫. In: *Journal de Mathématiques Pures et Appliquées* 78 (1999). DOI: 10.1016/S0021-7824(99)00032-X.

[17] R. J. DiPerna and P.-L. Lions. ≪Global solutions of Boltzmann's equation and the entropy inequality≫. In: *Archive for Rational Mechanics and Analysis volume* 114 (1991). DOI: 10.1016/S0021-7824(99)00032-X.

[20] H. Grad. ≪On the Kinetic Theory of Rarefied Gases≫. In: *Communications on Pure and Applied Mathematics* 2 (1949). DOI: 10.1002/cpa.3160020403.

[23] J. C. Maxwell. ≪On Stresses in Rarefied Gases arising from Inequalities of Temperature≫. In: *Philosophical Transactions of the Royal Society of London* 170 (1879).

[24] L. Wu and H. Struchtrup. ≪Assessment and development of the gas kinetic boundary condition for the Boltzmann equation≫. In: *Journal of Fluid Mechanics* 823 (2017), pp. 511–537. DOI: 10.1017/jfm.2017.326.

[25] F. Sharipov. ≪Application of the Cercignani-Lampis scattering kernel to calculations of rarefied gas flows. I. Plane flow between two parallel plates≫. In: *European Journal of Mechanics - B/Fluids* 21 (2002). DOI: 10.1016/S0997-7546(01)01160-8.

[26] C. Cercignani and M. Lampis. ≪Kinetic models for gas-surface interactions≫. In: *Transport Theory and Statistical Physics* 1 (1971). DOI: 10.1080/00411457108231440.

[27] S. Lorenzani. ≪Higher order slip according to the linearized Boltzmann equation with general boundary conditions≫. In: *Philosophical Transactions of the Royal Society* 369 (2011), pp. 2228–2236. DOI: 10.1098/rsta.2011.0059.

[28] N. N. Nguyen et al. ≪Variational derivation of thermal slip coefficients on the basis of the Boltzmann equation for hard-sphere molecules and Cercignani-Lampis boundary conditions: Comparison with experimental results≫. In: *Physics of Fluids* 32 (2020). DOI: 10.1063/5.0025282.

[29] P. Bhatnagar, E. Gross, and M. Krook. ≪A Model for Collision Processes in Gases. I. Small Amplitude Processes in Charged and Neutral One-Component Systems≫. In: *Physical Review* 94 (1954). DOI: 10.1103/PhysRev.94.511.

[30] P. Welander. ≪On the temperature jump in a rarefied gas≫. In: *Arkiv Fysik* 7 (1954).

[32] S. Lorenzani. ≪Kinetic modeling for the time-dependent behavior of binary gas mixtures≫. In: vol. 2132. 2019. DOI: 10.1063/1.5119626.

[33] P. Andries, K. Aoki, and B. Perthame. ≪A Consistent BGK-Type Model for Gas Mixtures≫. In: *Journal of Statistical Physics* 106 (2002). DOI: 10.1023/A:1014033703134.

[34] F. J. McCormack. ≪Construction of linearized kinetic models for gaseous mixtures and molecular gases≫. In: *Physics of Fluids* 16 (1973). DOI: 10.1063/1.1694272.

[36] V. Zhdanov, Y. Kagan, and A. Sazykin. ≪Effect of viscous transfer of momentum on diffusion in a gas mixture≫. In: *Journal of Experimental and Theoretical Physics* 15 (1962).

[37] S. Lorenzani. ≪A microchannel flow application of a linearized kinetic Bhatnagar-Gross-Krook-type model for inert gas mixtures with general intermolecular forces≫. In: *Physics of Fluids* 31 (2019). DOI: 10.1063/1.5098013.

[39] H. Akhlaghi and E. Roohi. ≪Mass flow rate prediction of pressure-temperature-driven gas flows through micro/nanoscale channels≫. In: *Continuum Mechanics and Thermodynamics* 26 (2013). DOI: 10.1007/s00161-013-0290-0.

[40] K. Aoki et al. ≪Diffusion models for Knudsen compressors≫. In: *Physics of Fluids* 19 (2007). DOI: 10.1063/1.2798748.

[41] Y.-L. Han et al. ≪Experimental and Computational Studies of Temperature Gradient-Driven Molecular Transport in Gas Flows through Nano/Microscale Channels≫. In: *Nanoscale and Microscale Thermophysical Engineering* 11 (2007). DOI: 10.1080/15567260701337209.

[42] F. Sharipov and V. Seleznev. ≪Data on Internal Rarefied Gas Flows≫. In: *Journal of Physical and Chemical Reference Data* 27 (1998). DOI: 10.1063/1.556019.

[43] X. Wang et al. ≪Knudsen pumps: a review≫. In: *Microsystems & Nanoengineering* 6.26 (2020). DOI: 10.1038/s41378-020-0135-5.

[44] P. Taheri and H. Struchtrup. ≪Rarefaction effects in thermally-driven microflows≫. In: *Physica A: Statistical Mechanics and its Applications* 389 (2010). DOI: 10.1016/j.physa.2010.03.050.

[45] O. Reynolds. ≪On Certain Dimensional Properties of Matter in the Gaseous State≫. In: *Philosophical Transactions of the Royal Society of London* 170 (1879). DOI: 10.2307/109294.

[46] M. Knudsen. ≪Eine Revision der Gleichgewichtsbedingung der Gase. Thermische Molekularströmung≫. In: *Annalen der Physik* 336 (1909). DOI: 10.1002/andp.19093360110.

[47] M. Knudsen. ≪Thermischer Molekulardruck der Gase in Röhren und porösen Körpern≫. In: *Annalen der Physik* 336 (1910). DOI: 10.1002/andp.19103360310.

[50] H. Struchtrup. ≪Maxwell boundary condition and velocity dependent accommodation coefficient≫. In: *Physics of Fluids* 25 (2013). DOI: 10.1063/1.4829907.

[51] L. Onsager. ≪Reciprocal relations in irreversible processes≫. In: *Physical Review* 37 (1931).

[53] S. K. Loyalka. ≪Kinetic Theory of Thermal Transpiration and Mechanocaloric Effect. I≫. In: *The Journal of Chemical Physics* (1971). DOI: 10.1063/1.1676780.

[54] T. Kanki and S. Iuchi. ≪Poiseuille flow and thermal creep of a rarefied gas between parallel plates≫. In: *Physics of Fluids* 16 (1973). DOI: 10.1063/1.1694393.

[55] F. Sharipov. ≪Rarefied gas flow through a long tube at any temperature ratio≫. In: *Journal of Vacuum Science & Technology A* 14 (1996). DOI: 10.1116/1.579991.

[56] S.F. Borisov et al. ≪Thermomolecular pressure difference at low knudsen numbers≫. In: *Journal of Engineering Physics* 25 (1973). DOI: 10.1007/BF00838141.

[57] V.G. Chernyak, B.T. Porodnov, and P.E. Suetin. ≪Application of the variation method to the problem of thermomolecular pressure difference in a cylindrical channel≫. In: *Journal of Engineering Physics* 26 (1974). DOI: 10.1007/BF00827694.

[58] K. Ritos et al. ≪Pressure- and Temperature-Driven Flow Through Triangular and Trapezoidal Microchannels≫. In: *Heat Transfer Engineering* 32 (2011). DOI: 10.1080/01457632.2011.562455.

[59] F. Sharipov. ≪Rarefied gas flow through a long tube at arbitrary pressure and temperature drops≫. In: *Journal of Vacuum Science & Technology A* 15 (1997). DOI: 10.1116/1.580904.

[60] N. Gupta and Y. Gianchandani. ≪Thermal transpiration in zeolites: A mechanism for motionless gas pumps≫. In: *Applied Physics Letters* 93 (2008). DOI: 10.1063/1.3025304.

[61] D. Copic and S. McNamara. ≪Efficiency derivation for the Knudsen pump with and without thermal losses≫. In: *Journal of Vacuum Science & Technology A* 27 (2009). DOI: 10.1116/1.3114444.

[62] D. J. Turner. ≪A mathematical analysis of a thermal transpiration vacuum pump≫. In: *Vacuum* 16 (1966). DOI: 10.1016/0042-207X(66)91429-1.

[63] S. Vargo et al. ≪Knudsen compressor as a micro- and macroscale vacuum pump without moving parts or fluids≫. In: *Journal of Vacuum Science & Technology A* 17 (1999). DOI: 10.1116/1.581765.

[64] E. P. Muntz et al. ≪Performance analysis and optimization considerations for a Knudsen compressor in transitional flow≫. In: *Journal of Vacuum Science & Technology A* 20 (2002). DOI: 10.1116/1.1430250.

[65] S. McNamara and Y. B. Gianchandani. ≪A micromachined Knudsen pump for on-chip vacuum≫. In: *TRANSDUCERS '03. 12th International Conference on Solid-State Sensors, Actuators and Microsystems. Digest of Technical Papers (Cat. No.03TH8664)*. Vol. 2. 2003. DOI: 10.1109/SENSOR.2003.1217167.

[66] S. Naris and D. Valougeorgis. ≪Gas flow in a grooved channel due to pressure and temperature difference≫. In: *4th International Conference on Nanochannels, Microchannels and Minichannels*. 2006.

[67] K. Aoki et al. ≪Numerical Simulation of a Knudsen Pump Using the Effect of Curvature of the Channel≫. In: 2007.

[68] O. I. Dodulad et al. ≪Knudsen pumps modeling with Lennard-Jones and ab initio intermolecular potentials≫. In: *Vacuum* 109 (2014). DOI: 10.1016/j.vacuum.2014.06.019.

[69] F. Sharipov. ≪Onsager-Casimir reciprocity relations for open gaseous systems at arbitrary rarefaction: I. General theory for single gas≫. In: *Physica A: Statistical Mechanics and its Applications* 203 (1994). DOI: 10.1016/0378-4371(94)90009-4.

[70] F. Sharipov. ≪Onsager-Casimir reciprocity relations for open gaseous systems at arbitrary rarefaction: II. Application of the theory for single gas≫. In: *Physica A: Statistical Mechanics and its Applications* 203 (1994). DOI: 10.1016/0378-4371(94)90009-4.

[71] F. Sharipov. ≪Data on the Velocity Slip and Temperature Jump on a Gas-Solid Interface≫. In: *Journal of Physical and Chemical Reference Data* 40 (2011). DOI: 10.1063/1.3580290.

[72] P. Wang, W. Su, and L. Wu. ≪Thermal transpiration in molecular gas≫. In: *Physics of Fluids* 32 (2020). DOI: 10.1063/5.0018505.

[73] C. Cercignani and S. Lorenzani. ≪Variational derivation of second-order slip coefficients on the basis of the Boltzmann equation for hard-sphere molecules≫. In: *Physics of Fluids* 22 (2010). DOI: 10.1063/1.3435343.

[74] H. Yamaguchi et al. ≪Thermal transpiration flow through a single rectangular channel≫. In: *Journal of Fluid Mechanics* 744 (2014). DOI: 10.1017/jfm.2014.70.

[75] Yamaguchi et al. «Mass flow rate measurement of thermal creep flow from transitional to slip flow regime». In: *Journal of Fluid Mechanics* 795 (2016). DOI: 10.1017/jfm.2016.234.

[76] H. Yamaguchi et al. «Mass flow rate measurement of thermal creep flow from transitional to slip flow regime». In: *Journal of Fluid Mechanics* 795 (2016). DOI: 10.1017/jfm.2016.234.

[78] C. E. Siewert and D. Valougeorgis. «The McCormack model: channel flow of a binary gas mixture driven by temperature, pressure and density gradients». In: *European Journal of Mechanics B/Fluids* 23 (2004), pp. 645–664. DOI: 10.1016/j.euromechflu.2004.03.003.

[79] S. Naris et al. «Gaseous mixture flow between two parallel plates in the whole range of the gas rarefaction». In: *Physica A: Statistical Mechanics and its Applications* 336 (2004), pp. 294–318. DOI: 10.1016/j.physa.2003.12.047.

[80] F. Sharipov and D. Kalempa. «Gaseous mixture flow through a long tube at arbitrary Knudsen numbers». In: *Journal of Vacuum Science & Technology A* 20 (2002). DOI: 10.1116/1.1469010.

[81] R. D. M. Garcia and C. E. Siewert. «Channel flow of a binary mixture of rigid spheres described by the linearized Boltzmann equation and driven by temperature, pressure, and concentration gradients». In: *Society for Industrial and Applied Mathematics* 67 (2007), pp. 1041–1063. DOI: 10.1137/060673606.

[82] S. Kosuge and S. Takata. «Database for flows of binary gas mixtures through a plane microchannel». In: *European Journal of Mechanics - B/Fluids* 27 (2008). DOI: 10.1016/j.euromechflu.2007.08.002.

[83] J. Kestin et al. «Equilibrium and transport properties of the noble gases and their mixtures at low density». In: *Journal of Physical and Chemical Reference Data* 13 (1984). DOI: 10.1063/1.555703.

A. Computation of the Chapman-Cowling integrals

With the same definitions of the different physical quantities as in Section 2.2, the general expression of the Chapman-Cowling integrals $\Omega^{ij}_{s,r}$ is (see [38, 34])

$$\Omega^{ij}_{s,r} = \left(\frac{k_B T}{2\pi\mu^{rs}}\right)^{1/2} \int_0^\infty \int_\Omega e^{-g^2} g^{2r+3} \left(1 - (cos\theta)^l\right) \sigma_{rs}\left(|\mathbf{V}|, \Omega\right) d\Omega dg$$

$$g = \left(\frac{\mu^{rs}}{2k_B T}\right)^{1/2} |\mathbf{V}| \quad \text{(A.1)}$$

where σ_{rs} is the differential scattering cross section for collisions between a molecule of the s-th and a molecule of the r-th species in which the relative velocity $\mathbf{V}$ is deflected through an angle θ and turned into the solid angle $d\Omega$.
In the following, we report the explicit expressions of the $\Omega^{ij}_{s,r}$ integrals for some notable intermolecular interaction potentials (see also [82, 37]).

A.1. Maxwell molecules

In this model, the interaction potential is

$$U^{sr} = \frac{K^{sr}}{r^{\nu-1}} \quad \text{(A.2)}$$

with $\nu = 5$; r is the distance between the center of the molecules and K^{sr} is the interparticle force law constant. The Ω-integrals are therefore given by

$$\Omega^{ij}_{s,r} = \frac{A_i(5)}{2}\sqrt{\frac{\pi K^{sr}}{\mu^{sr}}}\Gamma\left(j + \frac{3}{2}\right) \quad \text{(A.3)}$$

where Γ is the gamma function.
$A_i(5)$ represents the dimensionless collision cross sections, whose values are tabulated in [38].
K^{11} and K^{22} can be written in terms of the single gas viscosity coefficients η_s with the aid of the first Chapman-Enskog expressions for these quantities,

$$\eta_s = \frac{1}{3\pi}\left(\frac{2m_s}{K^{ss}}\right)^{1/2} \frac{k_B T}{A_2(5)} \quad \text{(A.4)}$$

while K^{12} may be determined from the method of the combination rule,

$$K^{12} = \left(K^{11} K^{22}\right)^{1/2}. \quad \text{(A.5)}$$

In order to specify the force constants K^{11} and K^{22}, experimental data on the viscosities η_s of the single gases at the temperature $T = 300\,\mathrm{K}$ may be used, for example given in [83].

A.2. Hard-sphere molecules

Rigid elastic spherical molecules may be regarded as a limiting case of the inverse power-law potential model Eq. (A.2) corresponding to $\nu = \infty$. For this rigid sphere model, the Ωintegrals read

$$\Omega_{s,r}^{ij} = \frac{(j+1)!}{8}\left[1 - \frac{(1+(-1)^i)}{2(i+1)}\right]\left(\frac{\pi k_B T_0}{2\mu^{sr}}\right)^{1/2}(d_s + d_r)^2 \tag{A.6}$$

where d_s is the molecular diameter of species s. Following [79], it can be computed via the expression

$$\eta_s = 1.016034\frac{5}{16}\frac{\sqrt{m_s k_B T}}{\sqrt{\pi}{d_s}^2} \tag{A.7}$$

and the experimental data on the viscosities η_s of the single gases at the temperature $T = 300\,\mathrm{K}$ have been used, given in [83].
Note that Eq. (A.6) takes the form

$$\Omega_{s,r}^{12} = 3\Omega_{s,r}^{11} \quad \Omega_{s,r}^{13} = 12\Omega_{s,r}^{11} \quad \Omega_{s,r}^{22} = 2\Omega_{s,r}^{11} \tag{A.8}$$

with

$$\Omega_{s,r}^{11} = \frac{1}{4}\left(\frac{\pi k_B T_0}{2\mu^{sr}}\right)^{1/2}(d_s + d_r)^2 \tag{A.9}$$

A.3. (6-12) Lennard-Jones model

In this model, the potential of intermolecular force is given by

$$U^{sr} = 4\epsilon^{sr}\left[\left(\frac{d^{sr}}{r}\right)^{12} - \left(\frac{d^{sr}}{r}\right)^{6}\right] \tag{A.10}$$

where r is the distance between the center of the molecules, ϵ^{sr} is the depth of the potential well (the maximum energy of attraction), and d^{sr} is the reference collision diameter [defined so that $U^{sr}(d^{sr}) = 0$]. In this case, the Ω-integrals cannot be evaluated analytically in closed form and numerical integrations have to be used, for example the ones tabulated in [84], assuming the same temperature as that for the Maxwell molecules and the rigid spheres, i.e., $T = 300\,\mathrm{K}$.